Advanced Imaging with Sound and Light: Photoacoustic Tomography and Quantum Microscopy

Thesis by
Xin Tong

In Partial Fulfillment of the Requirements for the
Degree of
Doctor of Philosophy

Caltech

CALIFORNIA INSTITUTE OF TECHNOLOGY
Pasadena, California

2026
Defended January 09, 2026

ACKNOWLEDGEMENTS

I am deeply grateful to my advisor, Prof. Lihong Wang, for his invaluable guidance, mentorship, and unwavering support throughout my doctoral studies. Under his supervision, I have had the privilege of working in an intellectually rigorous and inspiring environment that encouraged me to pursue meaningful and challenging problems in medical imaging. His vision, insight, and high standards have profoundly shaped my approach to research and scholarship.

I would also like to thank my dissertation committee members—Profs. Alireza Marandi, Changhuei Yang, and Mikhail G. Shapiro—for their time, encouragement, and thoughtful feedback on my research. I am especially grateful to Drs. Lily L. Lai and Lisa D. Yee for their detailed guidance and close collaboration in my clinical research on breast photoacoustic computed tomography.

I sincerely appreciate the support and camaraderie of my lab mates throughout this journey. I am particularly grateful to Drs. Li Lin, Yide Zhang, and Peng Hu for their generous mentorship and guidance in both research and career development. I also thank Drs. Zhe He, Huan Zhao, Rui Cao, and Lei S. Li for their valuable support and collaboration. I am thankful to Chien-Ying Huang, Cindy Z. Liu, Junfu Zheng, Wenyu Liu, and Yilin Luo for their assistance and teamwork, and to Dr. Jinge Yang, Dr. Zhe Guang, Dr. Qihang Liu, Dr. Youchang Zhang, David Garrett, Karteek Dhara, Joshua Olick-Gibson, and Manxiu Cui for many stimulating discussions. I also gratefully acknowledge all members of COIL and City of Hope for their support. Finally, I thank Dr. Konstantin Maslov, Dr. Geng Ku, Christine C. Garske, Catherine L. Pichotta, Joanne V. Pineda, and Kathy Yi for their assistance in the laboratory.

Finally, I wish to express my deepest gratitude to my family for their unconditional love and support. I am profoundly thankful to my partner, Ganning Zhao, for her love, encouragement, and courage. Being with her has brought me joy during moments of success and strength during times of challenge, and has helped me grow into a better person. I am forever grateful to my parents and grandparents for their boundless care and support, no matter the distance or the number of worlds between us.

ABSTRACT

Optical imaging enables visualization of biological structure and function but is fundamentally limited by several physical constraints. Spatial resolution is bounded by optical diffraction, depth penetration is curtailed by strong absorption and scattering in tissue, and image contrast-to-noise ratio is often restricted by photon shot noise in low-light conditions. This thesis advances two novel directions—photoacoustic imaging and quantum imaging—to address these limitations.

In photoacoustic imaging, we design and optimize high-speed photoacoustic computed tomography systems that enable deep, volumetric visualization of vasculature. By incorporating time-gated reconstruction and image-enhancement algorithms, these systems support small-animal imaging of cardiac structure, liver morphology, and brain hemodynamics non-invasively. Building on these foundations, we explore non-invasive breast photoacoustic imaging with high spatiotemporal resolution. Through integration with learning-based feature extraction, classification, and segmentation pipelines, we demonstrate the feasibility of applying photoacoustic imaging in clinical workflows to aid the characterization of breast tissue.

In quantum imaging, we develop two complementary architectures that extend the state of the art in opposite but synergistic directions. The scanning quantum microscope scales up existing quantum imaging approaches, achieving the largest resolvable pixel counts to date by combining entangled-photon illumination with efficient coincidence detection. This platform enables the first demonstration of whole-organism imaging and shows potential in remote sensing and sub-shot-noise imaging. In contrast, the widefield quantum microscope scales down quantum imaging to the microscopic regime, integrating single-photon–sensitive cameras with a covariance-based coincidence estimation algorithm. This approach enables cellular-level imaging and demonstrates quantum-enhanced resolution beyond the classical diffraction limit, establishing a practical pathway for quantum microscopy in biological imaging.

Across both research directions, this thesis advances system design and engineering, quantitative characterization, calibration, reconstruction, and image-enhancement methodologies. Together, these developments establish pathways from physical principles to practical imaging systems, spanning laboratory prototypes through preclinical and clinical applications in biomedical imaging.

PUBLISHED CONTENT AND CONTRIBUTIONS

[1] Y. Zhang†, S. Na†, J. J. Russin†, K. Sastry, L. Lin, J. Zheng, Y. Luo, X. **Tong**, Y. An, P. I. Hu, K. Maslov, T.-W. Tan, C. Y. Liu, and L. V. Wang, "Rotational ultrasound and photoacoustic tomography of the human body," *Nature Biomedical Engineering*, 2026. DOI: `10.1038/s41551-025-01603-5`,
X. Tong participated in the design and construction of the experimental setup, acquired and analyzed the experimental data, and participated in the writing of the manuscript.

[2] P. Hu, X. **Tong**, L. Lin, and L. V. Wang, "Data-driven system matrix manipulation enabling fast functional imaging in tomography," *IEEE Transactions on Medical Imaging*, 2025. DOI: `10.1109/TMI.2025.3612437`,
X. Tong participated in the conception of the project, acquired and analyzed the experimental data, and participated in the writing of the manuscript.

[3] X. **Tong**†, C. Z. Liu†, Y. Luo†, L. Lin†, J. Dzubnar, M. Invernizzi, S. Delos Santos, Y. Zhang, R. Cao, P. Hu, J. Zheng, J. Torres, A. Kasabyan, L. L. Lai, L. D. Yee, and L. V. Wang, "Panoramic photoacoustic computed tomography with learning-based classification enhances breast lesion characterization," *Nature Biomedical Engineering*, 2025. DOI: `10.1038/s41551-025-01435-3`,
X. Tong participated in the conception of the project, designed the patient study and image processing workflow, performed the imaging experiments, analyzed the data, and participated in the writing of the manuscript.

[4] Y. Luo, H.-K. Huang, K. Sastry, P. Hu, X. **Tong**, J. Kuo, Y. Aborahama, S. Na, U. Villa, M. A. Anastasio, and L. V. Wang, "Full-wave image reconstruction in transcranial photoacoustic computed tomography using a finite element method," *IEEE Transactions on Medical Imaging*, 2024. DOI: `10.1109/TMI.2024.3456595`,
X. Tong acquired and analyzed the experimental data and participated in the writing of the manuscript.

[5] X. **Tong**, Y. Zhang, and L. V. Wang, "Enhancing optical microscopy with quantum entanglement," *Optics and Photonics News*, 2024. DOI: `10.1364/opn.35.11.000032`,
X. Tong participated in the writing of the manuscript.

[6] Y. Zhang†, Z. He†, X. **Tong**†, D. C. Garrett, R. Cao, and L. V. Wang, "Quantum imaging of biological organisms through spatial and polarization entanglement," *Science Advances*, 2024. DOI: `10.1126/sciadv.adk1495`,
X. Tong participated in the conception of the project and the construction of the experimental setup, acquired and analyzed the experimental data,

designed the birefringence imaging, sub-shot-noise imaging, and image processing algorithms, and participated in the writing of the manuscript.

[7] Y. Zhang†, P. Hu†, L. Li, R. Cao, A. Khadria, K. Maslov, X. **Tong**, Y. Zeng, L. Jiang, Q. Zhou, and L. V. Wang, "Ultrafast longitudinal imaging of haemodynamics via single-shot volumetric photoacoustic tomography with a single-element detector," *Nature Biomedical Engineering*, 2024. DOI: `10.1038/s41551-023-01149-4`,
X. Tong acquired and analyzed the experimental data and participated in the writing of the manuscript.

[8] Z. He†, Y. Zhang†, X. **Tong**†, L. Li, and L. V. Wang, "Quantum microscopy of cells at the heisenberg limit," *Nature Communications*, 2023. DOI: `10.1038/s41467-023-38191-4`,
X. Tong participated in the conception of the project and the construction of the experimental setup, acquired and analyzed the experimental data, designed the covariance-based coincidence detection algorithms, and participated in the writing of the manuscript.

[9] L. Lin†, X. **Tong**†, S. I. Cavallero, Y. Zhang, S. Na, R. I. Cao, T. K. Hsiai, and L. V. Wang, "Non-invasive photoacoustic computed tomography of rat heart anatomy and function," *Light: Science & Applications*, 2023. DOI: `10.1038/s41377-022-01053-7`,
X. Tong participated in the conception of the project and the construction of the experimental setup, acquired and analyzed the experimental data, implemented the time-gated reconstruction algorithms, and participated in the writing of the manuscript.

[10] K. Sastry, Y. Zhang, P. I. Hu, Y. Luo, X. **Tong**, S. Na, and L. V. Wang, "A method for the geometric calibration of ultrasound transducer arrays with arbitrary geometries," *Photoacoustics*, 2023. DOI: `10.1016/j.pacs.2023.100520`,
X. Tong acquired and analyzed the experimental data and participated in the writing of the manuscript.

[11] X. **Tong**†, Z. He†, Y. Zhang†, S. Solomon, L. Lin, Q. Song, and L. V. Wang, "Experimental full-domain mapping of quantum correlation in clauser-horne-shimony-holt scenarios," *Physical Review Applied*, 2023. DOI: `10.1103/physrevapplied.19.034049`,
X. Tong participated in the conception of the project and the construction of the experimental setup, acquired and analyzed the experimental data, and participated in the writing of the manuscript.

[12] X. **Tong**†, L. Lin†, P. I. Hu, R. I. Cao, Y. Zhang, J. Olick-Gibson, and L. V. Wang, "Non-invasive 3d photoacoustic tomography of angiographic anatomy and hemodynamics of fatty livers in rats," *Advanced Science*, 2023. DOI: `10.1002/advs.202205759`,
X. Tong participated in the conception of the project and the construction

of the experimental setup, acquired and analyzed the experimental data, implemented the time-gated reconstruction algorithms, and participated in the writing of the manuscript.

[13] L. Lin†, P. I. Hu†, X. **Tong**†, S. Na†, R. I. Cao, X. I. Yuan, D. C. Garrett, J. Shi, K. Maslov, and L. V. Wang, "High-speed three-dimensional photoacoustic computed tomography for preclinical research and clinical translation," *Nature Communications*, 2021. DOI: `10.1038/s41467-021-21232-1`,
X. Tong participated in the conception of the project, acquired and analyzed the experimental data, and participated in the writing of the manuscript.

[14] L. Lin†, X. **Tong**†, P. I. Hu, M. Invernizzi, L. L. Lai, and L. V. Wang, "Photoacoustic computed tomography of breast cancer in response to neoadjuvant chemotherapy," *Advanced Science*, 2021. DOI: `10.1002/advs.202003396`,
X. Tong participated in the conception of the project, acquired and analyzed the experimental data, and participated in the writing of the manuscript.

† Denotes equal contribution.

TABLE OF CONTENTS

LIST OF ILLUSTRATIONS

LIST OF TABLES

NOMENCLATURE

2D. Two-dimensional.

3D. Three-dimensional.

AUROC. Area under the receiver operating characteristic curve.

BBO. β-barium borate.

BI-RADS. Breast imaging reporting and data system.

CHSH. Clauser–Horne–Shimony–Holt.

CNR. Contrast-to-noise ratio.

CT. Computed tomography.

DAQ. Data acquisition.

DCIS. Ductal carcinoma *in situ*.

DOF. Depth of field.

DOI. Diffuse optical imaging.

ECG. Electrocardiogram.

EMCCD. Electron-multiplying charge-coupled device.

EPR. Einstein–Podolsky–Rosen.

ESF. Edge-spread functions.

FOV. Field of view.

FWHM. Full width at half maximum.

HPV. Hepatic portal vein.

ICE. Imaging by coincidence from entanglement.

IDC. Invasive ductal carcinoma.

LCA. Left coronary artery.

LED. Light-emitting diode.

LHS. Local hidden state.

LSF. Line-spread functions.

MAP. Maximum-amplitude projection.

MRI. Magnetic resonance imaging.

NA. Numerical aperture.

NAC. Neoadjuvant chemotherapy.

NAFLD. Non-alcoholic fatty liver disease.

NASH. Non-alcoholic steatohepatitis.

PACT. Photoacoustic computed tomography.

PAI. Photoacoustic imaging.

PAM. Photoacoustic microscopy.

PAT. Photoacoustic tomography.

PET. Positron emission tomography.

PSF. Point-spread function.

QI. Quantum imaging.

QKD. Quantum key distribution.

QMC. Quantum microscopy by coincidence.

QS. Quantum steering.

QST. quantum state tomography.

RCA. Right coronary artery.

ROC. Receiver operating characteristic.

ROI. Region of interest.

SAM. Segment anything model.

SBH-PACT. Single-breath-hold photoacoustic computed tomography.

SEV. Superior epigastric vessel.

SIP-PACT. Single-impulse panoramic photoacoustic computed tomography.

SNSPD. Superconducting single-photon photodiode array.

SoS. Speed of sound.

SPCM. Single-photon counting module.

SPDC. Spontaneous parametric down-conversion.

SPECT. Single-photon emission computed tomography.

SSIM. Structural similarity index measure.

SSN. Sub-shot-noise.

SVD. Singular-value decomposition.

t-SNE. t-distributed stochastic neighbor embedding.

TG. Time-gating.

UBP. Universal back-projection.

US. Ultrasonography.

XGBoost. eXtreme Gradient Boosting.

Chapter 1

INTRODUCTION TO PHOTOACOUSTIC IMAGING

Photoacoustic imaging (PAI), or photoacoustic tomography (PAT), is a hybrid modality that combines pulsed optical excitation with ultrasonic detection to map optical absorption in biological tissues *in vivo* [1]–[4]. In PAI, short laser pulses are absorbed by endogenous or exogenous chromophores, leading to rapid thermoelastic expansion and the emission of broadband ultrasonic waves. These photoacoustic waves propagate with relatively low scattering and are detected at the tissue surface by ultrasound transducers. Image reconstruction then yields spatial maps of the initial pressure distribution, which are closely related to optical absorption.

Depending on the implementations, PAI can be categorized into photoacoustic microscopy (PAM), photoacoustic computed tomography (PACT), photoacoustic endoscopy, etc. [1], [2]. Among these, PACT employs multi-element ultrasonic arrays and broad optical illumination (often covering the entire field of view or FOV) and applies image reconstruction algorithms to recover three-dimensional (3D) absorption distributions [2]. PACT achieves scalable mesoscopic to macroscopic imaging with centimeter-scale penetration while maintaining sub-millimeter spatial resolution, bridging microscopic optical techniques and whole-body radiological imaging.

This chapter focuses on the principles and applications of PACT. Section 1.1 summarizes the physical and system-level principles of PACT. Section 1.2 reviews selected preclinical and clinical applications, with emphasis on small-animal and human studies that demonstrate the strengths and current limitations of PACT.

1.1 Principles of PACT

Photoacoustic effect and signal generation

The fundamental mechanism of PACT is the photoacoustic effect. A short laser pulse with fluence $F(\mathbf{r})$ illuminates tissue at the position $\mathbf{r}$. A fraction of the optical energy is absorbed by chromophores with absorption coefficient $\mu_a(\mathbf{r})$, leading to an initial specific energy deposition

$$H(\mathbf{r}) = \mu_a(\mathbf{r})F(\mathbf{r}). \tag{1.1}$$

Under stress and thermal confinement, the absorbed optical energy is converted into a transient pressure rise $p_0(\mathbf{r})$ given by

$$p_0(\mathbf{r}) = \Gamma(\mathbf{r}) H(\mathbf{r}), \tag{1.2}$$

where Γ is the Grueneisen parameter that depends on the local thermal expansion coefficient, isothermal compressibility and specific heat [2]. The initial pressure distribution $p_0(\mathbf{r})$ acts as an acoustic source and generates broadband ultrasound waves that satisfy the inhomogeneous wave equation

$$\nabla^2 p(\mathbf{r}, t) - \frac{1}{c^2(\mathbf{r})} \frac{\partial^2 p(\mathbf{r}, t)}{\partial t^2} = -\frac{\beta}{C_p} \frac{\partial H(\mathbf{r}, t)}{\partial t}, \tag{1.3}$$

where $p(\mathbf{r}, t)$ is the acoustic pressure, $c(\mathbf{r})$ is the speed of sound, β is the thermal expansion coefficient and C_p is the specific heat.

The measured time-resolved signals at the array elements encode information about the 3D distribution of $p_0(\mathbf{r})$, and therefore about $\mu_a(\mathbf{r})$ convolved with the spatial profile of the fluence $F(\mathbf{r})$ [1], [2].

PACT system architectures

PACT systems are characterized by the illumination scheme, the acoustic detection geometry and the data acquisition strategy [2]–[4].

Broad-beam or diffuse illumination is commonly used to cover a large FOV, for example an entire small animal or a human breast. Illumination can be delivered from one or multiple sides, or through optical fiber bundles integrated with the ultrasound probe. To stay within safety limits, the fluence at the skin surface is kept below the ANSI standards for the relevant wavelength and pulse repetition rate.

Acoustic detection is typically performed with piezoelectric or capacitive micromachined ultrasonic transducer arrays. Geometries include:

- **Planar or linear arrays**, often integrated into hand-held probes and are compatible with conventional clinical ultrasound systems. These arrays are widely used in breast and thyroid imaging and in multi-purpose clinical PACT platforms [4], [5].
- **Curved, circular, or hemispherical arrays**, designed to provide wide solid-angle coverage and more isotropic resolution. Examples include ring-shaped and hemispherical arrays for small-animal and whole-breast imaging [6]–[10]. The work from this thesis focuses on this geometry.

In PACT, a single laser pulse can generate a cross-sectional (two-dimensional, 2D) or 3D image, thus achieving high frame rates with parallel acquisition, limited mainly by the laser repetition rate and data throughput.

Image reconstruction and spatial resolution

Given the measured time-resolved pressure signals $p(\mathbf{r}_s, t)$ on a measurement surface $\mathbf{r}_s$, the goal of reconstruction is to recover $p_0(\mathbf{r})$. For homogeneous media and sufficiently dense sampling, analytic algorithms based on the inverse spherical Radon transform or back-projection are commonly used and can be implemented efficiently in the time or frequency domain [2].

For more complex media, including heterogeneous speed of sound and limited-view sampling, model-based and iterative methods can improve image quality at the cost of increased computation. k-space methods and finite-difference time-domain solvers are widely used to model wave propagation and to compensate for acoustic heterogeneities [11]. More recently, deep-learning approaches have been investigated to reconstruct images from sparse-view or noisy data [12], [13].

The spatial resolution of PACT is mainly determined by the acoustic bandwidth and the angular sampling of the detection aperture. In practice, the achievable resolution scales approximately linearly with imaging depth, with a typical depth-to-resolution ratio on the order of 100–200 in soft tissue [2]. By choosing lower center frequencies for deeper imaging and higher frequencies for superficial targets, PACT can be tuned across mesoscopic and macroscopic length scales.

Contrast mechanisms in PACT

PACT is fundamentally sensitive to optical absorption. Endogenous chromophores provide intrinsic contrast, including oxy- and deoxyhemoglobin, melanin, water, lipids, and nucleic acids [2]–[4]. By tuning the excitation wavelength and performing spectral unmixing, PACT can quantify the total hemoglobin concentration, hemoglobin oxygen saturation, and other functional parameters such as blood volume, blood flow surrogates, and oxygen metabolism.

In addition to endogenous contrast, exogenous agents such as organic dyes, nanoparticles and targeted molecular probes expand PACT into molecular imaging. These agents can be engineered to absorb in the near-infrared optical window and to report specific biological processes, including receptor expression, enzyme activity and drug delivery [2], [4].

Because PACT uses ultrasound detection, it inherits the advantages of ultrasound imaging: relatively low cost, portability, lack of ionizing radiation and compatibility with real-time operation. At the same time, PACT provides optical absorption contrast that is complementary to ultrasound's primarily scattering-based contrast, making combined PACT–ultrasound systems especially attractive for clinical translation [3], [4].

1.2 Applications of PACT

PACT has been applied across a wide range of biological systems, from small animal models to human subjects, leveraging its ability to visualize vascular anatomy, blood oxygenation and molecular contrast *in vivo* [1]–[4]. This section highlights representative preclinical and clinical applications of PACT.

Preclinical applications of PACT

Whole-body and organ-scale imaging in small animals

Array-based PACT has become a powerful tool for whole-body and organ-scale imaging in small animals. Early systems using circular or ring-shaped array geometries demonstrated noninvasive 3D imaging of entire mice, resolving major organs and vascular networks *in vivo* [6], [7]. Subsequent advances in laser technology, transducer arrays and acquisition electronics enabled higher frame rates and improved spatial resolution.

Single-impulse panoramic PACT (SIP-PACT) combines wide-field illumination with a full-ring confocal array to capture whole-body dynamics of small animals at high spatiotemporal resolution [8]. SIP-PACT has been used to visualize cardiac cycles, respiratory motion, and fast vascular responses to physiological perturbations in mice, while maintaining a large FOV and near-isotropic in-plane resolution.

More recently, high-speed 3D PACT systems have extended volumetric imaging to entire rodents with acquisition times on the order of tens of milliseconds per volume [10]. Such systems support real-time tracking of organ motion and hemodynamic changes, providing a unique platform for studying disease progression and treatment response *in vivo*.

Functional and molecular imaging in animal models

Tumor-bearing rodent models have been extensively studied with PACT to evaluate anti-angiogenic therapies, vascular-targeted agents, and nanoformulated drugs. In these settings, exogenous contrast agents such as near-infrared dyes and nanoparticles are often used to enhance molecular specificity, for example, to target integrins, growth factor receptors, or protease activity [2]. Dynamic contrast-enhanced PACT can quantify perfusion and permeability, offering a noninvasive readout of drug delivery and therapeutic efficacy.

Beyond oncology, PACT has been applied to preclinical studies of brain function, cardiovascular disease, liver and kidney pathology, and inflammatory processes. Multiscale PAT frameworks integrate PACT with other implementations to connect organ-level observations with microscopic molecular readouts [14].

Clinical applications of PACT

The past decade has seen rapid progress in translating PACT to the clinic. Early pilot studies in humans have now matured into multi-center trials and the first regulatory approvals for PACT-based devices [3], [4]. Most clinical systems are integrated with conventional ultrasound platforms, allowing co-registered ultrasound and PACT measurements in a single probe.

Breast imaging and oncology

Breast imaging has been a leading clinical application of PACT. Hemispherical and ring-array PACT systems have demonstrated 3D imaging of the human breast with sub-millimeter resolution and penetration depths of several centimeters, sufficient to cover the compressed breast volume [9], [15], [16]. In single-breath-hold PACT, a hemispherical array surrounding the breast acquires volumetric angiographic images within 10–15 s, capturing the vascular architecture and hemoglobin oxygenation patterns associated with malignant lesions [3], [9].

Hand-held PACT–ultrasound probes based on linear arrays have been evaluated in large patient cohorts. In a pivotal multi-center study involving more than 1,600 women, the addition of tomographic PAI to ultrasound significantly improved the specificity of breast mass characterization while maintaining high sensitivity, reducing the number of unnecessary biopsies for benign lesions [4], [5]. PACT-derived features such as internal vascularity, peripheral vessel patterns and local hemoglobin oxygen saturation provide complementary physiological information beyond grayscale ultrasound.

Longitudinal PACT has also been used to monitor responses to neoadjuvant chemotherapy (NAC). Changes in tumor vascularity and oxygenation during treatment correlate with pathological response, suggesting that PACT could serve as an early biomarker to adapt therapy and avoid ineffective regimens [3], [17].

Dermatology and peripheral vasculature

In dermatology, multispectral optoacoustic tomography and related mesoscopic PACT systems have been used to image melanomas and non-melanoma skin cancers, resolving melanin distribution, vascular morphology and oxygenation in and around lesions [4], [15]. Although many of these systems operate at slightly shallower depths than macroscopic PACT, they share the same tomographic principles and reconstruction methods.

Hand-held PACT has also been applied to peripheral vasculature in the limbs, visualizing small arteries and veins, skin microcirculation and vascular responses to thermal or pharmacological stimuli [18], [19]. Photoacoustic lymphangiography has been used to map vessels and assess lymphedema, showing advantages over near-infrared fluorescence methods in depth penetration and quantification [4], [20].

Gastrointestinal, inflammatory and endocrine diseases

Tomographic PAI has been explored in inflammatory bowel disease, where MSOT imaging of the bowel wall can assess disease activity and treatment response, including in pediatric populations [4], [21], [22]. These studies highlight the ability of PACT-like systems to quantify vascular and inflammatory signatures noninvasively and repeatedly, without ionizing radiation.

In the endocrine system, PACT has been investigated for thyroid imaging and risk stratification of thyroid nodules, where combined ultrasound and PAI can improve differentiation between benign and malignant lesions by jointly considering morphology and vascular features [23].

Challenges in PACT

Despite considerable progress, several technical and translational challenges remain. Optical attenuation continues to constrain the achievable imaging depth—an especially limiting factor when imaging larger or highly attenuating human subjects. Acoustic aberrations arising from heterogeneous tissue composition can distort wavefronts and degrade image quality, while quantitative spectroscopic PACT still requires robust correction for wavelength-dependent fluence variations to ensure reliable biomarker extraction [3]. System-dependent image quality further complicates protocol standardization, as variations in illumination geometry, detector configuration, reconstruction algorithms, and calibration procedures can lead to substantial inter-system variability across institutions. In addition, the intrinsic trade-off between frame rate and FOV remains a practical constraint: expanding the angular or spatial coverage typically demands longer acquisition times, larger arrays, or more complex multiplexing strategies, which may not be compatible with certain clinical workflows.

Beyond physics and engineering limitations, broader translational factors also limit the clinical impact of PACT. Workflow integration with existing imaging pathways, demonstration of cost-effectiveness relative to standard-of-care modalities, and adequate training for technologists and clinicians are essential for widespread adoption [4]. Finally, although PACT has shown strong promise as a complementary modality, its potential as a standalone clinical imaging system—capable of independently guiding diagnosis, monitoring, or intervention—has not yet been fully explored. Establishing such use cases will require coordinated advances in hardware performance, quantitative image interpretation, and multi-site validation.

In summary, PACT has evolved from a laboratory prototype into a promising preclinical and clinical imaging modality that complements conventional techniques. Its ability to noninvasively map vascular anatomy, function, and molecular contrast with high spatial resolution positions PACT as a powerful tool for both mechanistic studies in animal models and translational imaging in patients.

1.3 Dissertation outline (Chapters II–V)

Chapter II presents the design and realization of a high-speed three-dimensional PACT platform, with emphasis on illumination engineering, multi-element detection, data acquisition, and real-time reconstruction. The chapter details the methodological advances that enable deep-tissue volumetric imaging, including calibration strategies, signal processing pipelines, and reconstruction algorithms incorporated into the system.

Chapter III applies the developed 3D-PACT system to non-invasive imaging of small-animal cardiac and hepatic anatomy. The chapter describes the experimental design, ECG-synchronized acquisitions, and time-gated reconstruction methods that enable volumetric visualization of dynamic rat organs. It further analyzes anatomical features, tissue-dependent optical absorption, and comparative observations across lean, obese, and hypertensive cohorts.

Chapter IV extends PACT into a clinical context by investigating its utility in monitoring breast cancer response to neoadjuvant chemotherapy. It demonstrates acquisition protocols, quantification of tumor-associated vasculature, and interpretation of temporal changes in vascular morphology. The results illustrate the potential of PACT to serve as a non-invasive adjunct tool for assessing therapeutic response.

Chapter V introduces panoramic PACT for comprehensive breast imaging and presents a learning-based classification framework for lesion characterization. The chapter integrates handcrafted and learned features, evaluates classifier performance, and compares PACT-derived diagnostic information against conventional modalities. It demonstrates how machine learning enhances the interpretability and diagnostic power of PACT datasets.

Chapter 2

DEVELOPMENT AND APPLICATIONS OF A HIGH-SPEED 3D PACT SYSTEM

[1] L. Lin†, P. I. Hu†, X. **Tong**†, S. Na†, R. I. Cao, X. I. Yuan, D. C. Garrett, J. Shi, K. Maslov, and L. V. Wang, “High-speed three-dimensional photoacoustic computed tomography for preclinical research and clinical translation,” *Nature Communications*, 2021. DOI: `10.1038/s41467-021-21232-1`,

[2] P. Hu, X. **Tong**, L. Lin, and L. V. Wang, “Data-driven system matrix manipulation enabling fast functional imaging in tomography,” *IEEE Transactions on Medical Imaging*, 2025. DOI: `10.1109/TMI.2025.3612437`,

[3] Y. Zhang†, S. Na†, J. J. Russin†, K. Sastry, L. Lin, J. Zheng, Y. Luo, X. **Tong**, Y. An, P. I. Hu, K. Maslov, T.-W. Tan, C. Y. Liu, and L. V. Wang, “Rotational ultrasound and photoacoustic tomography of the human body,” *Nature Biomedical Engineering*, 2026. DOI: `10.1038/s41551-025-01603-5`,

[4] Y. Luo, H.-K. Huang, K. Sastry, P. Hu, X. **Tong**, J. Kuo, Y. Aborahama, S. Na, U. Villa, M. A. Anastasio, and L. V. Wang, “Full-wave image reconstruction in transcranial photoacoustic computed tomography using a finite element method,” *IEEE Transactions on Medical Imaging*, 2024. DOI: `10.1109/TMI.2024.3456595`,

[5] K. Sastry, Y. Zhang, P. I. Hu, Y. Luo, X. **Tong**, S. Na, and L. V. Wang, “A method for the geometric calibration of ultrasound transducer arrays with arbitrary geometries,” *Photoacoustics*, 2023. DOI: `10.1016/j.pacs.2023.100520`,

2.1 Motivation

The combination of deep penetration and optical absorption contrast makes PACT particularly attractive for biological imaging. It complements several established modalities: compared with fluorescence imaging in tissue [24], PACT preserves sub-millimeter resolution at depth; unlike ultrasound, PACT is free from speckle artifacts and benefits from absorption-based endogenous contrast; unlike CT and PET, it uses non-ionizing illumination; and compared with MRI, PACT offers faster volumetric imaging at lower cost. In breast imaging, for example, a modern 3D-PACT system can reach 4 cm penetration with nearly isotropic 0.37 mm–0.39 mm resolution in a single 10 s scan—substantially finer than typical 3T or 7T MRI voxel dimensions [25], [26].

Efforts to scale PACT to true 3D coverage have explored spherical, hemispherical, spiral, and planar detection geometries [6], [27]–[35]. These systems vary substantially in aperture completeness, spatial sampling density, laser delivery, and achievable FOV. Despite notable advances, challenges remain: limited angular coverage can produce severe limited-view artifacts; sparse detectors constrain spatial resolution and reduce contrast-to-noise ratio (CNR); and non-uniform scanning illumination can violate assumptions built into 3D back-projection algorithms [36], [37].

To overcome these issues, we developed a high-speed 3D-PACT platform combining a densely sampled hemispherical acoustic aperture with stable 1064 nm light delivery. The design goals were: (1) large and scalable FOV; (2) nearly isotropic spatial resolution throughout the volume; (3) high noise-equivalent sensitivity for deep tissue imaging; (4) high acquisition speed; and (5) minimal limited-view artifacts.

This system supports imaging across a wide range of scales—from mapping rat brain vasculature and hemodynamics to imaging full human breasts within a single breath-hold. The following sections describe the system architecture and its performance, with the technical procedures (calibration, illumination engineering, reconstruction algorithms) embedded directly within the narrative.

2.2 Characteristics and engineering of the 3D-PACT system

A schematic overview of the 3D-PACT system is shown in Fig. 2.1. The platform integrates four key subsystems that operate in synchrony: (1) a hemispherical multi-array acoustic detector; (2) integrated low-noise pre-amplification and multichannel digitization; (3) a coaxial mechanical scanning mechanism enabling dense angular sampling; (4) a regulated near-infrared illumination module designed for uniform fluence distribution over the imaging depth.

At the center of the system is a hemispherical shell containing four arc-shaped ultrasonic arrays, each with 256 elements, for a total of 1024 channels (Figs. 2.1a and b). Each element is centered at 2.25 MHz with a fractional bandwidth exceeding 98% (Fig. 2.1e), enabling detection of both fine superficial vasculature and deep tissue structures. The arrays were originally fabricated as circular arcs, but manufacturing imperfections introduced slight deviations from the ideal geometry.

To restore precise detector geometry, we characterized each element's spatial location by imaging a point absorber placed at multiple known positions throughout the FOV. The measured time-of-flight residuals from all positions were assembled into a nonlinear system, and we used Jacobi iteration to refine the estimated coordinates of all 1024 elements until convergence. Each detector element connects directly into a 1024-channel low-noise pre-amplifier array housed in the base of the hemispherical module. This design minimizes cable-induced noise by amplifying weak photoacoustic signals prior to transmission. Amplified outputs are routed through four phase-matched cables into four synchronized 256-channel data-acquisition (DAQ) units. Each DAQ provides tunable analog gain (12–51 dB), 12-bit sampling, and hardware triggering tied to the laser pulse. The tight integration between pre-amplifiers and DAQs substantially improves noise-equivalent sensitivity, particularly for deep tissue imaging where both optical fluence and acoustic pressure decay.

The array housing and DAQ modules are mounted on a coaxial rotation stage that sweeps the detector assembly over a 90° arc during a 3D scan. This rotation effectively enlarges the solid-angle coverage and ensures dense sampling consistent with spatiotemporal Nyquist criteria [38]. Depending on the desired FOV, the scan duration ranges from 2 s (small volumes such as rodent brain) to 10 s (large volumes such as human breast). All channels acquire data at each angular position, enabling high-resolution tomographic reconstruction with minimal angular undersampling artifacts.

Uniform and stable illumination across scanning angles is essential for accurate 3D reconstruction. We deliver 1064 nm nanosecond pulses from a Q-switched Nd:YAG laser through a one-inch diameter lens tube permanently affixed to the base of the detector housing. Two engineered diffusers are placed in series within this tube. Because water and soft tissue exhibit relatively low attenuation at 1064 nm, this wavelength is favorable for deep organ imaging, including rodent brain, liver, and human breast [39]. The fluence at the tissue surface remains within ANSI safety limits [40].

Following geometric calibration, we quantified the system's point-spread function by imaging a 50 µm aluminum particle at multiple depths. The reconstructed volumetric PSF exhibited near-isotropic resolution: approximately 390 µm in the transverse plane and 370 µm along depth (Figs. 2.1c and d). Because spatial sampling density satisfies both temporal and angular Nyquist criteria, resolution remains uniform

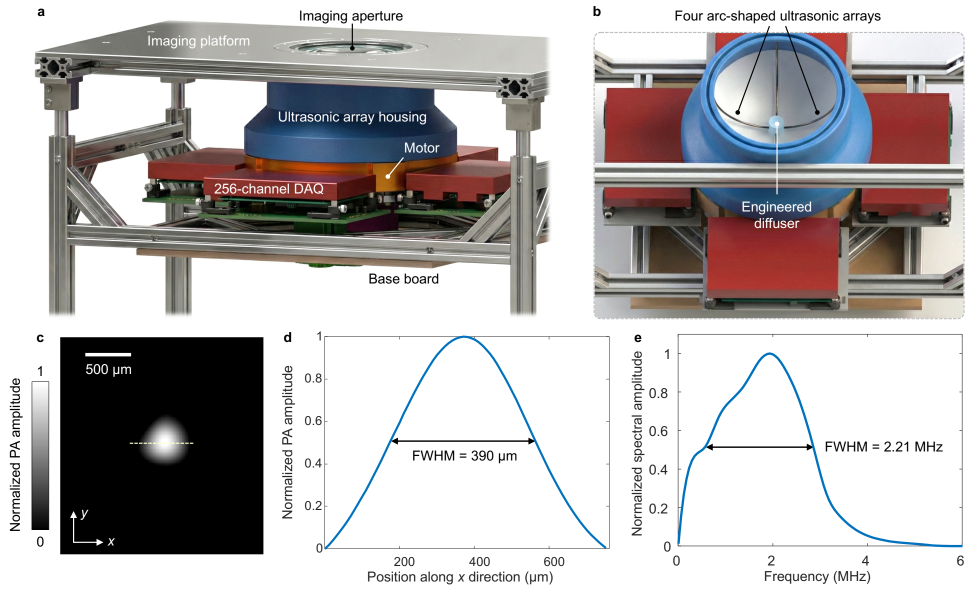

Figure 2.1: **Overview of the 3D-PACT system.** (a) Perspective rendering of the full system. (b) Cut-away view showing the four arc-shaped ultrasonic detector arrays and pre-amplifier housing. (c) Photograph of the hemispherical module. (d) Leaf-skeleton phantom before and after geometric calibration.

across large FOVs without the degradation commonly seen in sparse hemispherical systems.

All volumetric reconstructions are performed using a dual-speed-of-sound (SoS) 3D back-projection algorithm. Water and tissue possess distinct SoS values, and ignoring this difference leads to spatially varying blurring in deep regions. To correct this, we segment the water–tissue boundary based on the cropped volumetric images and compute separate acoustic propagation delays for each region during back-projection. This procedure stabilizes resolution across depth and improves quantification of vascular diameters in both rat brain and human breast imaging.

Raw A-lines are first bandpass-filtered to remove low-frequency electrical noise and high-frequency electronic artifacts. After geometric alignment, each channel is corrected for its temporal offset, and signals from all scanning angles are combined. Reconstruction is performed on a uniform 3D Cartesian grid, typically 256^3 or 512^3 voxels depending on the target FOV. Post-processing includes depth compensation, collaborative filtering to suppress background noise, and vessel-enhancement filtering when visualizing angiographic structures.

The system design and performance described above lay the groundwork for the imaging studies presented in the next sections. The same hardware platform supports high-speed functional mapping in the rat brain and deep volumetric breast imaging in humans.

2.3 3D-PACT of the rat brain anatomy and hemodynamics

Rodent brains provide a powerful model for studying cerebrovascular structure and neural–vascular coupling. High-speed, deep-penetration imaging is essential for capturing both static vascular architecture and dynamic hemodynamic responses to physiological and external stimuli. The 3D-PACT platform is well suited for this task: the panoramic acoustic aperture reduces skull-induced distortion, the 1064 nm illumination enables robust penetration, and the system's acquisition speed allows volumetric imaging at a rate sufficient for functional studies.

Following anesthesia and hair removal, rats were positioned horizontally with their cortical surface facing downward toward the membrane interface. For high-fidelity angiography, the parietal bone was thinned but kept intact during functional imaging. This approach reduces high-frequency distortion while preserving the natural cerebrovascular environment.

Figure 2.2 illustrates the volumetric angiograms acquired from a representative rat. With a 1064 nm excitation wavelength and the complete hemispherical detection geometry, a single 5 s scan captured the cerebral vasculature from cortex to deep brain regions (10 mm depth). When higher CNR was desired, eight consecutive 5 s scans were averaged. The dual-speed-of-sound reconstruction described earlier ensured accurate geometric representation of deep structures.

The resulting volumes exhibit clear vascular boundaries with minimal limited-view artifacts. Transverse and coronal slices in Figs. 2.2b and c resolve major arteries, veins, and venous sinuses, including the superior sagittal sinus (SSS), sigmoid sinus (SS), middle cerebral artery (MCA), and olfactory artery (OA). Even without averaging, the system yields high-contrast angiograms within 5 s.

To investigate functional hemodynamics, we acquired volumetric data continuously at 0.5 Hz. This rate is primarily limited by the 50 Hz laser repetition frequency and the number of angular steps required for dense sampling. Higher volumetric rates are achievable with higher-repetition-rate lasers (e.g., 100 Hz).

Hemodynamic fluctuations were induced via controlled modulation of inhalation gases (oxygen vs. nitrogen) and through varying concentrations of isoflurane anes-

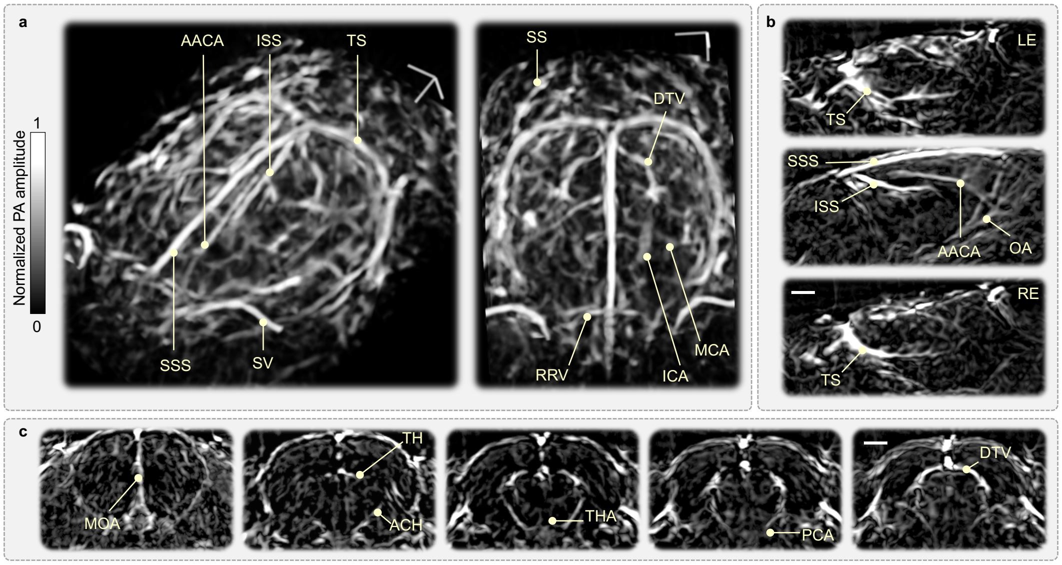

Figure 2.2: **3D-PACT of a rat brain *in vivo*.** (a) Rendered volumetric angiogram covering the entire brain. (b) Transverse slices at varying depths. (c) Coronal slices from rostral to caudal regions. AACA, azygos of the anterior cerebral artery; ACH, anterior choroidal artery; DTV, dorsal thalamic vein; ICA, internal carotid artery; ISS, inferior sagittal sinus; MCA, middle cerebral artery; MOA, medial orbitofrontal artery; OA, olfactory artery; PCA, posterior cerebral artery; RRV, rostral rhinal vein; SSS, superior sagittal sinus; TS, transverse sinus.

thesia. At each time point, raw multi-angle PACT data were reconstructed with the dual-SoS algorithm. ROIs were selected around major vessels and cortical regions, and voxel intensities within each ROI were averaged to form time traces reflecting changes in oxyhemoglobin-dominated absorption.

At 1064 nm, the absorption coefficient of oxyhemoglobin is approximately an order of magnitude larger than that of deoxyhemoglobin. Thus, temporal variations in local PA amplitude predominantly reflect changes in oxygenated blood volume and, secondarily, vascular diameter.

Figures 2.3a and c demonstrates the brain's response to acute hypoxia. Three coronal slices exhibit an overall reduction in PA amplitude during a 30 s pure nitrogen inhalation, reflecting decreased oxygenation. ROIs defined on these slices (Fig. 2.3b) show that signal drops are larger in major vessels than in brain parenchyma; the latter contains time-invariant contributions from lipids, water, and proteins [41].

Signal traces from the azygos of the anterior cerebral artery (AACA), olfactory artery (OA), superior sagittal sinus (SSS), and inferior sagittal sinus (ISS) show comparable fractional changes (Fig. 2.3c). During extended hypoxia, the rate of

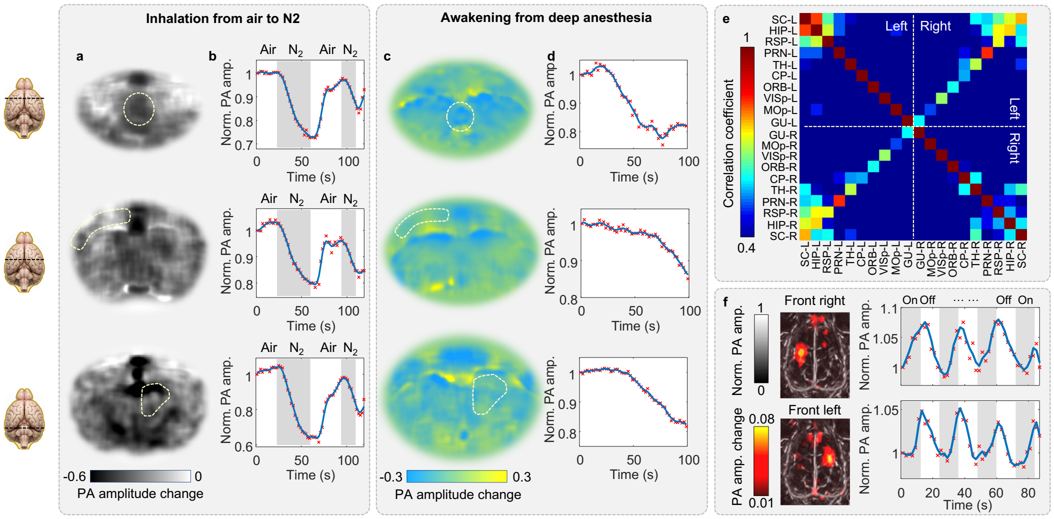

Figure 2.3: **Functional hemodynamic imaging.** (a) PA amplitude changes across coronal slices during nitrogen inhalation. (b) ROI-averaged responses showing decreased oxygenation. (c) Dynamics from four major vessels during hypoxia. AACA, azygos of the anterior cerebral artery; OA, olfactory artery; SSS, superior sagittal sinus; ISS, inferior sagittal sinus. (d–f) Hemodynamic changes during emergence from deep anesthesia. (g) Functional connectivity across 20 anatomically selected regions. (h) Cortical responses to electrical stimulation of the forelimbs.

PA decline plateaus, consistent with reduced oxygen consumption after prolonged oxygen deprivation [42]. Shorter hypoxia bouts (e.g., 10 s) produce more linear early-phase dynamics.

Isoflurane modulates both vascular tone and metabolic oxygen extraction [43], [44]. Figures 2.3d–f show the decrease in PA amplitude throughout the brain as anesthesia levels diminish. PA reductions in arteries and veins are similar (Fig. 2.3f), but the underlying causes differ: in veins, decreased oxygen saturation and reduced vessel diameter both contribute; in arteries, changes are dominated by vasoconstriction with only mild variations in oxygen saturation [45].

Interestingly, fractional PA changes in parenchymal regions (Fig. 2.3e) match those in major vessels. This consistency suggests that small-vessel contraction—which affects parenchymal ROIs—is more pronounced during emergence compared to contraction in major arteries.

Spontaneous hemodynamic fluctuations encode low-frequency activity patterns analogous to resting-state fMRI [46]. Using 3D-PACT, these fluctuations were recorded in high spatial detail across the entire brain.

We defined 20 anatomical ROIs spanning cortex, midbrain, and deep nuclei. For each ROI, temporal traces were bandpass-filtered to retain the hemodynamic frequency band (0.01–0.1 Hz). Pearson correlation coefficients were computed for every ROI pair. The resulting connectivity matrix (Fig. 2.3g) exhibits expected bilateral symmetry between homologous regions.

To assess task-evoked hemodynamics, we applied periodic electrical pulses to the forelimbs and imaged the resulting cortical responses at 0.5 Hz. Figure 2.3h shows increased PA amplitudes in motor-sensory regions contralateral to stimulation. The temporal profile of the PA response matches expected neurovascular activation dynamics.

Physiological motion—especially respiration—introduces periodic distortions. For the brain, these effects are weaker but still noticeable in deep structures. To suppress them, we implemented a time-gated motion-correction scheme (also used for abdominal imaging shown later). Each volumetric frame was partitioned into temporal segments corresponding to distinct breathing phases; segments with minimal motion were selected and combined for reconstruction.

This approach successfully removed breathing motion from images of a pregnant rat abdomen, revealing embryos that were initially blurred. The same strategy stabilizes cerebral imaging and enables clearer functional mapping.

The 3D-PACT system enables whole-brain volumetric imaging with high spatial resolution and functional sensitivity. The ability to resolve individual arteries, follow hemodynamic changes across multiple physiological challenges, and quantify intrinsic connectivity demonstrates its utility as a preclinical neuroimaging tool. Unlike modalities such as fMRI, which offer slower volumetric rates and coarser resolution, 3D-PACT captures vascular dynamics at the level of individual vessels across the entire brain volume.

2.4 3D-PACT of human breasts *in vivo*

Early detection of breast cancer significantly improves survival, and recent studies highlight that tumor biology—rather than size alone—contributes critically to prognosis [47], [48]. This motivates the development of imaging modalities that are non-ionizing, cost-effective, and capable of resolving vascular morphology and functional contrast. While mammography and ultrasound remain clinical workhorses, each has limitations: mammography offers high spatial resolution but relies on ionizing radiation and weak soft-tissue contrast; ultrasound is widely

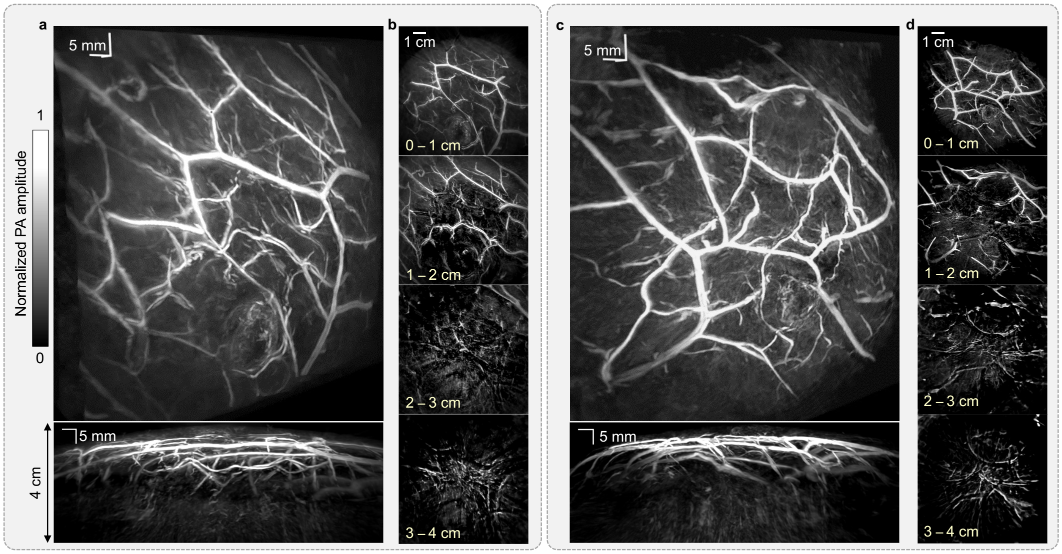

Figure 2.4: **3D-PACT of human breasts *in vivo*.** (a) Perspective angiogram of the right breast. Bottom: MAP side view showing 4 cm imaging depth. (b) Coronal MAPs from nipple to chest wall. Each slice shows a 1 cm-thick section. (c–d) Corresponding left-breast views.

available but lacks intrinsic optical absorption contrast; and MRI, though powerful, is slow, costly, and less accessible. PACT presents a valuable complement, leveraging optical absorption contrast with ultrasonic resolution and fast volumetric imaging [9], [49], [50].

To evaluate the translational capability of the 3D-PACT platform, we imaged both breasts of a healthy female volunteer (31 years old; 36C breast size). The system was positioned beneath a prone imaging bed with minimal separation. The target breast was gently compressed by a thin plastic cup to reduce illumination path length from nipple to chest wall, thereby improving penetration and SNR.

A full volumetric dataset was acquired in a single 10 s breath hold by rotating the 1024-element hemispherical array through a 90° arc. The detection geometry captured photoacoustic signals from virtually all angular directions, enabling accurate 3D reconstruction throughout the 4 cm-deep volume.

Figure 2.4a displays rendered angiograms of the right breast, including a side-view maximum-amplitude projection (MAP). Corresponding coronal slices in Fig. 2.4b span from the nipple to the chest wall, with clear visualization of superficial vasculature and smaller deep-lying vessels. Similar quality was obtained for the left breast (Figs. 2.4c and d), with apparent vessel diameters as small as 400 µm.

The imaging depth achieved by 3D-PACT results from careful engineering of the illumination and detection subsystems. At 1064 nm, tissue attenuation is dominated by scattering with a modest absorption component. For breast tissue, the 1 e-attenuation coefficient is approximately 0.9 cm^{-1} [51], [52], comparable to X-ray attenuation in soft tissue and significantly more favorable than wavelengths below 950 nm. Hemoglobin provides strong endogenous contrast, with vascular density and oxygenation serving as indicators of tumor perfusion, angiogenesis, and treatment response [53]–[55]. These factors together make 1064 nm an effective compromise between safety, penetration, and contrast.

The system's panoramic aperture further improves deep-tissue detection. Sparse or planar arrays often struggle with limited-view artifacts and degraded CNR at depth. In contrast, the hemispherical-rotational geometry maintains angular completeness and minimizes reconstruction ambiguities. Dual-speed-of-sound reconstruction reduces depth-dependent blurring caused by acoustic mismatch between water and tissue. Together, these features enable consistent spatial resolution over the entire imaging volume.

To produce the final breast angiograms, raw photoacoustic data from all 1024 channels and all scanning angles were first bandpass-filtered (0.3–3.5 MHz) to remove low-frequency drift and electronic noise. Detector-dependent temporal delays were corrected based on calibration measurements. The dual-SoS back-projection algorithm mapped the signals into a uniform 3D grid (512^3 voxels).

Following reconstruction, several post-processing steps were applied:

- Depth compensation. Because deeper regions receive lower fluence, reconstructed intensities were multiplied by an exponential factor matched to the measured effective attenuation coefficient of breast tissue.
- Denoising. Collaborative filtering (3D non-local means) was applied to suppress background noise while preserving vessel edges.
- Vessel enhancement. A multi-scale Frangi filter emphasized tubular structures and improved visualization of small vasculature.

This pipeline was crucial for obtaining high-quality images at 4 cm depth. Without depth compensation and vessel enhancement, vascular clarity diminished significantly in deep slices.

The volumetric angiograms show that most large vessels reside within 2 cm beneath the skin, consistent with angiographic maps derived from anatomical studies [56], [57]. These vessels primarily originate from the lateral thoracic, internal thoracic, and intercostal systems. Deeper vessels near the chest wall are typically smaller, more perpendicular to the skin, and more densely branched. 3D-PACT successfully visualizes these deeper networks, which are often invisible in optical imaging and difficult to capture using traditional breast ultrasound.

To further evaluate sensitivity to small absorptive inclusions, we constructed breast-mimicking phantoms with tissue-relevant optical properties. Tumor phantoms with absorption coefficient $\mu_a = 0.105\ \text{cm}^{-1}$, representing a 2.1-fold increase over background ($\mu_a = 0.05\ \text{cm}^{-1}$), were embedded at 2 cm depth. Reduced scattering was set to $\mu_s' = 5\ \text{cm}^{-1}$, matching typical values for human breast at 1064 nm [39], [51].

3D-PACT successfully resolved absorptive inclusions down to 1 mm in diameter. These results suggest that, beyond vascular imaging, the system may be sensitive enough to detect small high-contrast lesions in vivo, especially when combined with spectral imaging or molecular contrast agents.

The real-time acquisition workflow was designed to minimize subject motion and ensure reproducibility:

- Breath-hold imaging (10 s) suppresses respiratory motion and eliminates the need for gating.
- The plastic holding cup stabilizes breast position without discomfort.
- Illumination remains spatially stable across all rotational positions, which is essential for scatter-dominated tissues such as breast.

The system's safety profile is favorable: 1064 nm illumination lies within ANSI permissible exposure limits, and no ionizing radiation or exogenous contrast agents are required. These factors collectively make 3D-PACT attractive as a potential adjunct to mammography, ultrasound, or MRI in breast imaging workflows.

The demonstrated 4 cm penetration depth, near-isotropic 0.4 mm resolution, rapid volumetric acquisition, and rich endogenous contrast show that 3D-PACT is well positioned for breast imaging applications. While current implementation focuses on angiographic contrast, integration of multi-wavelength illumination, improved pulse energies, and more advanced reconstructions could extend the modality to tumor detection, oxygenation mapping, and treatment monitoring. The reconstruction and post-processing pipeline was instrumental in achieving the image quality presented here, making high-speed 3D-PACT a viable platform for future translational research in breast imaging.

2.5 Discussion

The 3D-PACT platform introduced in this chapter demonstrates that panoramic acoustic detection, stable near-infrared illumination, and high-channel-count acquisition can be integrated into a compact system capable of rapid and high-resolution volumetric imaging across a wide range of biological scales. By combining a densely sampled hemispherical array, dual-speed-of-sound reconstruction, and carefully regulated illumination at 1064 nm, the system consistently achieves deep penetration, isotropic spatial resolution, and high image quality.

The results shown across rodent brain, rodent body, and human breast imaging illustrate that the system performs robustly under diverse and demanding conditions. In small-animal imaging, the high imaging speed enables whole-brain functional mapping at 0.5 Hz while preserving fine vascular structures. The ability to resolve hemodynamics at the level of individual vessels provides a level of detail that complements and extends functional MRI, which typically resolves slower hemodynamic processes at coarser spatial resolution. For abdominal imaging, time-gated reconstruction effectively compensates for respiratory and cardiac motion, revealing structural and functional details that would otherwise be lost.

In human breast imaging, the 1064 nm illumination and large-aperture detection enable penetration up to 4 cm within a single breath hold. This allows rapid acquisition of high-quality angiograms that visualize both superficial and deep vasculature, including vessels adjacent to the chest wall. Such performance is challenging to achieve with purely optical techniques and typically requires significantly longer acquisition times with MRI. The combination of deep optical contrast, rapid volumetric capture, and absence of ionizing radiation makes 3D-PACT a compelling candidate for clinical translation.

Several engineering principles from the 3D-PACT system have broader implications for PACT design:

- Illumination uniformity. PACT reconstruction assumes that the light fluence pattern remains stable throughout scanning. Violations of this assumption lead to reconstruction inconsistencies and shadowing artifacts. The dual-diffuser optical pathway, combined with a fixed illumination axis, ensures that fluence remains effectively invariant across all angular positions. This design proved essential for high-quality breast imaging, where scattering is significant.

- Large detection aperture. A wide detection solid angle minimizes limited-view artifacts and improves sensitivity to structures oriented in all directions. The hemispherical–rotational geometry used here yields nearly panoramic coverage, enabling isotropic resolution and consistent contrast across the volume.
- Analog front-end integration. Weak photoacoustic signals from deep structures benefit significantly from pre-amplification before long cable runs. Directly integrating low-noise amplifiers beneath the detector arrays improved noise-equivalent sensitivity and image clarity, especially in breast imaging.
- Spatial Nyquist sampling. Adequate detector density and rotation-step spacing are critical to avoid aliasing and preserve FOV [38]. The system was designed to meet Nyquist criteria for both small and large imaging targets, which contributed to its robust performance across applications.
- Imaging speed. Rapid volumetric imaging reduces motion artifacts and enables functional studies. Even though the system does not yet provide instantaneous snapshots, coordinated mechanical scanning and fast acquisition allow dynamic processes such as rat-brain hemodynamics to be measured volumetrically.

While the system achieves state-of-the-art performance, several avenues can extend its capabilities:

- Spectral imaging. Incorporating multi-wavelength illumination would enable oxygenation mapping and molecular imaging using endogenous and exogenous absorbers [58].
- Higher repetition-rate lasers. Increasing the laser rate to 100 Hz or higher would allow faster volumetric imaging or larger FOVs in the same acquisition time.

- Faster mechanical scanning. Replacing the stepper motor with a high-torque servomotor could reduce scan times significantly.
- Higher-power laser delivery. Larger illumination areas could be achieved with more energetic pulses or multiple-beam combinations, improving coverage in human imaging.
- Awake small-animal imaging. By adapting the array geometry and animal holder, it may become possible to image awake rodents, similar to awake-mouse PAM systems [44].
- Clinical integration. The system's modularity facilitates co-registration with ultrasound, enabling hybrid optical–ultrasound imaging platforms with enhanced diagnostic value.

The 3D-PACT system presented here represents a major step toward truly versatile volumetric photoacoustic imaging. Its ability to visualize anatomical detail, functional hemodynamics, and deep tissue structures across multiple species demonstrates that high-speed, high-resolution 3D PACT is feasible on both preclinical and translational scales. The engineering insights gained from developing the system—particularly in illumination stability, panoramic detection, and reconstruction fidelity—provide a blueprint for future generations of PACT systems aimed at clinical adoption.

In summary, 3D-PACT merges deep penetration, high sensitivity, rapid acquisition, and rich optical contrast into a unified imaging platform. These capabilities position the system not only as a powerful tool for neuroscience and cardiovascular research, but also as a promising modality for clinical applications such as breast imaging, neonatal imaging, and beyond.

Chapter 3

NON-INVASIVE 3D PACT OF RAT LIVER AND HEART

[1] L. Lin†, X. **Tong**†, S. I. Cavallero, Y. Zhang, S. Na, R. I. Cao, T. K. Hsiai, and L. V. Wang, “Non-invasive photoacoustic computed tomography of rat heart anatomy and function,” *Light: Science & Applications*, 2023. DOI: `10.1038/s41377-022-01053-7`,

[2] X. **Tong**†, L. Lin†, P. I. Hu, R. I. Cao, Y. Zhang, J. Olick-Gibson, and L. V. Wang, “Non-invasive 3d photoacoustic tomography of angiographic anatomy and hemodynamics of fatty livers in rats,” *Advanced Science*, 2023. DOI: `10.1002/advs.202205759`,

3.1 Motivation

Cardiovascular disease remains the leading cause of morbidity and mortality worldwide, accounting for approximately 16% of total deaths [59]. Preclinical imaging of small-animal models plays a central role in understanding cardiac disease mechanisms and developing therapeutic strategies [60], [61]. Over the past several decades, non-invasive imaging of small animals has provided *in vivo* insights into structural and functional cardiac phenotypes with physiological and clinical relevance. Widely used modalities include light-sheet fluorescence microscopy [62], echocardiography [63], magnetic resonance imaging (MRI) [64], X-ray computed tomography (CT) [65], positron emission tomography (PET) [66], and single-photon emission computed tomography (SPECT) [67], as well as multimodal combinations such as microPET/CT and SPECT/CT [68]–[70]. Each modality offers a characteristic combination of penetration depth, spatial/temporal resolution, and contrast, and combinations of complementary techniques are often needed to cover the trade-offs between FOV, dynamic range, and phenotype characterization. Echocardiography, for example, is portable and well suited for real-time functional assessment of chamber contraction and valve motion, whereas CT and MRI provide larger FOV and/or finer spatial resolution for detailed anatomy and vascular imaging [65], [71].

In parallel, non-alcoholic fatty liver disease (NAFLD), also termed metabolic (dysfunction) associated fatty liver disease, has become the most common chronic liver disease in developed countries. In the United States, roughly 30% of the population is affected, with projections approaching 100 million cases by 2030. NAFLD spans a spectrum from simple steatosis to non-alcoholic steatohepatitis (NASH), which can progress to fibrosis, cirrhosis, and hepatocellular carcinoma. NAFLD is tightly linked to cardiometabolic comorbidities, including cardiovascular disease, hypertension, and dyslipidemia. Despite significant progress, the pathogenesis of NAFLD remains incompletely understood, and early, accurate, non-invasive diagnosis across the disease spectrum is still challenging.

Diagnostic techniques for NAFLD include biopsy, MRI, ultrasonography (US), and X-ray CT. Conventional US is widely adopted clinically due to low cost and portability, and recent advances such as shear-wave elastography, ultrafast power Doppler imaging, and ultrasound localization microscopy [72] have substantially improved sensitivity to stiffness and microvasculature, although many implementations require microbubble injection or long acquisition times for volumetric angiography with large FOV. CT provides high-resolution volumetric images, but exposes patients to ionizing radiation and offers limited soft-tissue contrast. MRI and magnetic resonance elastography provide accurate quantification of liver fat and stiffness, but they are cost-intensive, time-consuming, and incompatible with some implants. Liver biopsy remains the reference standard for detecting steatohepatitis and fibrosis, yet it is invasive, expensive, and subject to sampling error and procedure-related morbidity and mortality. These limitations motivate the development of new non-invasive biomarkers and imaging techniques that can characterize both hepatic structure and function.

Complementary to these established modalities, PACT combines optical absorption contrast with ultrasonic detection. Compared with echocardiography, PACT provides physiologically relevant optical contrast and reduced speckle artifacts; compared with MRI, PACT offers higher imaging speed and the potential for more compact, portable systems; and unlike X-ray CT, PACT uses nonionizing illumination while still resolving vascular and soft-tissue structures. However, translating PACT to non-invasive imaging of detailed cardiac and hepatic phenotypes faces several challenges. For cardiac imaging, ribs and lungs partially block and distort PA signals; highly absorptive myocardium attenuates light propagation into deeper chambers; and periodic heartbeats require motion correction or gating to avoid blurring and preserve intrinsic spatial resolution [73]–[77]. For liver imaging, prior preclinical PACT and PAT systems have been limited by insufficient sampling density and restricted detection angle, impeding visualization of fine hepatic vasculature *in vivo* at high speed and without exogenous contrast agents. As a result, most previous studies either focused on *ex vivo* cardiac preparations [78], [79] or provided incomplete volumetric liver angiograms.

Here, we build on a recently developed high-speed 3D-PACT platform [10] and apply it to non-invasive imaging of both rat hearts and livers. The system employs a hemispherical detection aperture with four rotating arc-shaped ultrasonic arrays and 1064 nm illumination, providing dense, quasi-isotropic sampling of PA signals over a large FOV. By combining ECG-guided time-gating for the heart with respiration-based time-gating for the liver, we suppress motion artifacts and obtain high-quality volumetric images and time-resolved movies. Using Zucker obese and age-matched lean rats, as well as hypertensive rats, we extract structural and functional metrics from both organs, including ventricular wall thickness, chamber volume dynamics, hepatic vessel density and irregularity, and hemodynamic changes in major vessels. These results demonstrate that 3D-PACT can serve as a unified, non-invasive platform for cardio-hepatic phenotyping in small-animal models, with potential for translation to neonatal and pediatric human imaging.

3.2 3D-PACT system design and time-gated reconstruction

Both cardiac and hepatic imaging experiments were performed on the same high-speed 3D-PACT platform. The core system is illustrated in Fig. 3.1. For illumination, a 1064 nm Nd:YAG laser (50 Hz repetition rate) delivers short pulses that are expanded by a diffuser mounted at the bottom of the hemisphere. The diffused beam passes through an optical window within the aperture and illuminates the region of interest. The acoustic aperture is covered by a transparent membrane that separates the water-filled housing from the animal while maintaining acoustic coupling. The choice of 1064 nm exploits reduced scattering in tissue compared with shorter near-infrared wavelengths [80] and provides strong absorption contrast from oxyhemoglobin and myoglobin [81], [82].

During imaging, anesthetized rats are placed on a heating pad above the aperture. The animals are positioned prone, with the chest centered over the optical window (Fig. 3.1b); abdominal hair is removed before imaging. A one-way scan consists of 500 mechanical steps and takes approximately 10 s, corresponding to 500 laser pulses and 500 sets of multi-channel PA data. Round-trip scanning is preferred to increase sampling density for time-gated reconstruction.

The hemispherical detection aperture provides a large solid-angle view, which mitigates acoustic blockage and distortion from ribs and lungs in the thorax and from

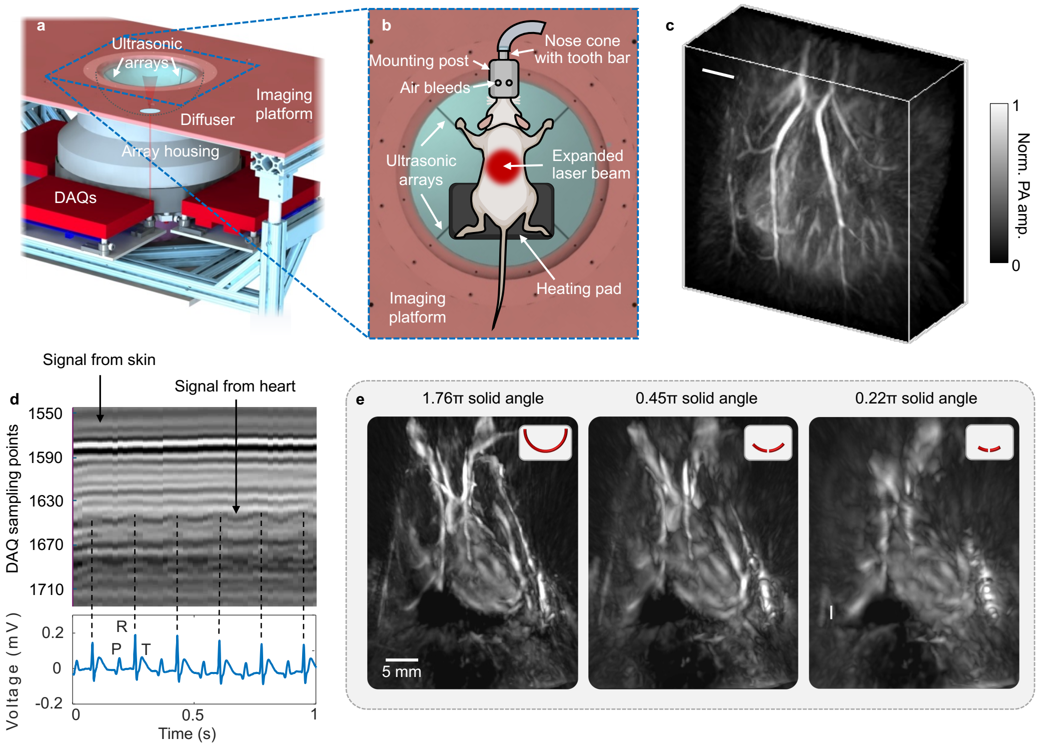

Figure 3.1: **Schematics and performance of the 3D-PACT system for hepatic and cardiac imaging.** (a) Schematic of the 3D-PACT imaging system. The 1064 nm laser beam is expanded by a diffuser fixed on the bottom of the hemisphere. (b) Close-up view of the imaging aperture for rat experiments. The rat is placed on a heating pad with its liver or heart at the center of the expanded laser beam. Two of the four arc-shaped ultrasonic transducer arrays are marked. (c) Orthogonal projection of a rat liver imaged by 3D-PACT. Scale bar, 5 mm. (d) Example of synchronized 3D-PACT (top) and ECG (bottom) signals for cardiac imaging. The PA diagram shows signal amplitude versus scanning step (time) and time-of-flight (vertical axis). R-waves in the ECG mark ventricular contraction, used for time-gating. (e) Reconstructed rat heart images with different ultrasonic detection apertures, illustrating the improvement in image quality with larger solid-angle coverage.

heterogeneous abdominal tissues. By combining signals from many view angles, the system improves image quality compared with limited-view geometries (Fig. 3.1e). Data are reconstructed using a universal back-projection (UBP) algorithm, with a dual-speed-of-sound model for liver imaging (see below) to account for different sound speeds in water and tissue.

Rapid periodic heart motion during the 10 s scan would cause severe motion artifacts if reconstructed naïvely. To address this, we synchronize 3D-PACT acquisition with the electrocardiogram (ECG) and apply time-gated reconstruction. An ECG electrode is instrumented with a synchronization marker such that a large spike is injected at the start of data acquisition, precisely aligning the ECG and PA data streams.

During each 10 s scan, the heart beats at $\sim$ 5 Hz [83], yielding roughly 11 laser pulses (scanning steps) per cardiac cycle at 50 Hz. We divide each cardiac cycle of duration T into 11 phases and assign each laser pulse to one phase according to its temporal offset from the nearest R-wave (Fig. 3.1d). For a given phase (e.g., end-diastole), we collect all PA data from that phase across multiple cycles and reconstruct a volumetric image. Repeating this procedure over all phases yields a 4D dataset describing the heart over one nominal cardiac cycle (Fig. 3.2a).

Phase 1 (time 0) is reconstructed from data gated to the R-waves and corresponds to early systole. The heart remains largely in systole from $T/11$ to $6T/11$, then relaxes, consistent with the Wiggers diagram. Mapping PA signal fluctuations across the heart reveals more pronounced motion near the apex than near the base.

For liver imaging, respiratory and cardiac motion generate oscillatory stripes in the raw PA data that blur volumetric reconstructions. Rather than treating these motions solely as artifacts, we use them in two ways: first, to remove motion-affected frames for high-quality static angiograms, and second, to reconstruct dynamic movies of respiratory motion.

For static hepatic angiography, we apply a time-gating (TG) approach by identifying frames heavily affected by respiration or heartbeat and removing them before reconstruction. Round-trip scanning is used to increase sampling density; signals from forward and backward scans are combined after TG to improve SNR and sampling. Time-gated reconstruction substantially suppresses motion-induced blurring and yields motion-artifact-free volumetric images that resolve vasculature down to apparent diameters of $\sim 380\,\mu$m.

To visualize respiratory motion and associated hemodynamics, we instead embrace the periodic breathing pattern. The raw PA signal from each transducer exhibits repeated cycles composed of inspiration and expiration (Figs. 3.8a and b). Each respiration cycle is divided into multiple phases; signals corresponding to the same phase across all cycles are summed (again incorporating round-trip scanning) and reconstructed to form a dynamic 4D sequence of liver angiograms. In addition, by correlating the respiration waveform with the temporal PA signal at each voxel, we obtain a 3D motion-contrast map highlighting voxels most strongly modulated by breathing (Fig. 3.8c).

3.3 Anatomy of rat liver and heart

Cardiac anatomy and depth-resolved visualization

Using ECG-gated 3D-PACT, we obtain clear volumetric images of the whole rat heart *in vivo*. Anterior views of the depth-encoded heart over one cardiac cycle are shown in Fig. 3.2a, with the heart highlighted at $4T/11$. Major vessels including the brachiocephalic artery, internal thoracic vessels, and intercostal vessels are resolved in addition to cardiac structures.

To visualize internal anatomy, we extract maximum-amplitude projections (MAPs) on sagittal and coronal planes (Figs. 3.2b and c). These cross-sections reveal the left and right ventricles, left and right atria, interventricular septum, pulmonary artery, aortic arch, and superior vena cava. Dynamic changes in chamber volumes between systole and diastole are readily observed: end-diastolic ventricular volume occurs near time 0, whereas maximal atrial filling appears around $6T/11$ (Fig. 3.2c).

Depth-encoded views further enable progressive "peeling" of superficial layers, from the chest wall to posterior cardiac structures (Fig. 3.2d). The primary sources of contrast are myoglobin-rich myocardium and hemoglobin-rich blood [81], [82], which provide strong PA signals at 1064 nm.

Hepatic anatomy and 3D angiography

With respiration-gated motion correction, the same 3D-PACT platform resolves hepatic vasculature in lean and obese rat livers *in vivo*. Maximum-amplitude projections from axial, sagittal, and coronal views are shown in Figs. 3.3a–c for a lean liver and Figs. 3.3e–g for an obese liver. Depth-encoded perspective projections highlight the three-dimensional organization of lobes and vessels (Figs. 3.3d and h).

At 1.2 cm depth below the liver surface, the CNR of a blood vessel with diameter $> 400\,\mu$m is approximately 5. In the coronal view, the median lobe, left liver lobe, inferior right lateral lobe, and caudate process are clearly identified, along with major vessels such as the superior epigastric vessels (SEV), hepatic portal veins (HPV), and their branches. As with the heart, PA contrast at 1064 nm is dominated by oxyhemoglobin, enabling detailed hepatic angiograms without exogenous contrast agents.

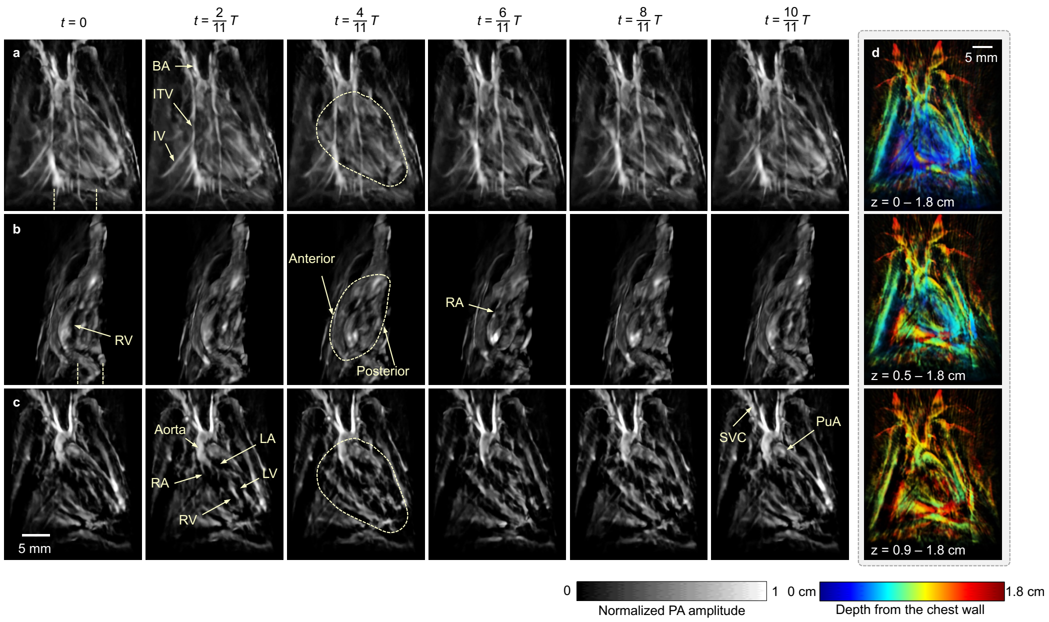

Figure 3.2: **Rat heart anatomy in 4D acquired by 3D-PACT.** (a) Anterior view of the heart over one cardiac cycle, with the heart highlighted at $4T/11$. BA, brachiocephalic artery; ITV, internal thoracic vessels; IV, intercostal vessels. (b) Sagittal cross-sectional images (maximum-amplitude projections, MAPs) of slices marked in (a), showing dynamic ventricular and atrial motion. (c) Coronal cross-sectional images (MAPs) of slices marked in (b), identifying the left atrium (LA), left ventricle (LV), pulmonary artery (PuA), right atrium (RA), right ventricle (RV), and superior vena cava (SVC). (d) Depth-encoded views at time 0, with superficial layers progressively removed to reveal posterior structures.

3.4 Feature extraction and quantitative comparison

To quantify structural and functional differences between groups, we extract features from motion-corrected volumetric datasets of both organs. For the heart, we focus on ventricular wall thickness and chamber volume dynamics, primarily comparing lean and obese Zucker rats, while hemodynamic metrics are evaluated across lean, obese, and hypertensive cohorts. For the liver, we extract both geometric and textural metrics—including liver volume, vessel density, angiographic irregularity, and estimated speed of sound—to distinguish lean and obese phenotypes.

Cardiac hypertrophy and volumetric function in obese rats

Using Zucker obese and age-matched lean rats, we demonstrate the capability of 3D-PACT to non-invasively assess obesity-induced hypertrophy and functional changes. In lean rats, typical cardiac cycles have 11 phases (11 phases / 50 Hz $\approx$ 0.22 s, i.e., a 4.55 Hz heart rate), whereas obese rats exhibited 9 phases per cycle (9 phases / 50 Hz

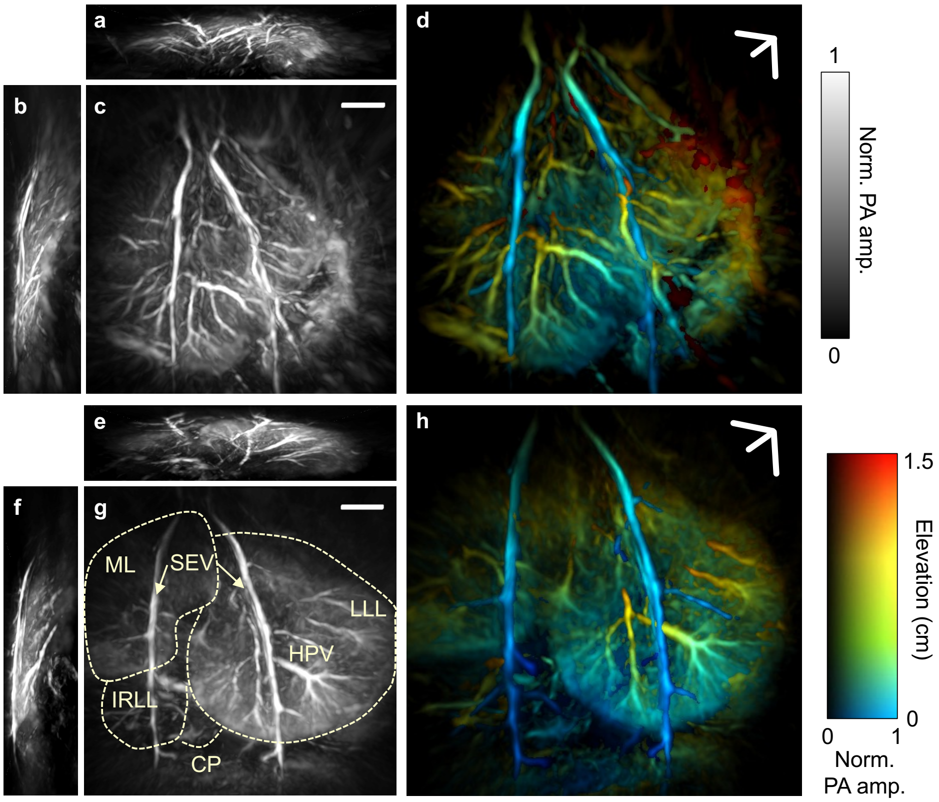

Figure 3.3: **3D-PACT of lean and obese rat livers *in vivo*.** (a–c) MAPs of a lean rat liver in (a) axial, (b) sagittal, and (c) coronal views. (d) Coronal perspective projection of the lean rat liver angiogram with depth encoding. (e–g) MAPs of an obese rat liver in (e) axial, (f) sagittal, and (g) coronal views. ML, median lobe. LLL, left liver lobe. IRLL, inferior right lateral lobe. CP, caudate process. SEV, superior epigastric vessels. HPV, hepatic portal veins. (h) Coronal perspective projection of the obese rat liver angiogram with depth encoding. Scale bars, 5 mm.

≈ 0.18 s, i.e., a 5.55 Hz heart rate), consistent with elevated heart rate supporting increased metabolic demands [84].

By sectioning the volume on the coronal plane (Figs. 3.4a and b), we observe concentric hypertrophy [85] in obese hearts, characterized by increased free-wall thickness in both left and right ventricles compared with lean controls. For quantitative wall-thickness measurements, we select a mid-ventricular coronal slice and compute the full-width-at-half-maximum (FWHM) of the PA signal across a ~ 1.3 mm wall segment. *Ex vivo* measurements of bisected hearts on the corresponding plane show good agreement with the *in vivo* estimates.

We also assess systolic and diastolic function by quantifying volumetric changes in ventricles and atria. Each heart is divided into 10 coronal sections of thickness

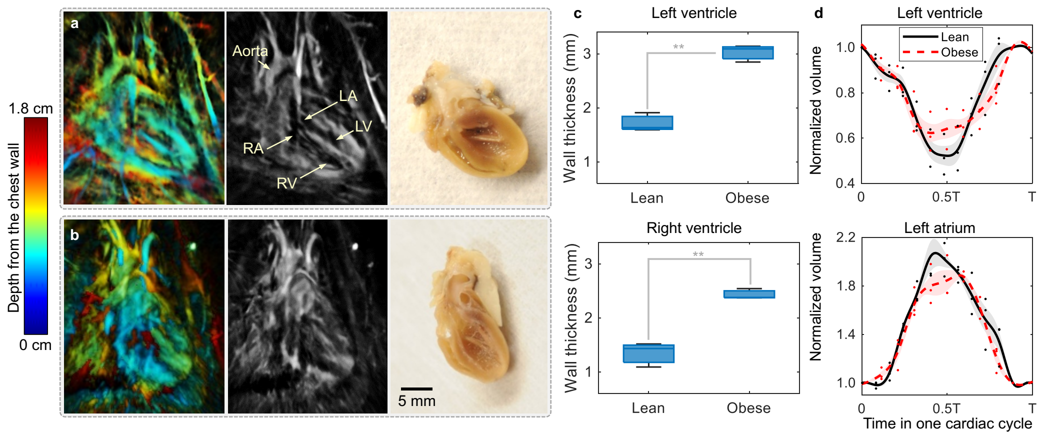

Figure 3.4: **Differences in cardiac anatomy and function between Zucker obese and lean rats.** (a) Depth-encoded cardiac anatomy of a Zucker obese rat. Left: 3D-PACT volume with color-coded depth; middle: coronal MAP; right: photograph of the corresponding hypertrophic heart after longitudinal sectioning. LA, left atrium; LV, left ventricle; RA, right atrium; RV, right ventricle. (b) Cardiac anatomy of a Zucker lean rat (control). (c) Free-wall thickness of left (top) and right (bottom) ventricles for obese vs. lean rats ($n = 3$, $p < 0.01$ for both). (d) Normalized left-ventricular and left-atrial volume variations over the cardiac cycle for obese vs. lean rats; shaded regions indicate standard deviation ($n = 3$).

1.04 mm, and ventricular and atrial regions are segmented in each slice. Volumes are then computed and normalized to their values at Phase 1 (end-diastolic phase) to reduce inter-animal variability ($n = 3$ per group). The resulting curves (Fig. 3.4d) show reduced normalized left-ventricular volume variation in obese rats, consistent with decreased ventricular strain or diastolic dysfunction in hypertrophic hearts [85]. Normalized left-atrial volume variation is likewise reduced in obese rats.

While detailed structural measurements were performed for lean and obese hearts, we note that the same ECG-gated volumetric framework can be used to extract analogous metrics in hypertensive rats. In the present work, hypertensive hearts are primarily characterized by their hemodynamic signatures (see Section 3.5), but the anatomical images support future extensions to wall-thickness and volumetric analyses in this cohort.

Hepatic structural metrics in lean and obese rats

For hepatic imaging, we use the same 3D-PACT configuration to image Zucker obese and lean rats (control group). Zucker obese rats are genetically predisposed models of metabolic-associated hepatic steatosis. Based on motion-corrected volumetric images, we extract five features to capture structural differences between groups: liver mask volume, vessel volume occupancy (VVO), vessel number density (VND), angiographic irregularity (AI), and estimated SoS (Fig. 3.5).

Liver masks and vessel masks are obtained via adaptive thresholding of raw and vessel-enhanced volumes (Fig. 3.5a). Liver mask volume reflects overall organ size and is compared between lean and obese rats ($n = 6$ per group) using one-tailed Welch's t-tests; obese livers exhibit significantly larger volumes ($p < 0.01$; Fig. 3.5d).

VVO is defined as the volume ratio between the binary vessel segmentation mask and the binary liver mask, representing the relative volumetric fraction of major vessels. VND is defined as the number density of vessel skeletons within the liver mask: centerlines are extracted from vessel masks, broken into individual vessel segments, and counted (Fig. 3.5b). Dividing the number of segments by the liver mask volume yields VND. Both VVO and VND are significantly reduced in obese livers ($p < 0.01$; Figs. 3.5e and f), indicating diminished vascular richness, likely due to fat accumulation and steatosis, particularly near hepatic and portal vein regions.

Angiographic irregularity (AI) is a composite metric designed to capture both local value distribution and directional morphology. AI is computed as the dot product of two intermediate maps: vessel distribution diversity (VDD) and morphological irregularity (MI) (Figs. 3.6a and b). VDD is obtained by scanning a sliding window across the volume, computing a normalized intensity histogram within each window, and assigning the entropy to the window center to form a 3D map M_{VDD}. MI is computed by scanning a sliding window on each slice, rotating the window from 0° to 180°, and performing singular-value decomposition (SVD); the MI at each voxel reflects the largest variation in the dominant normalized singular value across angles. Repeating this process over all three orthogonal slice orientations yields the 3D map M_{MI}. The AI map is then $M_{\mathrm{AI}} = M_{\mathrm{VDD}} \cdot M_{\mathrm{MI}}$ (Fig. 3.5c). AI is significantly different between lean and obese livers ($p < 0.01$; Fig. 3.5g), suggesting that fatty livers exhibit altered vascular patterning and signal distribution.

Finally, we estimate an effective tissue SoS by reconstructing images with a dual-SoS UBP algorithm [86], in which an ellipsoidal interface separates water and tissue. The SoS in water is fixed based on measured temperature. For each candidate tissue SoS, we reconstruct the volume and compute image sharpness as the mean amplitude in 3D spatial-frequency space (Fig. 3.6c). The SoS maximizing sharpness is taken

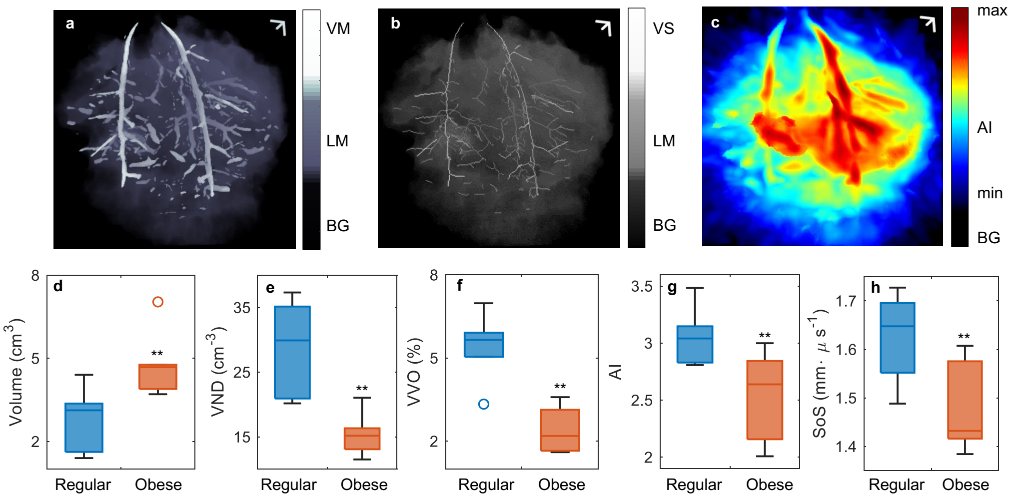

Figure 3.5: **Quantitative comparison between lean and obese rat livers.** (a) Coronal perspective projection of the binary liver mask and vessel segmentation mask. BG, background; LM, liver mask; VM, vessel mask. (b) Coronal perspective projection of the binary liver mask and vessel skeleton. VS, vessel skeleton. (c) Perspective projection of angiographic irregularity (AI) with the binary liver mask. (d–h) Statistical comparison of (d) liver mask volume, (e) VVO, (f) VND, (g) AI, and (h) estimated speed of sound (SoS) between lean and obese rat livers. Data are presented as box plots; p-values are calculated using one-tailed Welch's (unequal variances) t-tests. $^{**}p < 0.01$. Scale bars, 5 mm.

as the effective tissue SoS along the propagation paths to the liver. Comparison between lean and obese livers shows that SoS is significantly lower in obese livers ($p < 0.01$; Fig. 3.5h), consistent with ultrasound-based observations that fatty infiltration reduces sound speed.

3.5 Hemodynamics in heart and liver

Beyond static anatomy, 3D-PACT is particularly well suited for studying hemodynamics, because PA signal amplitude is highly sensitive to blood absorption and thus to blood volume, vessel caliber, and oxygenation. Here we analyze cardiac hemodynamics in lean, hypertensive, and obese rats and respiratory hemodynamics in hepatic vessels.

Cardiac hemodynamics in control, hypertensive, and obese rats

In representative cardiac images (Fig. 3.7a), we resolve large vessels including the aorta, pulmonary artery, right coronary artery (RCA), and left coronary artery (LCA). To quantify intravascular hemodynamics, we define regions of interest

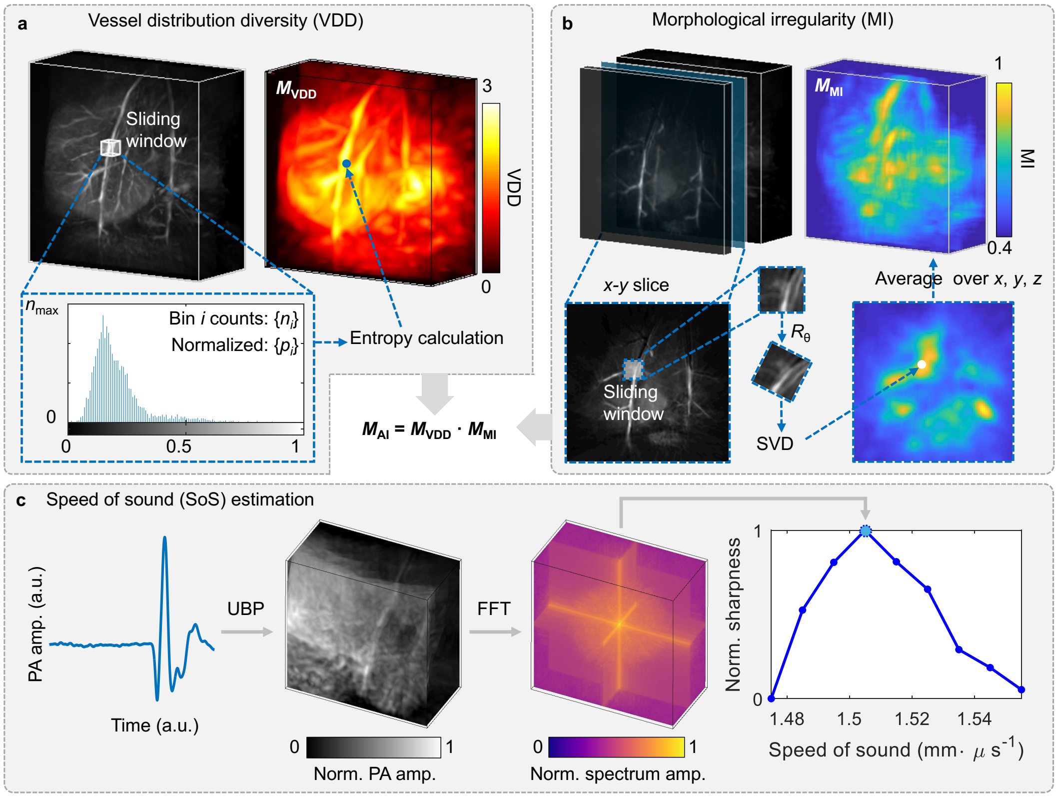

Figure 3.6: **Schematics of angiographic irregularity (AI) calculation and speed-of-sound (SoS) estimation.** (a) Vessel distribution diversity (VDD) calculation: a sliding window is scanned across the 3D image; at each position, the image histogram is acquired and entropy is calculated from normalized histogram counts. The value is assigned to the window center to form a 3D map M_{VDD}. (b) Morphological irregularity (MI) calculation: at each x–y slice, a sliding window is scanned and rotated from 0° to 180°; the dominant normalized singular value is recorded at each angle. The MI at the window center is assigned according to the largest difference in the dominant normalized singular value across angles. Similar processes over y–z and x–z slices yield the 3D map M_{MI}. AI is calculated as the dot product of the two maps, $M_{\text{AI}} = M_{\text{VDD}} \cdot M_{\text{MI}}$. (c) SoS estimation: the raw PA signal is reconstructed by UBP with different assumed tissue SoS values; a 3D fast Fourier transform (3D-FFT) yields the spectrum. Image sharpness is calculated as the mean spectrum amplitude, and the SoS maximizing sharpness is chosen as the estimated SoS.

(ROIs) slightly larger than each vessel lumen and average the PA amplitude along a 10-voxel ($\sim$ 1.3 mm) segment of the vessel axis. At 1064 nm, oxyhemoglobin dominates optical absorption (roughly an order of magnitude larger than deoxyhemoglobin) [87], so phase-dependent changes in ROI-averaged PA signals primarily

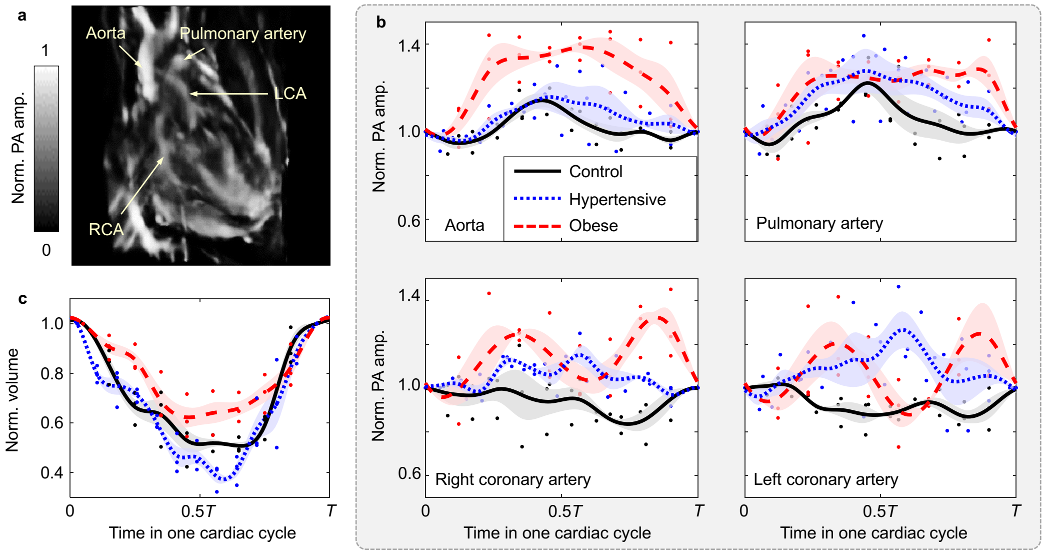

Figure 3.7: **Cardiac hemodynamics in control, hypertensive, and obese rats.** (a) 3D-PACT image showing the aorta, pulmonary artery, RCA, and LCA. (b) Normalized PA amplitude in the four vessels over the cardiac cycle for control (solid black), hypertensive (blue dashed), and obese (red dashed) rats ($n = 3$ per group). (c) Normalized left-ventricular volume over the cardiac cycle for the same groups, showing distinct systolic and diastolic behavior.

reflect variations in oxygenated blood volume (or vessel diameter) and oxygen saturation.

We first compare coronary perfusion in healthy, hypertensive, and obese rats. For the aorta and pulmonary artery, normalized PA amplitudes peak during ventricular systole ($\sim$ 0.4–0.5T), with slightly larger variations in hypertensive rats than in controls (Fig. 3.7b), consistent with altered ventricular volume changes (Fig. 3.7c). More pronounced fluctuations are observed in the left coronary arteries of hypertensive rats, which may arise from lipid accumulation and structural damage in coronary arteries, affecting perfusion [88].

In obese rats, obesity-associated hyperlipidemia and increased cardiac output [89] are accompanied by enlarged PA signal fluctuations in all four vessels (aorta, pulmonary artery, RCA, LCA) compared with lean controls (Fig. 3.7b). Statistically significant differences are found in RCA and aortic signals. Combined with hypertrophic anatomy and altered chamber volume dynamics (Fig. 3.4), these hemodynamic signatures highlight the potential of 3D-PACT to non-invasively phenotype cardiovascular disease in both hypertensive and obese models.

Respiration-gated hepatic hemodynamics

In the liver, respiratory motion modulates both vessel geometry and blood volume. Using the respiration-based TG scheme described above, we reconstruct dynamic volumetric sequences of the liver over the breathing cycle (Figs. 3.8a and b). Periodic deformation of lobes and vessels during inspiration and expiration is clearly visible.

From the raw signals, a repetitive breathing pattern is extracted and correlated with the temporal PA signal at each voxel to generate a motion-contrast map (Fig. 3.8c). Two representative voxels are selected, and their normalized PA amplitude changes over respiration phases are plotted (Fig. 3.8d); the two voxels exhibit anti-correlated patterns, reflecting their different positions relative to the diaphragm.

On an axial slice containing cross-sections of the SEV and HPV (Fig. 3.8c), we segment vessel cross-sections and compute their area changes over respiration phases (Fig. 3.8e). PA amplitudes from the upper and lower portions of SEV show opposite variations, consistent with SEV passing through the diaphragm and experiencing pivot-like motion along the z-axis. The liver as a whole moves more uniformly with the diaphragm. SEV shows larger area changes than HPV: SEV diameter increases during inspiration, consistent with the respiratory pump mechanism, in which negative intrathoracic pressure enhances venous return and outgoing flow from the heart. In contrast, HPV area changes remain relatively small, likely because HPV lies further from the thoracic cavity and its blood volume is buffered by extensive hepatic capillary networks.

These results demonstrate that 3D-PACT can capture respiration-related deformation and hemodynamics in major hepatic vessels without additional acquisition time or hardware, opening new opportunities to study portal hypertension and cardio-hepatic coupling in NAFLD and related diseases.

3.6 Discussion

This chapter presents a unified framework for non-invasive 3D-PACT of both rat heart and liver, using a single hemispherical imaging platform with organ-specific gating strategies. By combining ECG-guided TG for the heart with respiration-based TG for the liver, we obtain high-quality volumetric images and dynamic movies of two key organs implicated in cardiometabolic disease. The system resolves cardiac chambers and coronary vessels, as well as hepatic lobes and portal venous networks, with sufficient resolution and SNR to support quantitative analyses of anatomy, hemodynamics, and tissue properties.

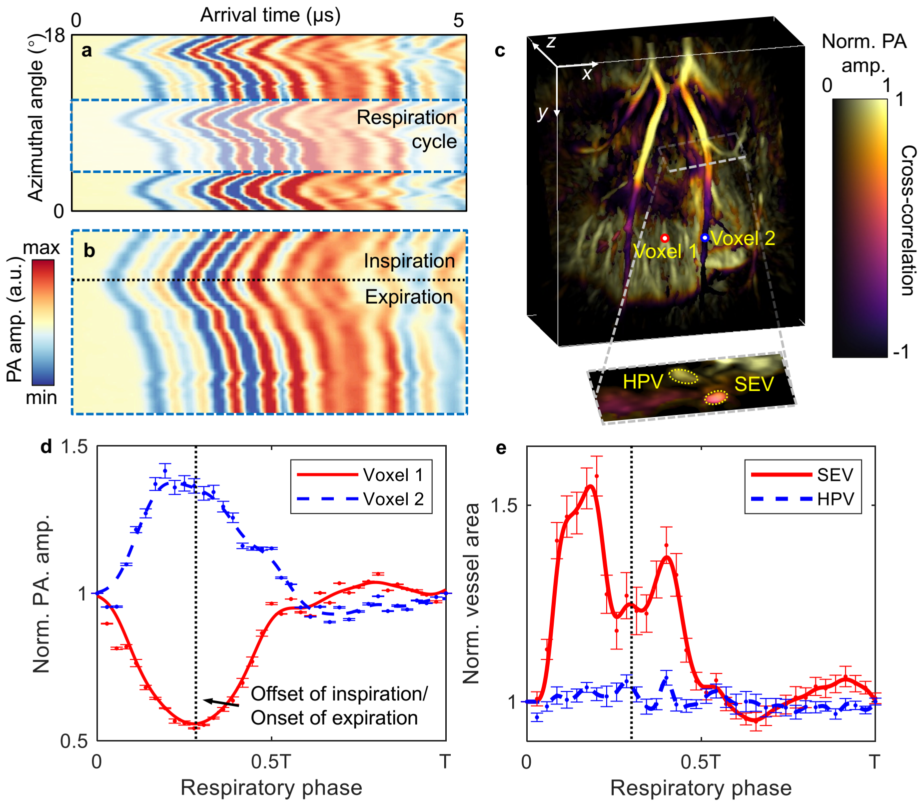

Figure 3.8: **Respiration-based TG schematics and hepatic hemodynamic results.** (a) Schematic of respiration-based time gating for dynamic imaging. The raw PA signal from one transducer shows periodic oscillations from breathing. (b) Close-up of one respiration cycle: each cycle is divided into multiple phases, and signals from the same phase across all cycles are summed (with round-trip scanning) for reconstruction. (c) Motion-contrast-encoded orthogonal projection of a rat liver, with a slice showing SEV and HPV cross-sections. (d) Relative PA signal changes for two voxels in (c), normalized to the first phase and plotted as mean ± standard error. (e) Relative changes of cross-sectional vessel areas (SEV and HPV) in (c), normalized to the first phase and plotted as mean ± standard error.

From the cardiac perspective, 3D-PACT addresses longstanding challenges in photoacoustic cardiac imaging, including acoustic disturbances from ribs and lungs, strong optical attenuation in myocardium, and motion artifacts from periodic heartbeats. The hemispherical detection aperture and regulated 1064 nm illumination promote deep penetration and mitigate rib-induced shadowing. ECG-guided phase-binned reconstruction yields 4D datasets in which intrinsic spatial resolution is maintained across the cardiac cycle. Leveraging these technical advances, we non-invasively quantify ventricular wall thickness, chamber volume dynamics, and vessel-specific hemodynamics in lean, hypertensive, and obese rats. The observed concentric hypertrophy and altered volume changes in obese hearts, along with vessel-specific PA fluctuations in hypertensive and obese rats, illustrate how 3D-PACT can phenotype structural and functional cardiac abnormalities relevant to human disease.

From the hepatic perspective, 3D-PACT provides high-speed, volumetric angiograms of the liver without exogenous contrast agents. Motion-corrected images exhibit clear lobar anatomy and resolve vessels down to $\sim 380\,\mu\mathrm{m}$ in diameter at depths of $\sim 1.2\,\mathrm{cm}$. Building on these images, we extract a panel of quantitative metrics—liver volume, VVO, VND, AI, and effective SoS—that collectively distinguish lean and obese livers with high statistical significance. VVO and VND capture reductions in vascular richness associated with steatosis; AI encodes changes in signal distribution and anisotropy that may be sensitive to early microvascular remodeling; and SoS provides a biophysical parameter linked to fat accumulation and fibrosis. Respiration-gated reconstruction additionally reveals dynamic deformation and area changes in SEV and HPV, suggesting that 3D-PACT can probe portal hemodynamics and mechanical coupling between liver and diaphragm.

Taken together, these cardiac and hepatic results emphasize several broader points. First, 3D-PACT offers organ-agnostic hardware that can be repurposed across different anatomical sites by adjusting animal positioning and gating schemes. This flexibility is particularly valuable for studying diseases such as NAFLD that are intertwined with cardiovascular and respiratory dysfunctions. Second, the combination of structural, functional, and textural metrics derived from a single modality creates a richer phenotyping space than any single metric alone, and may be especially powerful when integrated with machine learning or multivariate statistical models. Third, the same hardware and reconstruction pipeline can be adapted for hybrid imaging with pulse–receiver ultrasound, multi-wavelength spectroscopy, or advanced algorithms (e.g., fast-marching or model-based reconstructions) to further improve spatial resolution, quantitative accuracy, and specificity.

Several avenues remain for future work. On the cardiac side, arrays with higher center frequency (e.g., 5–10 MHz) could improve spatial resolution for mouse hearts and finer coronary branches, at the cost of increased attenuation and sensitivity to rib-induced distortions. Optimized array geometries (e.g., more arcs with fewer elements per arc) and faster scanning mechanisms could reduce acquisition times while preserving sampling density. On the hepatic side, multi-wavelength illumination and exogenous contrast agents (e.g., lipid-sensitive dyes or indocyanine green) could enable spectroscopic discrimination between fat, fibrosis, and perfusion, enhancing the specificity of NAFLD staging. More extensive animal studies spanning steatosis, steatohepatitis, fibrosis, and cirrhosis would allow the proposed metrics (VVO, VND, AI, SoS) and respiration-gated hemodynamics to be mapped onto histological and clinical endpoints.

Finally, the demonstrated 3D-PACT platform is directly relevant to translational imaging. The 2.25 MHz center frequency balances FOV, penetration depth, and resolution for large rodents and pediatric humans, and previous work has already shown $\sim$ 4 cm penetration in human breast imaging. With optimized illumination patterns (e.g., donut beams), higher-power or multi-laser sources, and refined mechanical design to position target organs closer to the optical window, similar or greater depths could be achieved for human liver and neonatal heart imaging. By providing high-speed, volumetric, nonionizing, and contrast-rich imaging of both cardiac and hepatic physiology, 3D-PACT has the potential to become a powerful tool for studying the cardio-hepatic axis and for guiding diagnosis and therapy in metabolic and cardiovascular disease.

Chapter 4

PACT OF BREAST CANCER IN RESPONSE TO NEOADJUVANT CHEMOTHERAPY

[1] L. Lin†, X. **Tong**†, P. I. Hu, M. Invernizzi, L. L. Lai, and L. V. Wang, "Photoacoustic computed tomography of breast cancer in response to neoadjuvant chemotherapy," *Advanced Science*, 2021. DOI: `10.1002/advs.202003396`,

4.1 Motivation

Breast cancer remains the second leading cause of cancer-related mortality in women in the United States, yet survival has improved substantially over recent decades [90]–[92]. These gains have been driven, in part, by systemic therapies increasingly tailored to the biological subtypes of breast cancer [90]–[93]. NAC—systemic therapy administered before surgery—has contributed to better clinical outcomes by increasing the rate of breast conservation [94], [95] and by providing prognostic information based on treatment response [96], [97]. Achieving a robust response to NAC is associated with improvements in both disease-free and overall survival [96], [97].

NAC response measurements also play an important role in evaluating new systemic therapies [98], [99]. In a subset of "exceptional responders," NAC essentially eradicates detectable tumor. For these patients, the risk of recurrence is low, with 5-year relapse-free survival rates of 95% and 94% reported for HER2-positive and triple-negative breast cancers, respectively [100]. Such findings raise the possibility of omitting definitive surgery in carefully selected patients and challenge the long-standing paradigm that solid tumors must always be surgically resected. This concept has motivated clinical trials investigating the safety of eliminating surgery in women who receive NAC and show an apparent complete response [101].

In current practice, there is no noninvasive imaging modality that can be used routinely to confirm complete response after NAC. Consequently, the presence or absence of residual disease is ultimately established by surgical excision and histopathological analysis. Standard clinical methods for monitoring response include physical examination, mammography, ultrasound, and MRI. These techniques largely rely on changes in tumor morphology and size, which may not reflect early or partial treatment effects. Furthermore, NAC can induce fibrosis and other tissue changes that obscure residual tumor, thereby degrading the performance of conventional imaging [102].

Accurately distinguishing responders from non-responders at an early and clinically actionable time point would significantly improve patient management. To that end, several functional and anatomical imaging approaches have been investigated, including fluorothymidine PET [103], CE-MRI with emphasis on vascular enhancement [104], and diffuse optical imaging (DOI) [105]. These modalities have shown that metabolic and hemodynamic measurements carry predictive value for therapy response. Nonetheless, PET and CE-MRI require contrast agents, specialized infrastructure (radioisotope handling or high-field magnets), and relatively long and costly imaging sessions, which limit their use for frequent monitoring. DOI is label-free and amenable to repeated measurements, but its relatively low spatial resolution [106] hinders adoption for detailed clinical evaluation. Taken together, these limitations motivate the development of new imaging techniques for assessing breast cancers treated with NAC.

PACT provides a complementary solution by combining the optical contrast of DOI with the high spatial resolution of ultrasound, while avoiding speckle artifact [14], [107]. Several groups have explored the use of PACT to monitor NAC response in breast cancer [108]–[110]. However, prior systems generally lacked sufficient spatial sampling and angular coverage to resolve individual vessels over the entire breast, which limited the reliability of retrieved biomarkers. Additionally, variations in breast positioning and deformation between visits introduce changes in light fluence that are difficult to model, thereby complicating quantitative measurements such as total hemoglobin concentration.

To overcome these challenges, we designed a single-breath-hold photoacoustic computed tomography (SBH-PACT) system that images the entire breast with detailed angiographic resolution within a single 15 s breath hold. This configuration allows us to visualize tumor-associated angiogenesis [9], a hallmark of tumor progression and metastasis [55], [111], [112]. Elevated expression of vascular endothelial growth factor has been linked to poor responses to chemotherapy [113], [114], further underscoring the value of vascular imaging. Because angiogenesis emerges early in the transition from benign hyperplasia to malignant disease, noninvasive longitudinal monitoring of tumor-associated microvasculature may aid early diagnosis in patients with abnormal screening findings. In this context, serial SBH-PACT imaging could help stratify indeterminate lesions and potentially reduce the number of required biopsies.

In this chapter, we evaluate the ability of SBH-PACT to characterize NAC response in three breast cancer patients imaged at three time points: before NAC, during treatment, and after treatment completion. We segment tumor regions and quantify changes in tumor dimensions, vessel density, entropy, and morphological irregularity. These metrics are benchmarked against the histopathology of the resected specimens. Our results demonstrate that SBH-PACT, conceptually akin to a contrast-free, high-speed, high-resolution version of CE-MRI, can capture treatment-related changes in tumor vasculature and size.

4.2 Evaluation of the SBH-PACT system with a breast-mimicking phantom

A schematic of the SBH-PACT system is shown in Fig. 4.1a. The patient lies prone on a bed with minimal separation from the imaging unit. A homogenized, circular laser beam is delivered from below and illuminates the breast, which is gently compressed against the chest wall. A full-ring ultrasonic transducer array encircles the breast and provides a panoramic in-plane view. A motorized linear stage translates the array along the elevational direction. Within a single 15 s breath hold, a complete volumetric data set is acquired, revealing angiographic structures across the entire breast and resolving vessels down to an apparent diameter of 258 μm [9].

Prior to clinical use, we characterized the system sensitivity using a breast-mimicking phantom (Figs. 4.1b and c). The bulk phantom was composed of 3% clear agarose, 0.0125% black acrylic ink, and 20% intralipid (3.6%) [115], chosen to approximate breast optical properties. Custom 3D-printed molds were used to fabricate a breast-shaped volume containing embedded tumor-mimicking inclusions. Seven absorbing inclusions were positioned at 2 cm depth, with designed diameters of 1, 1.5, 2, 2.5, 3, and 3.5 mm. The absorption coefficient of the inclusions (0.105 cm^{-1}) was set to be 2.1 times that of the background (0.05 cm^{-1}) [51], [116]. The reduced scattering coefficient μ_s' was 5 cm^{-1} at 1064 nm [51].

In the reconstructed MAP image (Fig. 4.1c), inclusions located near the lateral boundaries appear somewhat enlarged relative to their nominal sizes, likely due to minor ink diffusion during fabrication. Nonetheless, the system clearly resolves a 1 mm inclusion near the center at the correct depth, demonstrating the sensitivity required for detecting small abnormalities.

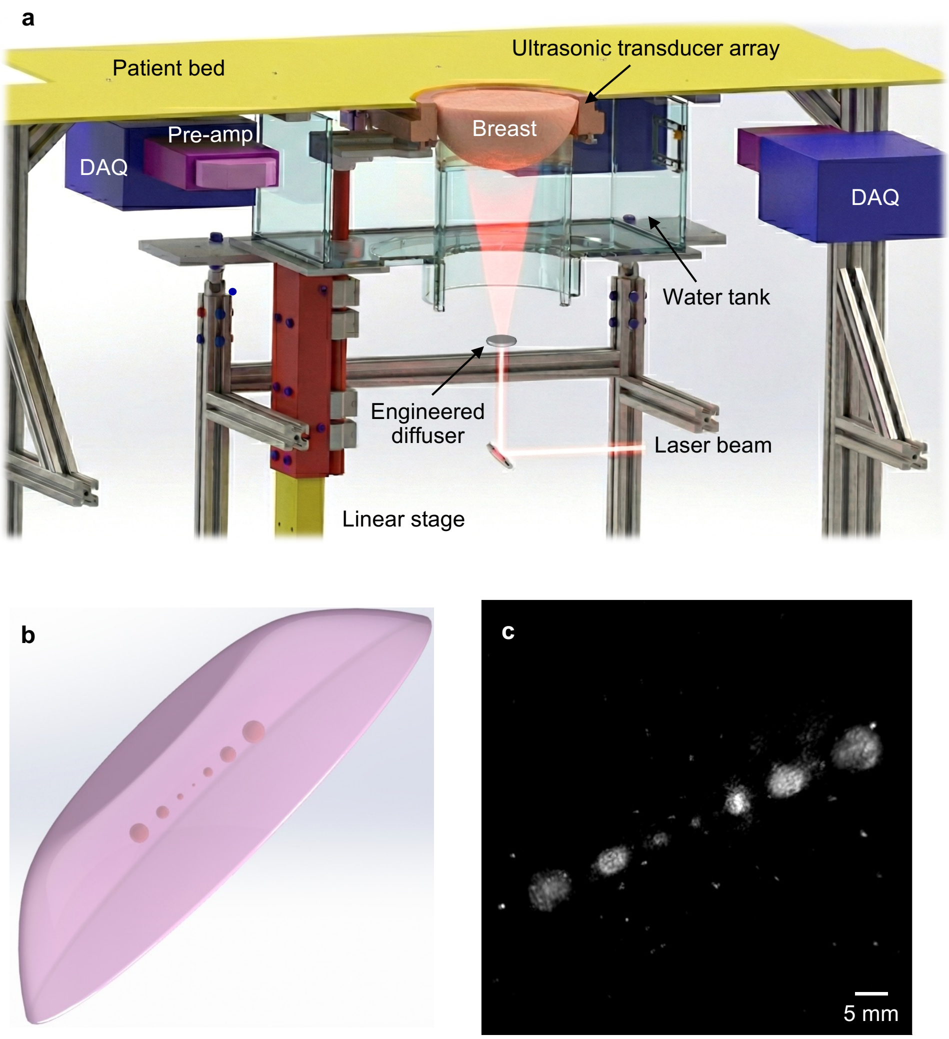

Figure 4.1: **Single-breath-hold photoacoustic breast imaging system and breast-mimicking phantom.** (a) Cut-away rendering of the SBH-PACT system, illustrating the patient bed, water tank, full-ring ultrasonic transducer array, and data acquisition modules. (b) Schematic of the breast-shaped phantom with embedded absorbing inclusions. (c) MAP image of the phantom acquired by SBH-PACT, demonstrating detection of a 1 mm-diameter inclusion at 2 cm depth.

4.3 Pilot clinical SBH-PACT studies with patient-reported outcomes

The clinical pilot study was designed to evaluate SBH-PACT in women with breast cancer undergoing NAC and to develop quantitative image-based metrics of treatment response. Four patients scheduled to receive NAC consented to participate. Due to the onset of the coronavirus pandemic, the study was halted after the first visit of the fourth patient, leaving three patients who completed the full imaging protocol across three time points (T1–T3), for a total of nine SBH-PACT sessions

($n = 3$). T1 corresponded to the pre-treatment baseline after diagnostic work-up and biopsy; T2 occurred after two cycles of chemotherapy; and T3 was acquired after completion of NAC but before surgery. SBH-PACT images were compared against conventional imaging (mammography, ultrasound, MRI) and the final surgical histopathology. All SBH-PACT reconstructions and analyses were performed blinded to clinical imaging and pathological results.

After each SBH-PACT exam, patients completed a brief survey regarding comfort and overall experience. In this small cohort, patients consistently rated SBH-PACT as more comfortable and easier to tolerate than MRI and mammography, and comparable in comfort to ultrasound. Among the three patients who completed all three visits, two had residual solid masses after NAC as seen on clinical exam or MRI (partial response), while one had no detectable mass on exam or MRI (complete clinical response).

4.4 SBH-PACT of breast cancer treated with NAC

Representative SBH-PACT images from a single patient at T1, T2, and T3 are shown in Fig. 4.2. Depth-encoded angiograms of the contralateral, clinically unaffected breast serve as an internal control (Fig. 4.2a). Across time points, the vascular architecture of the unaffected breast remained largely unchanged, indicating that systemic therapy did not produce gross vascular alterations in normal tissue at the imaging scale.

In the affected breast, the tumor is visualized as a region of increased vascular density (Fig. 4.2c). To highlight such regions, we extracted vessel skeletons from the MAP images and generated vessel density maps for each breast (Figs. 4.2b and d). Areas with the highest vessel density coincided with the clinically known tumor location (Fig. 4.2d). Over the course of NAC, SBH-PACT revealed a progressive reduction in both tumor size and associated vascular density, although this patient did not achieve a complete response. Elevated vessel density observed outside the pathologically confirmed tumor could be false positives or may represent additional early lesions not yet diagnosed [117].

In all three patients, the unaffected breasts sometimes contained foci of increased vascular density that were not apparent on standard imaging. Given the high sensitivity of SBH-PACT to microvasculature, some of these regions may correspond to subclinical neoplastic changes that are occult to conventional modalities, potentially contributing to the reported 11.3% rate of breast cancers detected only in resected

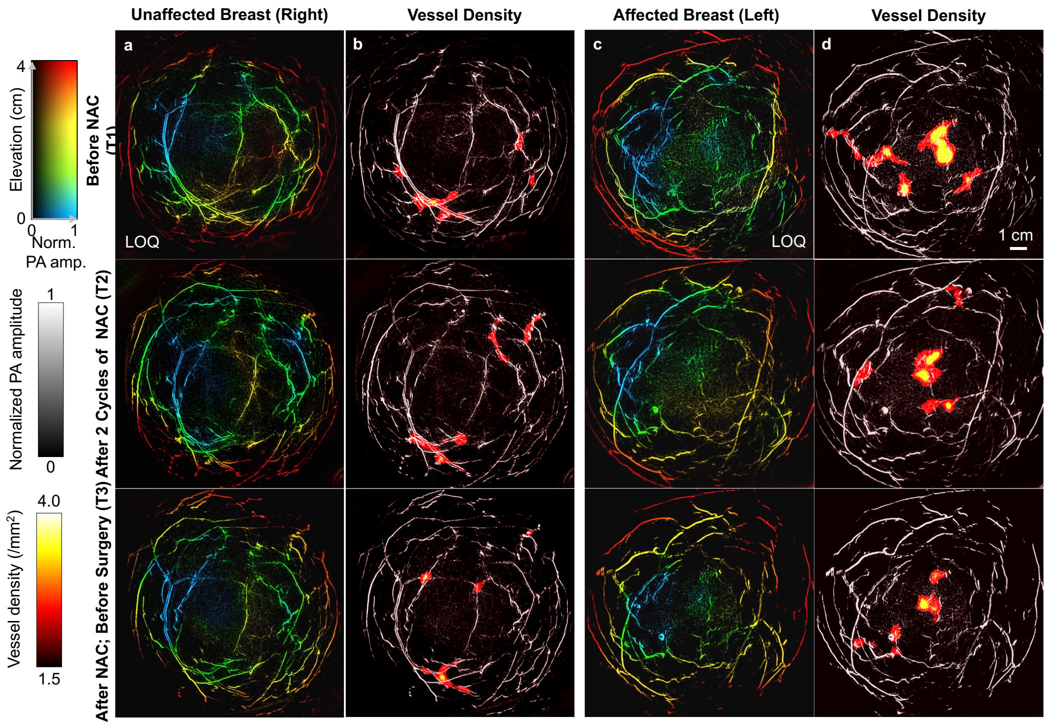

Figure 4.2: **Longitudinal SBH-PACT of a patient treated with NAC.** (a) Depth-encoded angiograms of the unaffected breast at three time points. (b) Corresponding vessel density maps overlaid on the MAPs in (a). (c) Depth-encoded angiograms of the affected breast. (d) Vessel density maps for the affected breast, highlighting regions of increased vascular density that localize the tumor.

specimens despite preoperative imaging [118]. On the other hand, these findings could also reflect benign vascular variations or reconstruction artifacts. In practice, such foci can be suppressed by increasing the vessel density threshold (e.g., to 2.5 mm^{-2}) and/or by discarding connected components smaller than a selected minimum area (e.g., 4 mm^2).

Figure 4.3 presents SBH-PACT angiograms from two additional patients. For Patient 2 (partial response; Fig. 4.3a), cancer-associated angiogenesis remained detectable at T3 despite a reduction in lesion size. Zoomed views demonstrate persistent, abnormal vasculature within the tumor region. For Patient 3 (Fig. 4.3b), who had a complete clinical response, tumor-associated vascularity decreased at T2 and was nearly absent at T3, in agreement with the near-pathological complete response established by histopathology.

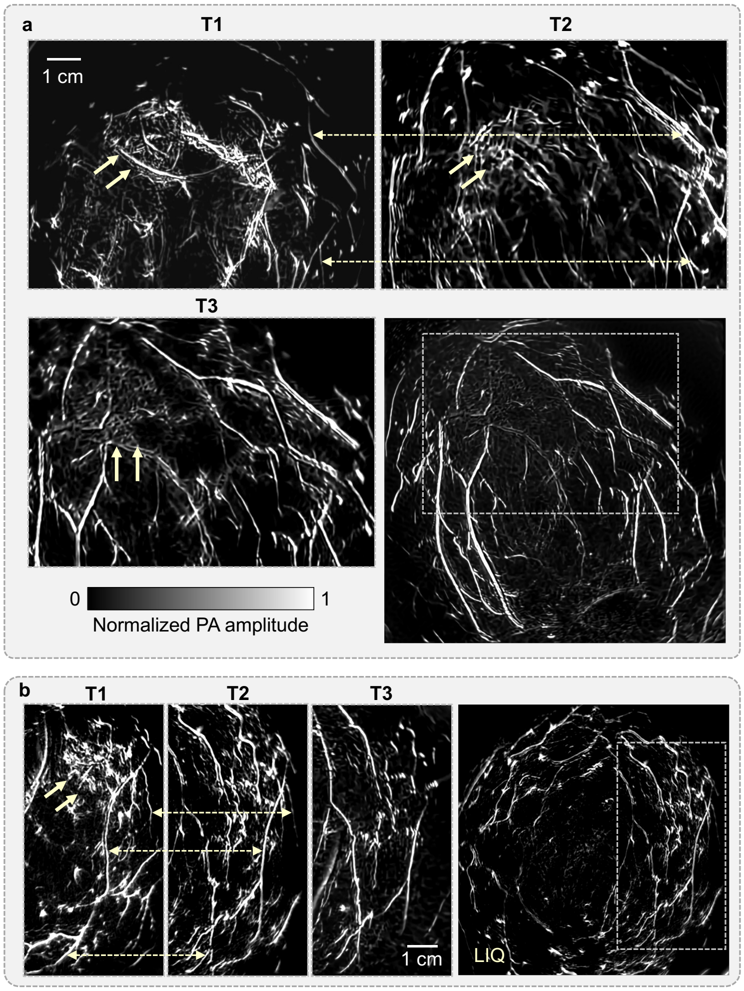

Figure 4.3: **SBH-PACT angiograms of two additional NAC-treated patients.** (a) Patient 2, who exhibited a partial response. Close-up views of the tumor region (yellow dashed boxes) show persistent angiogenesis at T3. Yellow arrows highlight cancer-associated vessels; magenta arrow lines trace prominent vessels observed at both T1 and T2. (b) Patient 3, who showed a complete clinical response. Cancer-associated vascular structures decrease markedly at T2 and are nearly absent at T3.

4.5 Breast cancer segmentation based on blood vascular irregularity

Vessel density alone does not fully capture the complexity of tumor vasculature. Malignant lesions typically exhibit highly disorganized vascular patterns, with irregular distributions and morphologies, compared with the more organized vasculature of healthy tissue. To quantify this, we first computed entropy maps from the SBH-PACT angiograms (Fig. 4.4a). Entropy measures local fluctuations in photoacoustic amplitude; higher values are found at vessel boundaries and in regions with complex vascular structures, including tumors.

In contrast, vessels in normal breast tissue tend to be smoother and more directional. To emphasize morphological irregularity, we estimated a measure of vascular anisotropy and used it to weight the entropy maps (Fig.4.4b). This procedure downweights highly directional structures typical of normal vasculature and enhances isotropic, irregular patterns more characteristic of tumor-associated vessels.

For automated segmentation, we binarized the anisotropy-weighted entropy maps using a threshold defined as the mean plus 1.4 times the standard deviation of the entire breast image. This threshold was empirically chosen to produce segmented tumor sizes that closely matched MRI measurements. We then selected the largest contiguous region in the resulting binary mask as the tumor region (Fig. 4.4c). These masks were used to compute tumor dimensions and track their evolution over the three imaging time points.

4.6 Measurements of cancer characteristics to evaluate response to NAC

To further enhance visualization of tumor-associated vasculature, we used the anisotropy-weighted entropy maps as modulation masks for the original angiograms (Fig. 4.5a). This emphasizes irregular vessels in and around the tumor while attenuating background vasculature. Because the breast is positioned differently in SBH-PACT and MRI, we rotated MRI images to an intermediate orientation between craniocaudal and mediolateral views such that the tumor and major vessels spatially aligned with SBH-PACT projections. When displayed side-by-side (Fig. 4.5b), SBH-PACT and MRI show consistent changes in tumor size and partial treatment response between T1 and T3. However, only SBH-PACT provides detailed microvascular information within and surrounding the lesion at high temporal resolution (single 15 s breath hold).

In our SBH-PACT system, the in-plane spatial resolution is approximately 255 μm, whereas the elevational resolution is about 5.6 mm [9]. Within tumor regions, vessels tend to cluster in depth (similar color in depth-encoded images, e.g., Fig. 4.2c). We therefore performed quantitative analysis on 2D MAP images obtained by projecting along the elevational axis. Given the relatively low blood volume fraction in normal breast tissue [119], these MAP images capture most clinically relevant vascular features. In the long term, fully isotropic 3D quantification will require further improvements in elevational resolution.

To quantify NAC response, we defined a region of interest (ROI) encompassing the tumor area in the T1 SBH-PACT image and applied the same ROI to coregistered

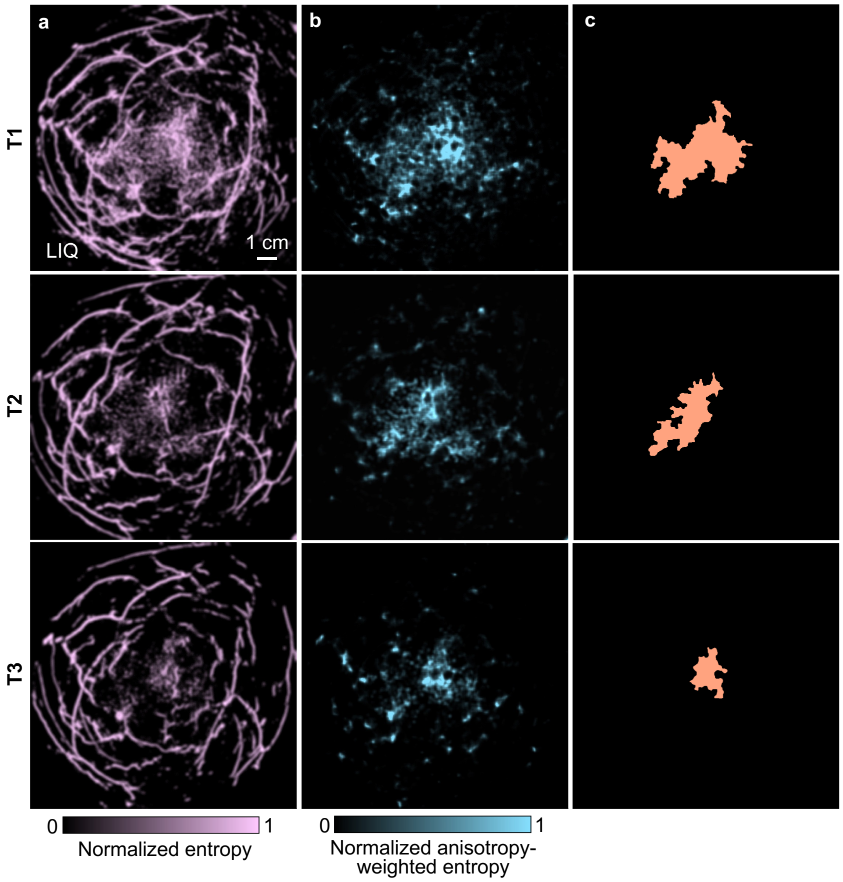

Figure 4.4: **Tumor segmentation based on vascular irregularity for one patient across three time points.** (a) Entropy maps derived from the breast angiograms. (b) Anisotropy-weighted entropy maps that suppress directional vessels in healthy tissue and highlight disordered vascular regions. (c) Segmented tumor regions obtained from (b), illustrating progressive shrinkage with NAC.

images at T2 and T3. Figure 4.6 summarizes the resulting metrics: tumor size, relative vessel density, entropy, and anisotropy. Tumor dimensions measured by SBH-PACT (Fig. 4.6a) were in good agreement with those obtained from clinical imaging (mammography, ultrasound, MRI) and with the histopathological measurements of the surgical specimens (see Table S2 in the original paper). The smallest lesion visualized as a solid mass in SBH-PACT was 0.8 cm × 0.6 cm × 0.5 cm in Patient 3 at T2. Across all three patients, serial SBH-PACT imaging revealed a reduction in tumor volume during NAC.

Within the tumor ROI, we observed decreasing trends in relative vessel density (Fig. 4.6b), entropy (Fig. 4.6c), and anisotropy (Fig. 4.6d) over the course of treatment, whereas the same metrics in the contralateral breast remained relatively stable.

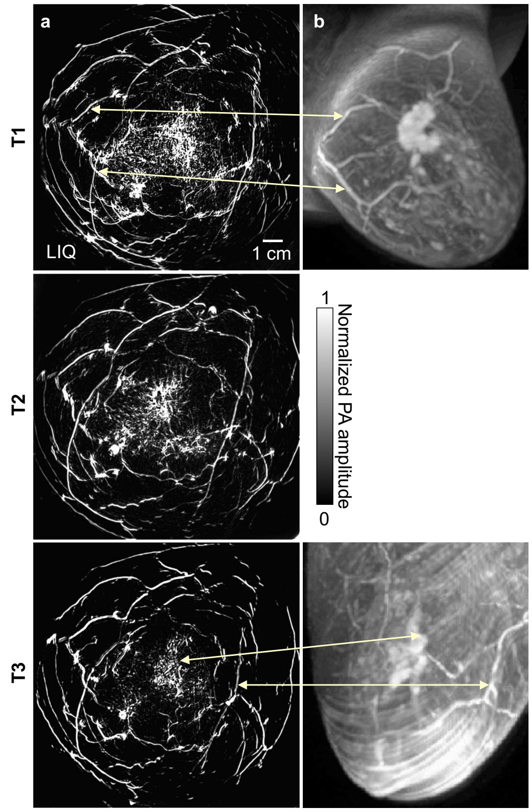

Figure 4.5: **Comparison between SBH-PACT and contrast-enhanced MRI for one patient.** (a) SBH-PACT angiograms modulated by anisotropy-weighted entropy to highlight tumor-associated vasculature. (b) Dynamic contrast-enhanced MRI images at T1 and T3, rotated to match the SBH-PACT viewing geometry. Magenta arrows indicate corresponding structures identifiable in both modalities. SBH-PACT provides fine angiographic details in a single breath-hold acquisition.

Statistical comparisons were performed using one-tailed Welch's t-tests (unequal variances), under the null hypothesis that the mean parameter values in the ROI were not greater than those in healthy tissue. For Patient 3 at T1, vascular metrics in the ROI were significantly elevated relative to healthy tissue ($p < 0.01$), but by T3 the differences were no longer significant ($p > 0.1$), consistent with a complete or near-complete response. For Patients 1 and 2, significant differences ($p < 0.05$) persisted through T3, in line with their partial responses.

We additionally examined average photoacoustic amplitudes within the ROI and in depth-matched healthy tissue. The ratio of ROI to healthy-tissue amplitudes decreased with treatment, reflecting an overall reduction in absorption. However, amplitude-based metrics alone are sensitive to visit-to-visit changes in breast deformation, which alter the local light fluence. Therefore, structural and statistical

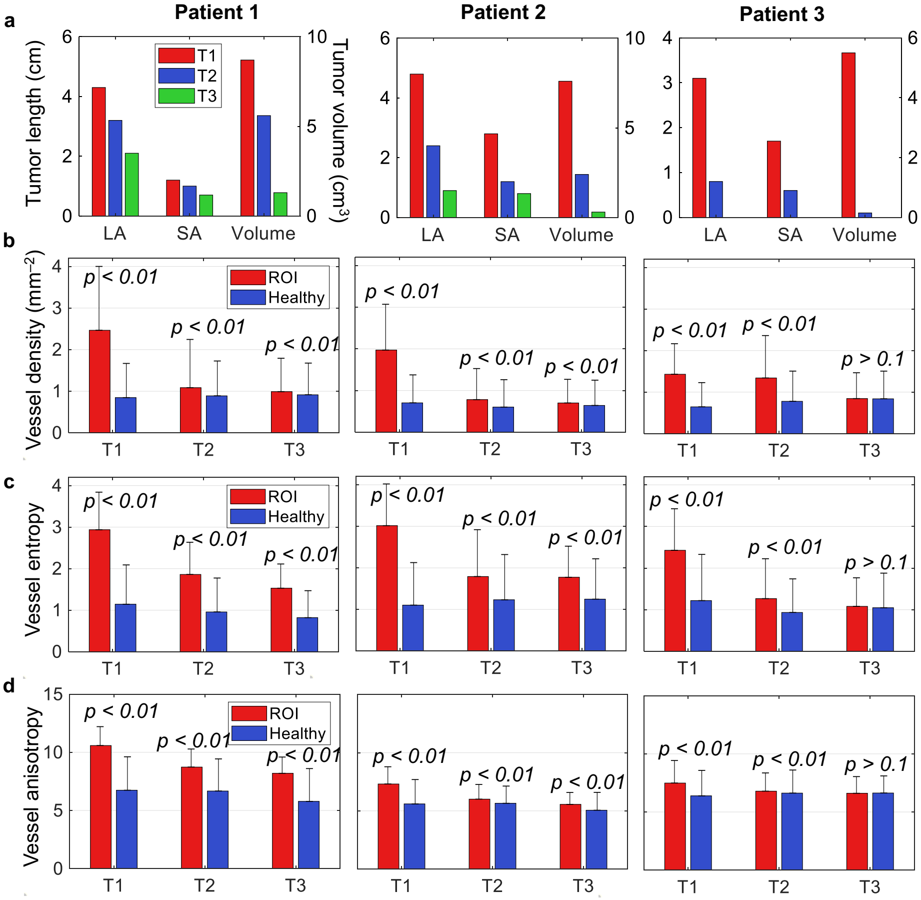

Figure 4.6: **Quantitative characterization of tumor evolution during NAC for three patients.** Data are presented as mean ± standard error; p-values correspond to one-tailed Welch's t-tests. (a) Tumor dimensions and volume (LA, long axis; SA, short axis). (b) Relative vessel density in the ROI and in depth-matched healthy tissue. (c) Vascular entropy in the ROI and healthy tissue. (d) Vascular anisotropy in the ROI and healthy tissue.

descriptors of the vasculature (density, entropy, anisotropy) provide more robust indicators of NAC response.

4.7 Discussion

The results in this chapter highlight SBH-PACT as a promising imaging modality for assessing breast cancer response to chemotherapy. By imaging the entire breast from nipple to chest wall with high spatial resolution, SBH-PACT localizes tumors via regions of increased vascular density and reveals detailed angiographic patterns associated with treatment response. Image processing based on entropy and anisotropy further amplifies differences between normal and tumor vasculature, enabling automated segmentation and quantitative analysis of tumor size, vessel density, entropy, and anisotropy over time.

In this pilot study, we performed SBH-PACT on both affected and contralateral breasts at three time points in three patients, for a total of nine imaging sessions. Despite the limited cohort and early closure of the study due to the coronavirus pandemic, the collected data demonstrate that SBH-PACT can sensitively detect treatment-induced angiographic changes in breast cancer.

Patient feedback was favorable: participants rated SBH-PACT as more comfortable and easier than MRI and mammography and comparable to ultrasound in terms of tolerability. Each breast can be scanned within a single 15 s breath hold, and the method requires neither intravenous contrast nor ionizing radiation, features that are advantageous for serial monitoring and eventual clinical translation.

There are multiple avenues for improving the current system. A laser with higher pulse energy and repetition rate could enhance the CNR and reveal finer vascular features. To optimize light penetration and reduce breast thickness, we currently use a soft agar pillow for gentle compression, which does not fully control breast geometry and may introduce variability across visits. In future implementations, thin polymethylpentene (TPX) holding cups with acoustic impedance closely matched to soft tissu [120] could be used to provide more standardized and reproducible breast positioning. On the image-processing side, sensitivity to microscopic disease might be further improved with multiscale vessel enhancement filter [121], [122] or deep learning-based reconstruction and enhancement methods tailored to photoacoustic angiography [123].

The ability of SBH-PACT to noninvasively visualize and quantify tumor-associated angiogenesis opens up new possibilities in breast cancer imaging. Angiogenesis is intimately linked to tumor development, invasion, and metastatic spread [55], [111], [112], [124], [125]. Historically, limited sensitivity to microvascular changes has prevented widespread clinical use of angiogenesis measurements. Our results suggest that SBH-PACT-based vascular metrics can serve as practical indicators of treatment response. The combination of whole-breast coverage, high spatial resolution, short acquisition time, and the absence of ionizing radiation or contrast injections supports future applications in screening, surveillance, and longitudinal response assessment.

Beyond monitoring NAC, SBH-PACT-derived angiographic biomarkers may be useful as prognostic indicators of relapse-free survival [124], as endpoints for evaluating new systemic therapies [125], and as noninvasive complements or alternatives to biopsy in selected scenarios. Larger prospective studies will be required to validate these applications, establish robust quantitative thresholds, and integrate SBH-PACT into clinical decision-making pathways.

Chapter 5

PACT WITH LEARNING-BASED CLASSIFICATION ENHANCES BREAST LESION CHARACTERIZATION

[1] X. **Tong**†, C. Z. Liu†, Y. Luo†, L. Lin†, J. Dzubnar, M. Invernizzi, S. Delos Santos, Y. Zhang, R. Cao, P. Hu, J. Zheng, J. Torres, A. Kasabyan, L. L. Lai, L. D. Yee, and L. V. Wang, "Panoramic photoacoustic computed tomography with learning-based classification enhances breast lesion characterization," *Nature Biomedical Engineering*, 2025. DOI: `10.1038/s41551-025-01435-3`,

5.1 Introduction

Breast cancer affects roughly 12–13% of women in the United States over their lifetime [126], and benign breast conditions are even more common [127]. Despite improvements in screening, breast cancer still accounts for a major share of cancer-related mortality [128]. Accurate classification of imaging findings is essential for guiding clinical decisions [128]. The breast imaging reporting and data system (BI-RADS) [129] formalizes imaging descriptors and recommended follow-up: lesions that cannot be confidently dismissed as benign frequently lead either to short-interval follow-up or biopsy. Although biopsy is clinically definitive, it is invasive and contributes to patient anxiety, cost and delay [130].

Mammography remains the most widely used screening tool but is hindered by reduced sensitivity in dense breast tissue [131]–[134]. Adjunct modalities address some shortcomings but introduce others. Ultrasound provides structural and functional cues [135] yet is susceptible to operator dependence and diagnostic ambiguity [136]–[138]. Advanced US technologies, such as microvascular imaging and elastography [72], [139], show promise but require additional validation. MRI supports high-risk screening without ionizing radiation but relies on contrast agents [140] and is less suitable for patients with claustrophobia or MR-incompatible implants [141], [142]. Diffuse optical tomography offers sensitivity to haemoglobin dynamics but suffers from low spatial resolution [143].

PACT has emerged as a complementary imaging method that combines optical contrast with ultrasound-based resolution [1], [3]. For breast applications, panoramic PACT achieves volumetric visualization with high spatial resolution and penetration depths of several centimetres [10], [17], [144]–[146]. Hemoglobin absorption enables direct visualization of angiogenesis [55], [147], [148] and hypoxia [149], [150], both fundamental processes in tumour development [151]. Because PACT depends on absorption rather than scattering, images are free of speckle and provide enhanced vessel contrast [152]. Previous PACT studies have shown qualitative lesion appearance [153]–[156] and quantitative vascular features [157]–[161]. More recently, deep-learning-based methods have been introduced for image enhancement and diagnosis [162]–[164]. However, substantial gaps remain: panoramic systems with full-ring coverage are rare; a unified feature set for breast PACT has not been standardized; and quantitative classification and segmentation frameworks have been limited [165].

To address these gaps, we conducted a two-year clinical study of women undergoing diagnostic workup for suspicious mammographic findings. We describe a full workflow—from image acquisition and feature extraction to machine-learning classification and lesion segmentation—designed to evaluate PACT's utility in several clinically relevant tasks. The system captures whole-breast volumes in a single breath-hold, enabling both cross-sectional and longitudinal evaluation. Using features derived from 2D MAPs, we trained classifiers to differentiate healthy quadrants (HQs) and suspicious quadrants (SQs), achieving area under the ROC curve (AUROC) values comparable to those of established clinical modalities [166], [167]. We further evaluated whether PACT-derived features can separate biopsy-confirmed benign lesions from malignant ones, and we developed a semi-automatic segmentation framework to identify lesion centroids and boundaries. Altogether, these developments demonstrate the potential of panoramic PACT to improve breast lesion characterization.

5.2 Patient recruitment and imaging procedure

Participants were drawn from two coordinated clinical studies. The overall workflow—from recruitment to feature extraction and classification—is depicted in Fig. 5.1. Women presenting with abnormal mammographic or MRI findings (BI-RADS 3 or above) were invited to participate, and 39 patients ultimately enrolled. Table 1 summarizes demographics and clinical details.

Following informed consent, each participant underwent PACT imaging (Fig. 5.1b). Two wavelengths, 1,064 nm and 755 nm, were delivered through a diffused illumination scheme. Subjects lay prone on a custom bed with the breast positioned through an aperture and supported by a disposable membrane. A full-ring transducer array beneath the bed performed z-axis scanning. A complete volumetric scan required 13 s during a single breath-hold. Both breasts were imaged in multiple orientations, and a subset of participants returned for follow-up imaging at 6, 12, and 24 months.

Up to two volumetric scans were acquired per visit per wavelength (Fig. 5.1c). Reconstructed 3D volumes were rendered as 2D MAP images and divided into four quadrants for analysis. The panoramic view captures vasculature with resolution down to ~258 µm and depths approaching 4 cm [144]. Phantom studies confirm performance at comparable depths. From each quadrant, 45 features spanning basic statistics, morphological metrics, and dynamic measures were extracted (Figs. 5.1d and e).

Binary classification models were trained to separate HQs from SQs (Figs. 5.1f and g). To limit overfitting, we selected 13 features based on Gini importance and used them to further classify biopsy-confirmed benign and malignant quadrants. Finally, a semi-automatic segmentation workflow localized lesion centroids and boundaries (Fig. 5.1h).

5.3 Comparison with clinical imaging modalities

PACT images allow qualitative inspection of vascular architecture alongside complementary imaging modalities (Fig. 5.2). In a participant with invasive ductal carcinoma (IDC), the primary tumour and a satellite lesion are visible in mammography, MRI and PACT. While mammography cannot depict vasculature, PACT and Gd-MRI show correlated vessel patterns, though PACT reveals finer vascular structures due to its sensitivity to haemoglobin contrast. Feature-encoded PACT images increase lesion conspicuity through automatically weighted feature fusion.

In a second patient with extremely dense breast tissue, the IDC is obscured on mammography but clearly delineated in both PACT and MRI (Fig. 5.2b). Tortuous vessels, known to correlate with malignancy [168], are evident primarily in the PACT images.

5.4 Qualitative lesion analysis and longitudinal monitoring

PACT's panoramic coverage facilitates visual assessment of lesion morphology across a wide spectrum of cases. Patients with stromal fibrosis exhibit vessel distortion without marked feeding vasculature (Figs. 5.3a and b). In contrast, IDCs

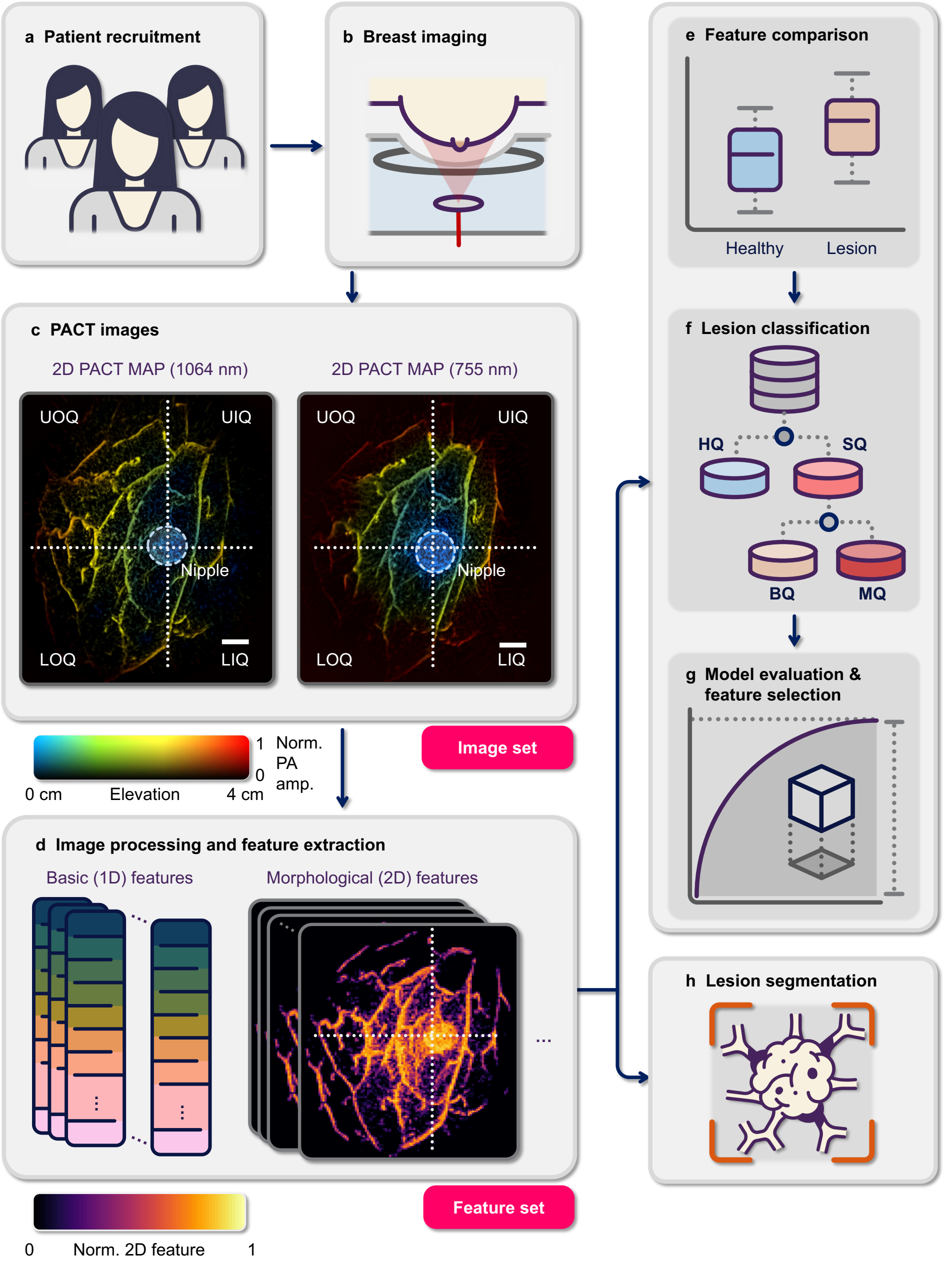

Figure 5.1: **Patient breast PACT workflow.** (a) Participant recruitment. (b) Participant imaging. (c) PACT images of the patient. (d) Image processing and feature extraction. (e) Feature comparison. (f) Lesion classification. SQ, suspicious quadrant. HQ, healthy quadrant. MQ, malignant quadrant. BQ, benign quadrant. (g) Classifier evaluation and feature selection. (h) Lesion localization and segmentation.

show larger areas of high PA amplitude and a dense network of feeding vessels (Figs. 5.3c and d).

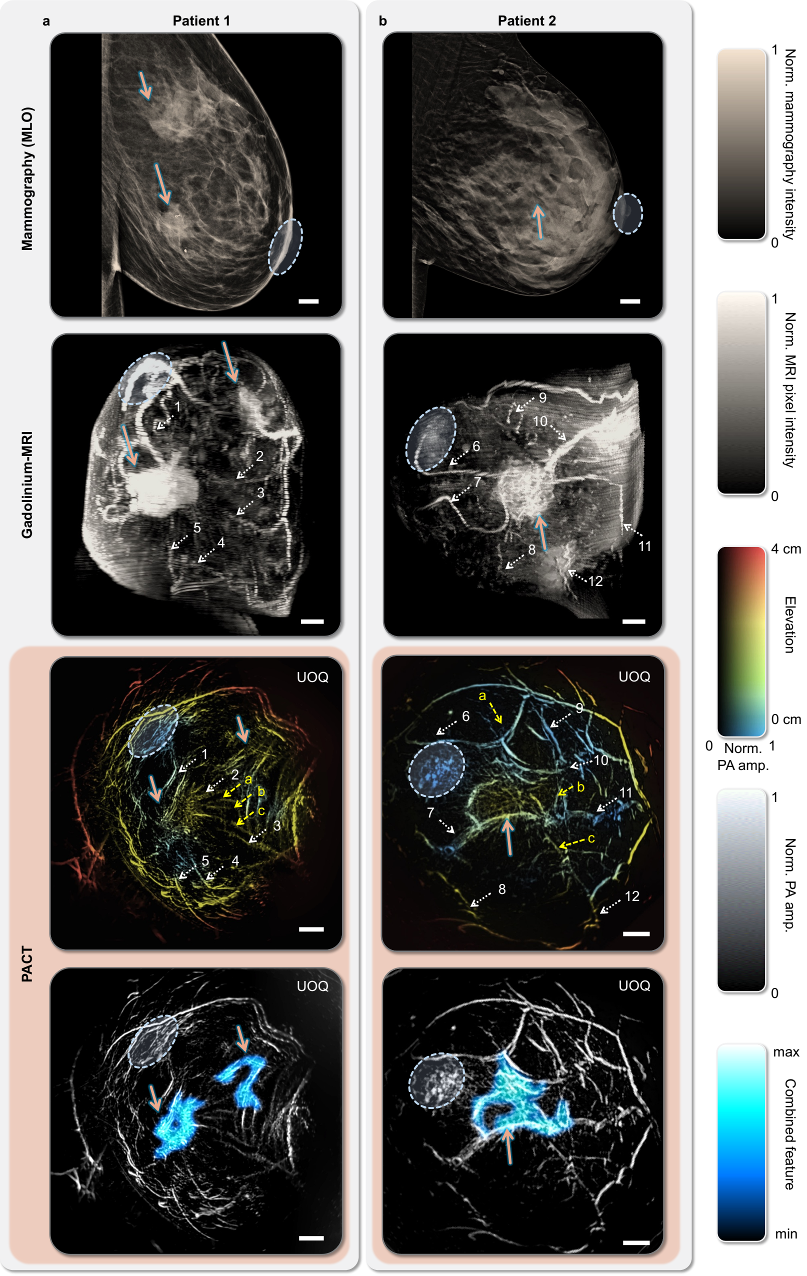

Figure 5.2: **Representative breast images from PACT and conventional imaging modalities.** (a–b) Mammography (top), gadolinium-enhanced MRI (2nd row), depth-encoded PACT (3rd row), and feature-encoded PACT (4th row) images of the same breasts in two patients with invasive ductal carcinoma (IDC). MLO, mediolateral oblique view. UOQ, upper outer quadrants. Lesions are marked by pink solid arrows. Vessels detected by both PACT and MRI are marked by white dotted arrows with numbers. Vessels detected by PACT only are marked by yellow dashed arrows with letters. Nipples are marked by light blue dashed contours. Scale bars, 1 cm.

Longitudinal scans underscore PACT's value for monitoring. Among the 26 participants with benign or probably benign lesions followed over one to two years, PACT images typically show stable vessel density and anisotropy-modulated entropy (AME) (Figs. 5.3e and f). By contrast, a patient whose BI-RADS category progressed over six months exhibited increased vessel density and AME before biopsy-confirmed ductal carcinoma *in situ* (DCIS), changes that were detectable in PACT images before MRI reassessment (Figs. 5.3g–i).

5.5 Quantitative comparison of PACT features

To systematically evaluate discriminatory power, quadrant images were grouped into HQs (BI-RADS ≤ 3) and SQs (BI-RADS ≥ 4). Basic features such as standard deviation and IQR capture global heterogeneity (Figs. 5.4b–d). Morphological features—including vessel skeleton density and AME—reflect spatial structure (Figs. 5.4e–g). Texture descriptors such as GLCM contrast and energy (Figs. 5.4j and k) and Hu moment invariants (Fig. 5.4h) provide complementary information. Nearly all features show statistically significant separation between HQs and SQs.

5.6 Learning-based classification

We trained multiple classifiers (naive Bayes, random forest, SVM, AdaBoost [169], and eXtreme Gradient Boosting (XGBoost) [170]) using 42 preselected features (Fig. 5.5a). Cross-validation revealed XGBoost as the top performer, with maximal AUROC of 0.89 and mean AUROC of 0.87 (Fig. 5.5b). To improve interpretability and reduce overfitting, we ranked features by Gini importance and retained the top 13. The results are summarized in Table 5.6. Applying PCA to these 13 features yielded scores that distinguished biopsy-confirmed benign from malignant quadrants (Fig. 5.5c). t-distributed stochastic neighbor embedding (t-SNE) visualization [171] further highlights clustering of malignant versus benign lesions in the reduced 2D space (Fig. 5.5d).

5.7 Learning-based lesion localization and segmentation

Because classifiers operate at the quadrant level, we developed a complementary segmentation workflow to locate and delineate lesions in the 2D MAP images (Fig. 5.6a). Using the top 2D features (entropy, density and anisotropy), we constructed an enhanced feature map. Thresholded versions of this map highlight candidate lesion regions (Fig. 5.6b). The enhanced images, combined with Gabor-filtered channels and spatial grids, were clustered using K-means to obtain rough

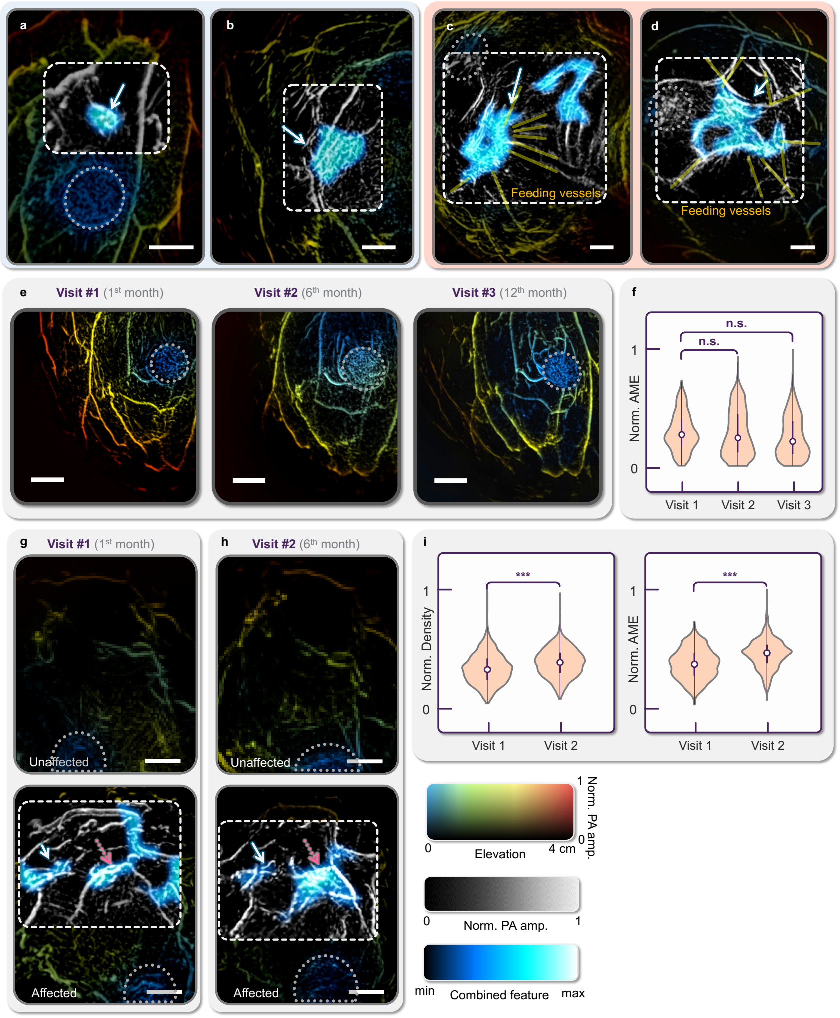

Figure 5.3: **Representative PACT images and longitudinal assessments.** Example PACT images of the regions around two stromal fibrosis lesions (a, b) and two invasive ductal carcinomas (c, d) in each of four study participants. The feeding vessels around the cancers are highlighted by orange lines. (e) Serial images of a BI-RADS 3 lesion from three visits over one year in a participant with benign mass. (f) Feature comparison of the same lesion over three visits. AME, anisotropy-modulated entropy. n.s., $p > 0.05$. (g–i) Sequential imaging of ductal carcinoma *in situ*. (g) First of the serial images of the unaffected (left) and affected (right) breasts of a study participant with a benign mass. (h) Serial images of the same patient after six months. Changes by PACT prior to biopsy are marked by the pink dotted arrows. (i) Feature comparison of the same lesion over two visits. $***p < 0.001$. All other lesions are marked by white arrows. Nipples are marked by gray dotted contours. Scale bars, 1 cm. Identified lesions are indicated by color using the combined feature value.

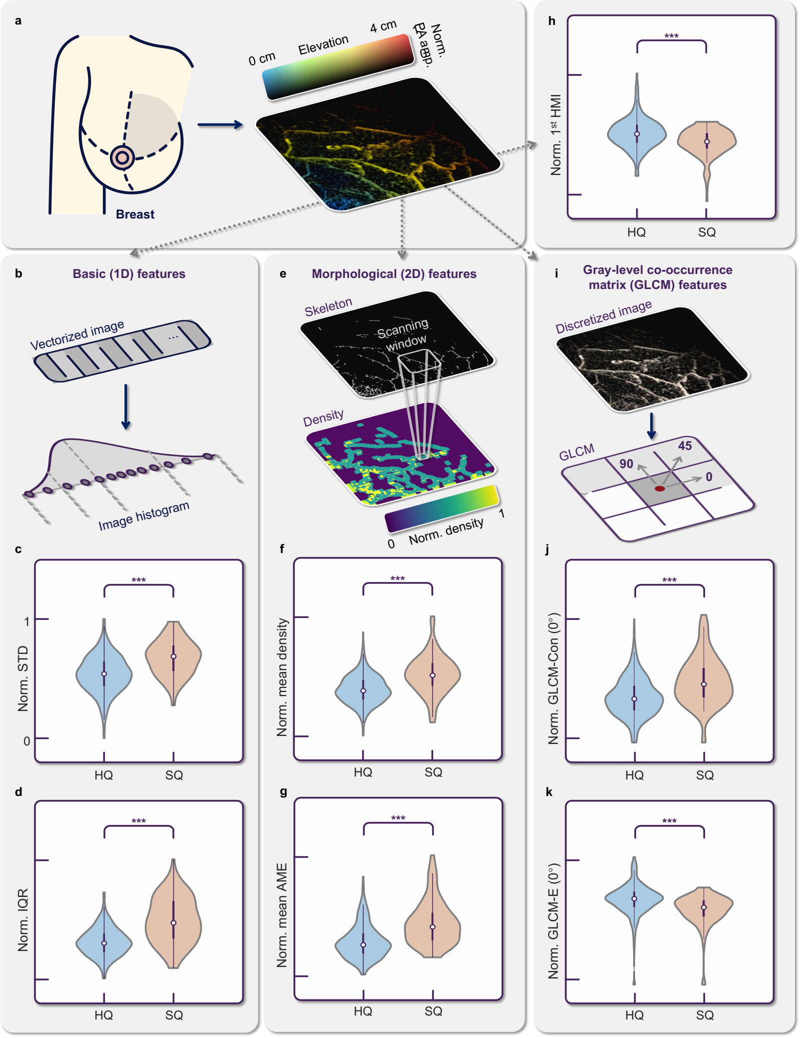

Figure 5.4: **Examples of PACT-derived features for HQ–SQ comparison.** (a) Feature extraction based on quadrants. (b) Extraction of the basic (1D) features. (c–d) Examples of the 1D feature comparison using violin plots, based on (c) standard deviation (STD) and (d) interquartile range (IQR), between healthy quadrants (HQs) and suspicious quadrants (SQs). $***p < 0.001$. (e) Example morphological (2D) feature map of the vessel skeleton, from which the vessel density map was acquired. (f–g) Violin plots of (f) vessel density and (g) anisotropy-modulated entropy (AME). (h) Hu moment invariant (HMI)-based feature comparison. (i) Extraction of gray-level co-occurrence matrix (GLCM)-based features. (j–k) Examples of the GLCM feature comparison using violin plots, based on the (j) contrast and (k) energy at 0° orientation of neighboring pixels, between HQs and SQs. $***p < 0.001$. For all features, $n_{\mathrm{HQ}} = 534$, $n_{\mathrm{SQ}} = 141$.

masks, followed by morphological refinement and manual bounding box adjustments by three trained readers. We then used MedSAM [172], a medical adaptation

Classifier	**Features**	**Training AUROC**	**Testing AUROC**	**Testing F_1 score**
NB	42 features	0.86 ± 0.06	0.71 ± 0.01	0.54 ± 0.01
	13 features	0.88 ± 0.01	0.82 ± 0.01	0.71 ± 0.01
RF	42 features	0.98 ± 0.02	0.81 ± 0.01	0.55 ± 0.05
	13 features	0.99 ± 0.01	0.82 ± 0.02	0.69 ± 0.03
SVM	42 features	0.86 ± 0.03	0.57 ± 0.05	0.38 ± 0.07
	13 features	0.88 ± 0.03	0.78 ± 0.01	0.62 ± 0.03
AdaBoost	42 features	0.95 ± 0.02	0.83 ± 0.02	0.66 ± 0.02
	13 features	0.95 ± 0.02	0.82 ± 0.04	0.70 ± 0.02
XGBoost	42 features	0.94 ± 0.02	0.83 ± 0.02	0.71 ± 0.03
	13 features	0.96 ± 0.01	0.87 ± 0.01	0.74 ± 0.02

Table 5.1: Performance comparison of classifiers using 42-feature and 13-feature subsets.

of the Segment Anything model (SAM), to infer refined lesion masks. The lesion long-axis length estimated from PACT correlates well with measurements from mammography, US, and MRI ($r^2 = 0.77$, Fig. 5.6c).

5.8 Discussion

This chapter presents a comprehensive panoramic PACT workflow for breast lesion evaluation, integrating image acquisition, feature extraction, classification and segmentation. The system's high spatial resolution and depth capability allow detailed visualization of vasculature, a key indicator of lesion physiology. Compared with earlier PACT studies, this work incorporates a more extensive patient cohort, richer feature analysis and machine-learning-based interpretation.

Qualitative imaging shows that malignant lesions tend to exhibit increased vessel density, irregular feeding vessels and enhanced PA amplitude, consistent with known angiogenic processes [173]. Quantitatively, features spanning intensity statistics, morphology, texture and dynamics collectively discriminate HQs from SQs, and the learned models generalize to lesions imaged across two independent PACT platforms. In classification tasks, PACT achieves AUROC values comparable to or exceeding mammography and ultrasound across breast densities [132], [133], [167], [174]–[178]. Furthermore, PACT-derived features show potential to distinguish benign from malignant lesions—an important step toward reducing unnecessary biopsies.

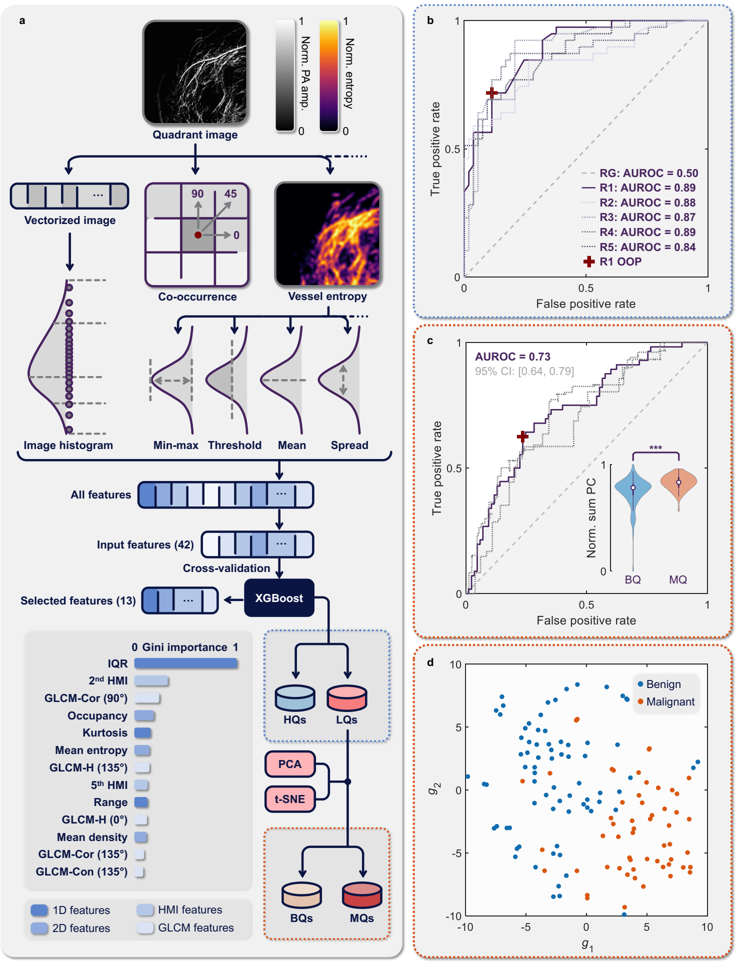

Figure 5.5: **Classifier development and performance.** (a) Schematic of the feature extraction, feature selection, and classification. IQR, interquartile range. HMI, Hu moment invariant. GLCM, gray-level co-occurrence matrix. Cor, correlation. Con, contrast. H, homogeneity. (b) ROC curves of the XGBoost classifier. Solid line corresponds to the ROC curve with the highest AUROC. Dotted lines correspond to the other ROC curves from the 5-round cross-validation (R1–R5). Dashed line corresponds to the baseline ROC curve from random guess (RG). Cross denotes the optimal operating point (OOP) of the optimal ROC curve. For the testing set, $n_{\text{HQ}} = 53$, $n_{\text{SQ}} = 39$. (c) ROC curves based on the sum of the first six principal components (PCs) of biopsy-proven benign (BQ) and malignant (MQ) quadrants through PCA. Dotted lines correspond to the lower and upper bounds of the 95% CI. Norm., normalized. (d) t-SNE visualization of the clustering of the 13-dimensional features from the BQs and MQs in the two-dimensional subspace. For (c) and (d), $n_{\text{BQ}} = 85$, $n_{\text{MQ}} = 56$.

Technical extensions, including dual-wavelength imaging and PA elastography, offer promising directions for increasing diagnostic richness. Differences in wavelength-

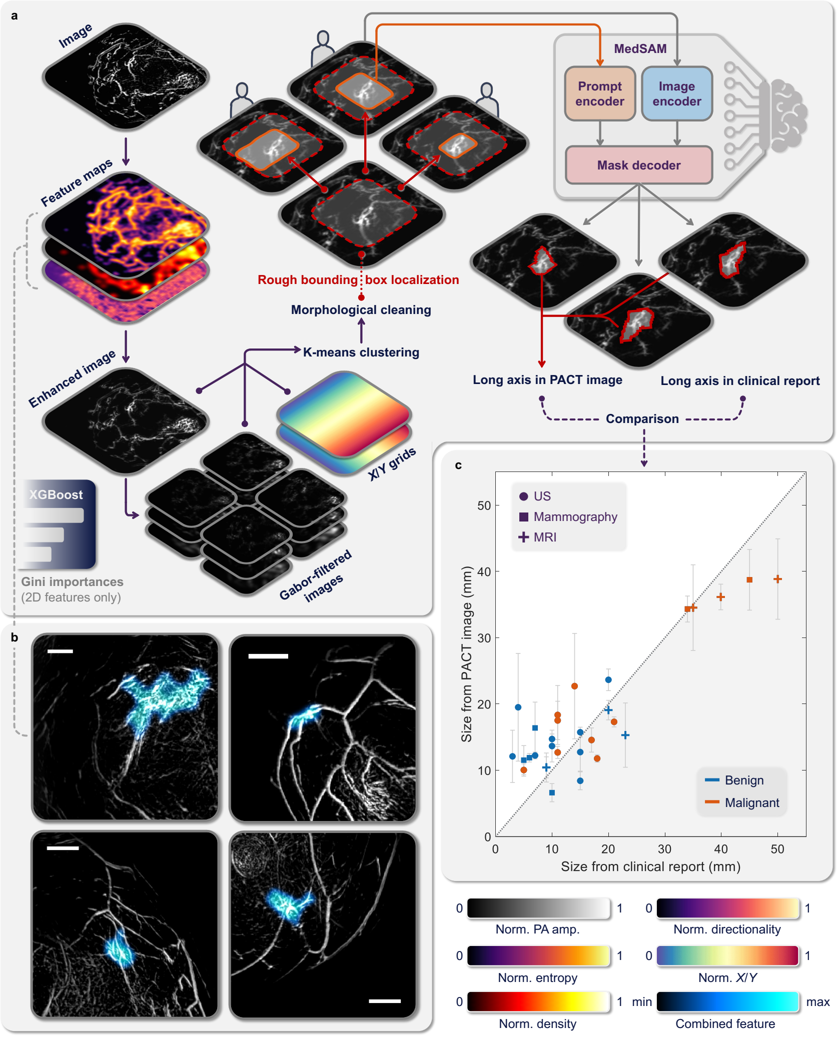

Figure 5.6: **Semi-automatic lesion localization and segmentation.** (a) Schematic of the lesion segmentation. (b) Examples of four breast quadrant images color-encoded by the weighted product of vessel density (V), entropy (H), and anisotropy (A). Color bars, 1 cm. (c) Distribution of the lesion size (in terms of the long axis) estimated through PACT versus from the clinical report. US, ultrasonography. Data are plotted as means ± standard errors of the mean ($n = 3$).

dependent penetration and melanin absorption suggest avenues for personalized imaging protocols [80], [179]. Elastic contrast extracted from breathing motion frames [144], [180], [181] may further improve lesion characterization.

Limitations include the relatively modest cohort size and reliance on MAP images rather than full volumetric features. Larger datasets will allow exploration of deep-learning models for multimodal integration [182], [183]. Our results from a fully automated segmentation pipeline underscore the importance of fine-tuning when sample sizes are small.

Overall, panoramic PACT offers a powerful and non-ionizing approach for breast imaging. With further refinement and standardization, PACT could become a valuable adjunct to conventional modalities, supporting early detection, improved lesion characterization and more informed clinical decision-making.

Chapter 6

INTRODUCTION TO QUANTUM IMAGING

[1] X. **Tong**†, Z. He†, Y. Zhang†, S. Solomon, L. Lin, Q. Song, and L. V. Wang, “Experimental full-domain mapping of quantum correlation in clauser-horne-shimony-holt scenarios,” *Physical Review Applied*, 2023. DOI: `10.1103/physrevapplied.19.034049`,

[2] X. **Tong**, Y. Zhang, and L. V. Wang, “Enhancing optical microscopy with quantum entanglement,” *Optics and Photonics News*, 2024. DOI: `10.1364/opn.35.11.000032`,

Classical optical microscopy forms images by mapping the intensity of light transmitted, reflected, or scattered by an object onto a detector. The achievable performance is governed by standard figures of merit: spatial resolution, contrast, and noise. Spatial resolution is limited by the optical wavelength and numerical aperture through diffraction; contrast depends on how strongly the object modulates the illumination relative to its background; and the CNR is ultimately constrained by photon shot noise and detector noise [184], [185].

Quantum imaging (QI) extends this framework by exploiting nonclassical states of light—most prominently entangled and squeezed states—and measuring multiphoton correlations rather than single-photon intensitie [186]–[188]. This shift enables qualitatively new imaging modalities and quantitative performance gains that cannot be achieved with classical light alone.

This chapter focuses on the principles and applications of QI. Section 6.1 summarizes the principles of QI. Section 6.2 introduces the characterization of the degrees of entanglement of the photon sources in general and focuses on my work in quantizing the polarization entanglement using the full-domain coincidence maps. Section 6.3 discusses the advantages and limitations of QI.

6.1 Principles of quantum imaging

Entangled photons and SPDC

In most optical QI experiments, entangled photon pairs are generated via spontaneous parametric down-conversion (SPDC) in a second-order ($\chi^{(2)}$) nonlinear crystal [189]. A pump photon at angular frequency ω_p is converted, with low probability, into a pair of lower-energy photons at frequencies ω_s and ω_i (signal and idler), constrained by energy and momentum conservation,

$$\omega_p = \omega_s + \omega_i, \qquad \mathbf{k}_p = \mathbf{k}_s + \mathbf{k}_i. \tag{6.1}$$

The phase-matching configuration determines whether the signal and idler share the same polarization (type-0 or type-I SPDC) or have orthogonal polarizations (type-II SPDC), and whether they emerge collinearly or on separate emission cones.

By combining two type-I (or type-0) crystals with orthogonal optical axes, or by exploiting the intersection region of type-II emission, one can engineer high-brightness sources of polarization-entangled biphotons. A typical output state has the form

$$|\psi_{\mathrm{SPDC}}\rangle = \cos\theta_p \, |H\rangle_s \, |H\rangle_i + e^{i\phi_d} \sin\theta_p \, |V\rangle_s \, |V\rangle_i \,, \tag{6.2}$$

where θ_p and ϕ_d encode the pump polarization and the relative phase accumulated in the crystal pair and compensating optics [190]. For $\theta_p = \pi/4$ and $\phi_d = 0$ (up to global phase), Eq. (6.2) reduces to a maximally entangled Bell (EPR) state,

$$|\psi_{\mathrm{EPR}}\rangle = \frac{1}{\sqrt{2}} \left(|H\rangle_s \, |H\rangle_i + |V\rangle_s \, |V\rangle_i \right). \tag{6.3}$$

Beyond polarization, SPDC inherently produces strong correlations in the transverse spatial degrees of freedom and in the joint energy–time domain. These arise from the same energy- and momentum-conservation relations that govern the biphoton generation process, but manifest in continuous-variable wavefunctions rather than discrete polarization states. These degrees of entanglement underpin many QI protocols such as ghost imaging, quantum holography, and super-resolution coincidence microscopy [191]–[193].

In the paraxial regime, the biphoton state may be written in transverse momentum coordinates $\mathbf{q}_s$ and $\mathbf{q}_i$ as

$$|\psi_{\mathrm{spatial}}\rangle = \iint \mathrm{d}\mathbf{q}_s \, \mathrm{d}\mathbf{q}_i \; \Phi(\mathbf{q}_s, \mathbf{q}_i) \, |\mathbf{q}_s\rangle_s \, |\mathbf{q}_i\rangle_i \,, \tag{6.4}$$

where the biphoton amplitude Φ is approximately

$$\Phi(\mathbf{q}_s, \mathbf{q}_i) \propto \tilde{E}_p(\mathbf{q}_s + \mathbf{q}_i) \, \mathrm{sinc}\!\left(\frac{L}{2} \, \Delta k_z(\mathbf{q}_s, \mathbf{q}_i) \right). \tag{6.5}$$

Here $\tilde{E}_p$ is the transverse spatial spectrum of the pump, L is the crystal length, and Δk_z is the longitudinal phase mismatch. The pump term enforces a strong momentum anticorrelation $\mathbf{q}_s + \mathbf{q}_i \approx 0$, while the phase-matching term couples their bandwidths. By Fourier transforming Eq. (6.4), one obtains the position-space wavefunction,

$$\psi(\mathbf{r}_s, \mathbf{r}_i) \propto E_p\left(\frac{\mathbf{r}_s + \mathbf{r}_i}{2}\right) \Phi(\mathbf{r}_s - \mathbf{r}_i), \tag{6.6}$$

which displays strong position correlations $\mathbf{r}_s \approx \mathbf{r}_i$ for thin-crystal or wide-pump conditions. $\Phi(\mathbf{r}_s - \mathbf{r}_i)$ is the position-correlation function determined by the crystal phase-matching and finite longitudinal interaction length. These spatially entangled biphotons form the basis of quantum ghost imaging, quantum holography, and super-resolution coincidence microscopy, where the nonlocal correlations allow information about an object in one arm to be reconstructed using detections in another arm.

Energy conservation in SPDC yields a complementary continuous-variable entanglement in frequency and arrival time. The joint spectral amplitude of the biphoton can be written as

$$|\psi_\omega\rangle = \iint \mathrm{d}\omega_s \, \mathrm{d}\omega_i \; f(\omega_s, \omega_i) \; |\omega_s\rangle_s \, |\omega_i\rangle_i \,, \tag{6.7}$$

with

$$f(\omega_s, \omega_i) \propto \alpha(\omega_s + \omega_i) \, \phi(\omega_s, \omega_i), \tag{6.8}$$

where α is the pump spectral envelope and ϕ is the crystal phase-matching function. The narrow pump bandwidth imposes strong anticorrelations in frequency: $\omega_s+\omega_i \approx \omega_p$. Fourier transforming the joint spectral amplitude gives the joint temporal amplitude,

$$\psi(t_s, t_i) = \frac{1}{2\pi} \iint \mathrm{d}\omega_s \, \mathrm{d}\omega_i \; f(\omega_s, \omega_i) \, e^{-i(\omega_s t_s + \omega_i t_i)}, \tag{6.9}$$

which exhibits tight coincidence-time correlations $t_s \approx t_i$ for broadband phase matching. These correlations underpin applications such as dispersion cancellation, Franson interferometry, and various time-resolved quantum imaging protocols that exploit the ultrashort biphoton coherence time to outperform classical timing limits.

Together, the spatial and time–energy wavefunctions provide a high-dimensional resource that complements the discrete polarization entanglement described earlier, enabling a broad suite of quantum-imaging modalities that leverage continuous-variable correlations inaccessible to classical light.

Single-photon detectors and coincidence detection

A wide range of single-photon detectors and imaging sensors are used in QI experiments, each offering distinct trade-offs in quantum efficiency, timing resolution, dark count rate, and spatial multiplexing capabilities. These characteristics determine not only the achievable signal-to-noise ratio but also the appropriate strategy for coincidence extraction.

Single-photon avalanche diodes (SPADs)

SPADs (or single-photon counting modules or SPCMs)—either stand-alone modules or integrated into multi-pixel arrays—operate in Geiger mode and provide digital pulses upon single-photon absorption. They feature sub-nanosecond timing jitter and can be paired with time-to-digital converters (TDCs) for high-precision timestamping. Because SPADs produce discrete electronic pulses, coincidences between signal and idler channels are typically identified using hardware or software temporal windows,

$$|t_s - t_i| < \Delta t, \tag{6.10}$$

where Δt is chosen based on detector jitter and optical-path mismatch. Many tabletop QI experiments—including Franson interferometry, quantum key distribution testbeds, and proof-of-principle ghost imaging—use such SPAD–TDC architectures due to their excellent timing resolution and low dead time.

Electron-multiplying CCDs (EMCCDs)

EMCCDs provide high quantum efficiency (especially in the visible spectrum) and sub-electron effective read noise thanks to their on-chip electron-multiplication register. Unlike SPADs, they do not yield per-photon timing information. Instead, exposures integrate many photon events into a 2D intensity map $I(\mathbf{r})$ for each frame. Coincidence information is extracted statistically by computing covariance across frames,

$$C(\mathbf{r}_s, \mathbf{r}_i) = \big\langle I_s(\mathbf{r}_s)\, I_i(\mathbf{r}_i) \big\rangle - \big\langle I_s(\mathbf{r}_s) \big\rangle \big\langle I_i(\mathbf{r}_i) \big\rangle. \tag{6.11}$$

This covariance-based detection recovers the same underlying second-order correlation function $G^{(2)}$ without time stamping. EMCCDs and intensified CCDs (ICCDs) have therefore become standard tools in high-dimensional spatial entanglement experiments, quantum ghost imaging, and coincidence microscopy where spatial resolution—not timing—is the limiting factor.

Scientific CMOS (sCMOS) sensors

sCMOS cameras offer higher frame rates and lower noise than CCDs, but their readout architecture introduces pixel-dependent gain, noise, and fixed-pattern artifacts.

Like EMCCDs, they rely on spatial covariance for extracting biphoton correlations. While their higher speed is advantageous for dynamic or scanning QI experiments, their higher effective read noise generally requires brighter SPDC sources or longer integration times. Recent work using sCMOS sensors has demonstrated megapixel-scale $G^{(2)}$ reconstructions and massively parallel coincidence imaging.

Superconducting nanowire single-photon detectors (SNSPDs)

SNSPDs provide near-unity quantum efficiency, picosecond-scale timing jitter, extremely low dark counts, and fast recovery times. They are typically used as single-pixel or few-pixel detectors, though SNSPD arrays (tens to hundreds of pixels) are becoming increasingly available. Their superb temporal resolution enables ultra-narrow coincidence windows and precise measurement of joint spectral or temporal correlations.

Table 6.1: Comparison of common single-photon detectors used in QI experiments.

Detector	**Quantum efficiency**	**Dark count rate**	**Pixel count**
SPAD (single-pixel)	40–70%	10–500 cps	1
SPAD array	20–50%	10^2–10^3 cps/pixel	10–1000
EMCCD	80–95%	negligible	512^2–1024^2
sCMOS	60–80%	negligible	512^2–1024^2
SNSPD (single-pixel)	80–98%	< 1 cps	1

Table 6.1 summarizes the key specifications of the single-photon detectors. Together, these detection technologies and coincidence mechanisms form the experimental backbone of quantum imaging. The choice of sensor and analysis strategy is dictated by whether the imaging task is primarily limited by timing resolution, spatial resolution, or photon budget.

Quantum imaging configurations

Several canonical imaging configurations emerge when SPDC sources and coincidence detection are combined with different optical layouts [188].

- Ghost imaging. Signal photons traverse the object and are collected by a bucket detector without spatial resolution, while idler photons are detected by a spatially resolving camera. By correlating bucket counts with individual

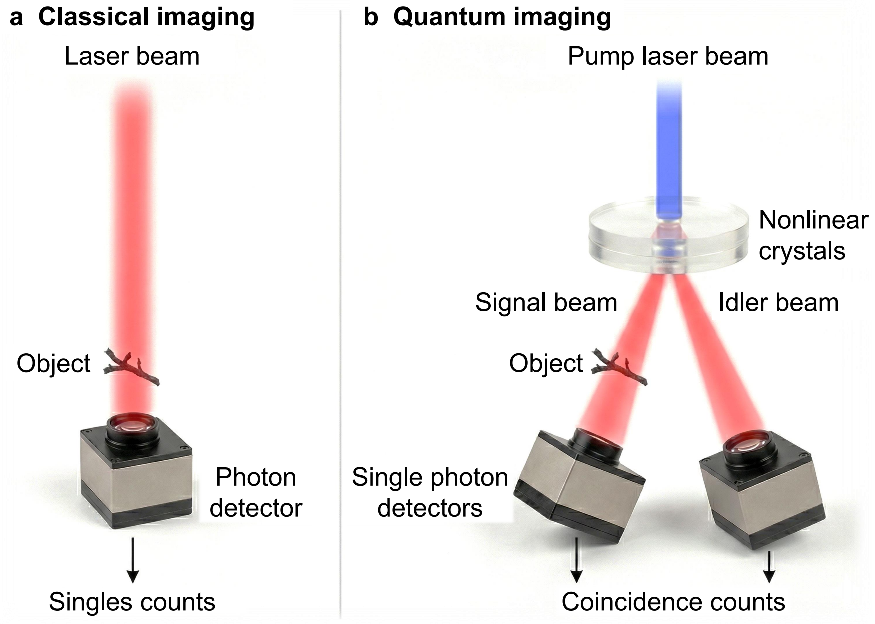

Figure 6.1: **Conceptual comparison of classical and quantum imaging.** (a) In classical imaging, a single detector records the intensity after the object. (b) In quantum imaging, an SPDC source generates entangled signal–idler pairs; the signal interacts with the object while the idler bypasses it, and images are reconstructed from coincidence counts between the two detection channels.

camera pixels, one reconstructs an image of the object even though the imaging optics and spatial resolution reside entirely in the idler arm [192].

- Imaging with undetected photons. In undetected-photon imaging, the object modulates one arm of an interferometric SPDC setup, but only the conjugate arm is actually detected [191]. The interference fringes of the detected idler photons encode amplitude and phase information about the signal photons that interacted with the object, enabling imaging at one wavelength while detecting at another, often more convenient, wavelength.

- Coincidence-based quantum microscopy. By directing the photon pairs through the signal and idler arms separately, coincidence-based quantum imaging can beat the classical diffraction limit by exploiting spatial entanglement and interference. In imaging by coincidence from entanglement (ICE), entangled biphotons effectively implement a virtual confocal pinhole, narrowing the point-spread function and providing $\sim$40% resolution enhancement, along with strong stray-light suppression [194]. Quantum microscopy by coincidence (QMC) achieves near twofold resolution enhancement and improved robustness to stray light [188], [195].

6.2 Characterization of quantum imaging sources

Spatial entanglement characterization

Quantifying the strength and dimensionality of entanglement in SPDC systems is essential for evaluating their suitability for QI tasks such as high-dimensional imaging, super-resolution coincidence microscopy, and nonlocal interferometry. The biphoton state generated by SPDC can be described in either spatial coordinates $(\mathbf{r}_s, \mathbf{r}_i)$ or spectral coordinates (ω_s, ω_i) through a joint amplitude $f(x_s, x_i)$, where x represents a continuous degree of freedom. A common metric of entanglement dimensionality is the *Schmidt number* K, defined from the singular-value decomposition of f.

Experimentally, one typically measures the joint probability distribution

$$P(x_s, x_i) = |f(x_s, x_i)|^2, \tag{6.12}$$

and reconstructs the corresponding Schmidt coefficients via numerical diagonalization of the reduced density operator. For separable states $K = 1$, whereas high-dimensional entanglement yields large K, often 10^2–10^4 in spatial-domain measurements and 10–100 in energy–time measurements, depending on pump bandwidth, crystal geometry, and collection optics.

Spatial entanglement is typically evaluated by measuring the joint position distribution $P(\mathbf{r}_s, \mathbf{r}_i)$ or its Fourier-dual momentum distribution $P(\mathbf{q}_s, \mathbf{q}_i)$. The measured $G^{(2)}$ map reveals the position or momentum correlation widths of the biphoton state, from which the Schmidt number can be estimated using

$$K_{\text{spatial}} \approx \frac{\sigma_{\text{pump}}}{\sigma_{\text{corr}}}, \tag{6.13}$$

where σ_{pump} is the pump-beam width (in either position or momentum space) and σ_{corr} is the measured correlation width of the biphoton distribution. More rigorous methods directly diagonalize the reconstructed joint distribution to obtain the Schmidt eigenmodes, which often approximate spatial Hermite–Gaussian or Laguerre–Gaussian modes depending on the pump shape and crystal geometry. Such measurements have been widely used to assess the transverse-mode structure of SPDC and to benchmark high-dimensional QI systems.

Energy-time entanglement characterization

Energy–time correlations are probed by reconstructing the biphoton joint spectral intensity $P(\omega_s, \omega_i)$ or joint temporal intensity $P(t_s, t_i)$. Joint spectral measurements can be performed using scanning monochromators, dispersive-fiber spectrometers, or time-of-arrival spectrographs combined with high-timing-resolution detectors such as SNSPDs. The joint spectral intensity encodes the anticorrelation ridge $\omega_s + \omega_i \approx \omega_p$, whose tilt and width reflect the interplay between the pump spectrum and crystal phase matching.

Once the joint spectral intensity is measured, the Schmidt number is obtained by singular-value decomposition of $f(\omega_s, \omega_i)$ or, when only intensities are available, by applying a phase-retrieval or moment-based approximation. For transform-limited pump pulses, a simple estimate follows from the ratio of marginal to conditional bandwidths,

$$K_{\text{spectral}} \approx \frac{\Delta\omega_{\text{marg}}}{\Delta\omega_{\text{cond}}}, \tag{6.14}$$

where $\Delta\omega_{\text{marg}}$ is the single-photon bandwidth and $\Delta\omega_{\text{cond}}$ is the narrow conditional bandwidth obtained by fixing the partner photon's frequency.

Polarization entanglement characterization

Polarization entanglement in SPDC sources is typically quantified by reconstructing the two-photon density matrix through quantum state tomography (QST) and evaluating metrics such as state fidelity, concurrence, and the Clauser–Horne–Shimony–Holt (CHSH) Bell parameter, all of which capture the strength and purity of nonclassical correlations between the signal and idler photons (Fig. 6.2). High-quality entanglement appears as strong off-diagonal coherences in the density matrix and Bell-inequality violations exceeding the classical bound.

We developed a robust framework for mapping polarization entanglement using full-domain correlation mapping, enabling quantitative Bell-state analysis directly within an imaging geometry and offering a practical route toward entanglement-enabled quantum imaging systems.

Full-domain coincidence maps

Our experimental setup in Ref. [190] consists of a 405 nm continuous-wave pump laser, polarization and phase-control optics (polarizer, half-wave plate, variable wave plate, quartz plate), and a pair of type-I β-barium borate (BBO) crystals with

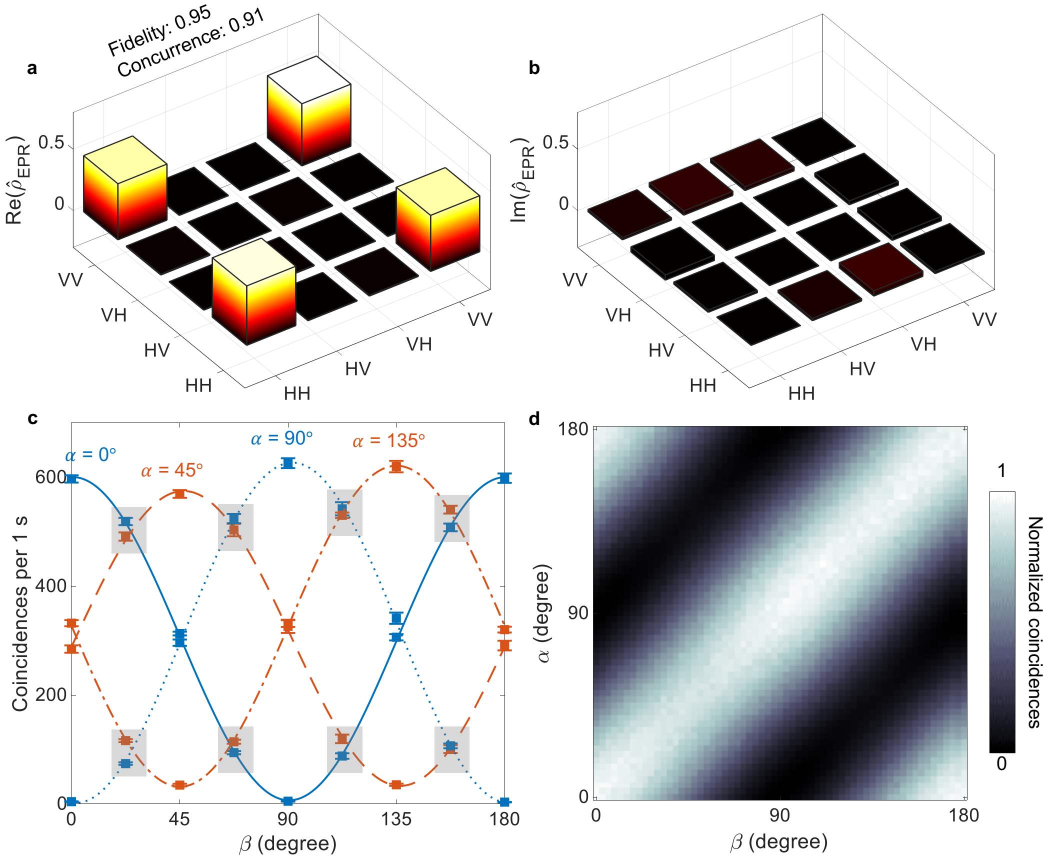

Figure 6.2: **Characterization of an experimental EPR-like state.** (a–b) Real (a) and imaginary (b) parts of the reconstructed two-qubit density matrix from QST; fidelity and concurrence quantify the entanglement. (c) Coincidences as a function of β when $\alpha = 0, 45, 90, 135$. Experimental results are plotted as means ± standard errors of the means ($n = 9$). (d) Full-domain coincidence map $N(H, H|\alpha, \beta)$, showing the sinusoidal modulation of coincidences versus analyzer angles.

orthogonal optical axes (Fig. 6.3). By adjusting the pump polarization angle θ_p and the relative phase ϕ_d (Eq. 6.2), one can prepare a family of bipartite states ranging from nearly product states to highly entangled EPR-like states and Werner-type mixtures.

Signal and idler photons are routed to separate analyzer arms, each comprising a half-wave plate and a polarizing beam splitter followed by bandpass filters, collection optics, and SPCMs. A time-tagging controller records single counts and coincidences with sub-nanosecond resolution [190]. Instead of measuring correlations at a small set of analyzer angles optimized for a particular Bell test, we scan

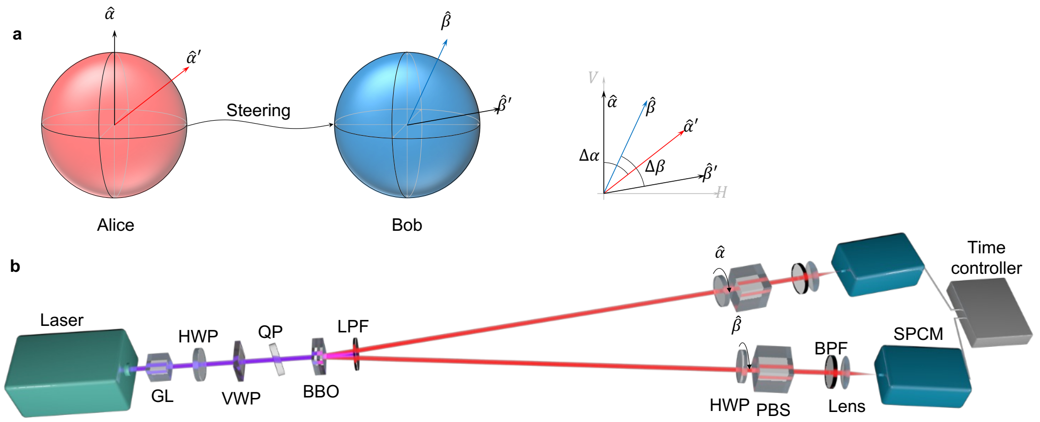

Figure 6.3: **Experimental setup for full-domain correlation mapping of polarization-entangled biphotons.** Pump polarization and phase are controlled before a pair of type-I BBO crystals that generate entangled photon pairs. Motorized half-wave plates and polarizing beam splitters in the signal and idler arms scan analyzer angles (α, β), while SPCMs and a time controller record coincidences.

the full (α, β) domain on a grid, recording the coincidence rate $N(H, H|\alpha, \beta)$ at each point [190]. Shifting this map by 90° along the α and/or β axes yields effective coincidence maps for the other outcome combinations:

$$N(V, H|\alpha, \beta) \simeq N(H, H|\alpha + 90^\circ, \beta), \tag{6.15}$$

$$N(H, V|\alpha, \beta) \simeq N(H, H|\alpha, \beta + 90^\circ), \tag{6.16}$$

$$N(V, V|\alpha, \beta) \simeq N(H, H|\alpha + 90^\circ, \beta + 90^\circ). \tag{6.17}$$

These four maps are then combined via Eq. (6.18) to produce a full-domain correlation map $E(\alpha, \beta)$ that compactly encodes polarization correlations for *all* possible analyzer pairs.

For an experimental EPR-like state, the resulting $N(H, H|\alpha, \beta)$ map exhibits sinusoidal fringes along both axes, and the derived $E(\alpha, \beta)$ map displays alternating lobes of strong positive and negative correlation [190].

Mapping Bell nonlocality and quantum steering

For polarization-based experiments, one often works with binary outcomes corresponding to horizontal (H) or vertical (V) polarizations measured at analyzer angles α and β for signal and idler, respectively. Denoting the joint probabilities by $P(a, b|\alpha, \beta)$ with $a, b \in \{H, V\}$, a convenient correlation observable is [190]

$$E(\alpha, \beta) = P(H, H|\alpha, \beta) + P(V, V|\alpha, \beta) - P(H, V|\alpha, \beta) - P(V, H|\alpha, \beta). \tag{6.18}$$

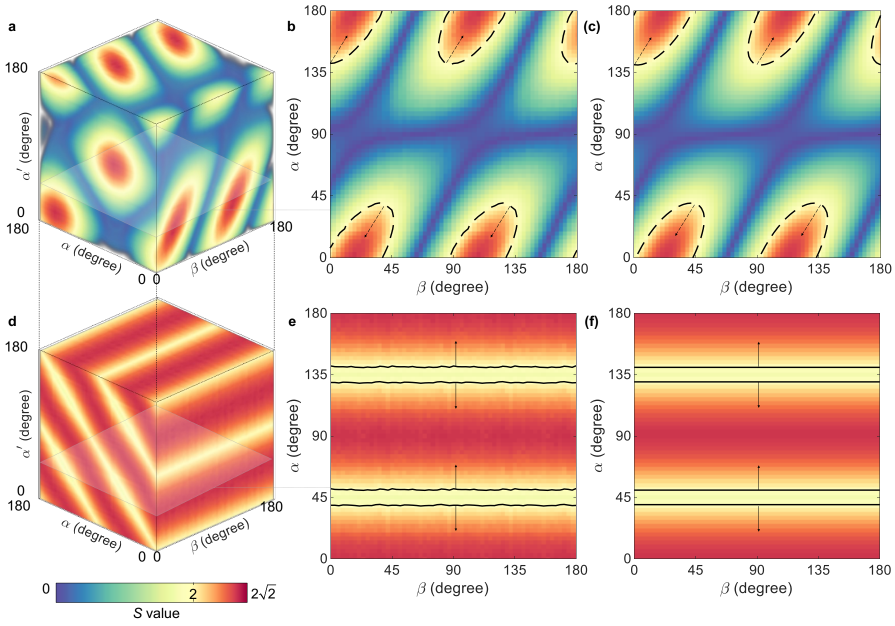

Figure 6.4: **Full-domain characterization of nonlocality and steering for an EPR-like state.** (a–c) Three-dimensional CHSH map $S_{\text{CHSH}}(\alpha, \alpha', \beta, \beta + 45°)$, with lobes where $S_{\text{CHSH}} > 2$ indicating violation of local-hidden-variable models. (d–f) Corresponding steering map S_{QS}, with a larger violation volume reflecting the weaker local-hidden-state bound.

In the CHSH scenario, Alice and Bob (signal and idler arms) choose between two analyzer settings each, (α, α') and (β, β'). The CHSH parameter is then

$$S_{\text{CHSH}} = |E(\alpha, \beta) + E(\alpha', \beta) - E(\alpha, \beta') + E(\alpha', \beta')| . \tag{6.19}$$

Local-hidden-variable models impose the Bell–CHSH inequality $S_{\text{CHSH}} \leq 2$, while quantum mechanics permits violations up to the Tsirelson bound $S_{\text{CHSH}} = 2\sqrt{2}$ [196].

Quantum steering inequalities provide an intermediate notion between mere entanglement and full Bell nonlocality [187], [197]. In the same CHSH geometry, one can construct a steering parameter S_{QS} based on combinations of $E(\alpha, \beta)$ that must satisfy $S_{\text{QS}} \leq 2$ under any local-hidden-state (LHS) model [198]. Violations certify that Alice can "steer" Bob's local state by choosing her measurement basis.

From the correlation map $E(\alpha, \beta)$, one can compute the CHSH parameter S_{CHSH} (Eq. 6.19) and the steering parameter S_{QS} for all quadruples $(\alpha, \alpha', \beta, \beta')$ in the CHSH geometry. This yields high-dimensional "S-maps":

$$S_{\text{CHSH}} : (\alpha, \alpha', \beta, \beta') \mapsto S_{\text{CHSH}}(\alpha, \alpha', \beta, \beta'), \tag{6.20}$$

$$S_{\text{QS}} : (\alpha, \alpha', \beta, \beta') \mapsto S_{\text{QS}}(\alpha, \alpha', \beta, \beta'). \tag{6.21}$$

Slices of these maps are particularly informative. Fixing $\beta' = \beta + 45°$ and viewing the subspace (α, α', β), one obtains three-dimensional maps that demarcate the hypervolumes where $S_{\text{CHSH}} > 2$ (Bell nonlocality) and $S_{\text{QS}} > 2$ (steering) (Fig. 6.4).

For the experimental EPR state, the measured S_{CHSH} map shows distinct lobes where the CHSH inequality is violated, with maximal values approaching 2.7. The corresponding steering map S_{QS} exhibits larger regions of violation, consistent with the hierarchy that steering is easier to demonstrate than Bell nonlocality [186], [187].

To quantify how "nonclassical" a given source is over the full domain, define violation ratios

$$\eta_{\text{CHSH}} = \frac{V\{S_{\text{CHSH}} > 2\}}{V\{\text{all angles}\}}, \qquad \eta_{\text{QS}} = \frac{V\{S_{\text{QS}} > 2\}}{V\{\text{all angles}\}}, \tag{6.22}$$

where $V\{\cdot\}$ is the volume (measure) in angle space. For an ideal EPR state, theory predicts $\eta_{\text{CHSH}} \approx 0.2$ and $\eta_{\text{QS}} = 1$, while product states have $\eta_{\text{CHSH}} = \eta_{\text{QS}} = 0$. These scalar figures of merit provide a compact way to compare different entangled sources.

Unbalanced and mixed bipartite states

By tuning (θ_p, ϕ_d) away from the ideal Bell-state settings or by adding controlled classical noise (e.g., stray light), one can generate unbalanced pure states and Werner-type mixed states [199]. Their full-domain N and S maps reveal how nonlocality and steering degrade as entanglement is reduced.

Unbalanced states with significant relative phase ϕ_d retain steering over wide angle regions but can lose Bell nonlocality in most of the domain; Werner states with sufficient mixing weight $1 - p$ become entirely local, with $S_{\text{CHSH}} \leq 2$ and $S_{\text{QS}} \leq 2$ everywhere (Fig. 6.5).

Calibrating quantum key distribution via S-maps

Beyond serving as general diagnostics of nonclassicality, the S-maps enable practical calibration of entanglement-based quantum key distribution (QKD) protocols, such as the E91 scheme [200], [201]. In E91, Alice and Bob choose among several polarization bases; some setting combinations are used to test CHSH or steering inequalities and thus bound Eve's information, while others generate the raw key [202].

Given an experimentally measured S-map for a particular biphoton source, one can search over all tuples of measurement settings to find those that (1) maximize S_{CHSH}

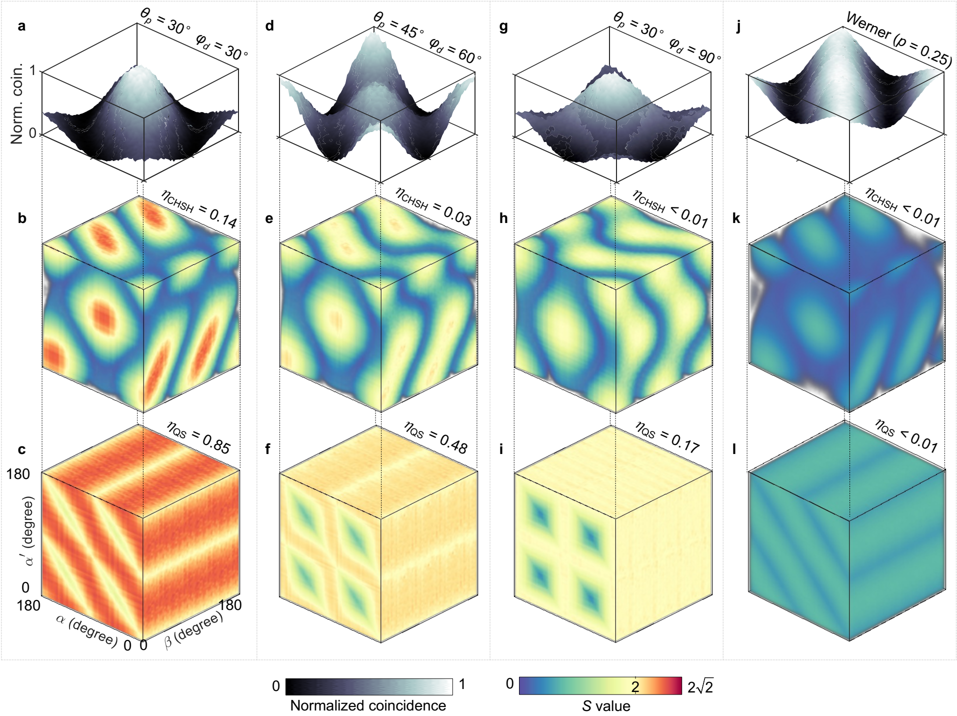

Figure 6.5: **Representative coincidence and S-maps for non-ideal sources.** Rows show (top to bottom) full-domain $N(H, H|\alpha, \beta)$, CHSH maps, and steering maps for (left to right) unbalanced pure states with different (θ_p, ϕ_d) and a Werner state with mixing parameter p. The violation volumes η_{CHSH} and η_{QS} shrink as entanglement and purity degrade.

(or S_{QS}), and (2) yield a positive asymptotic device-independent key rate under collective attacks [203], [204]. We compute key-rate maps $r(\alpha, \alpha', \beta, \beta')$ using standard entropy-accumulation-based formulas and overlay them with the S-maps to identify robust regions in angle space that support secure key generation (Fig. 6.6).

6.3 Advantages and limitations of quantum imaging

The combination of entangled or squeezed light with correlation-based detection yields a set of concrete advantages over classical imaging when sources and detectors are well characterized as above [188].

- Enhanced spatial resolution. Spatially entangled photon pairs can surpass the classical diffraction limit by effectively narrowing the point-spread function (PSF) through higher-order interference.
- Stray-light resistance and imaging through noise. Quantum coincidence imaging can be highly robust to stray light and sensor noise because only correlated

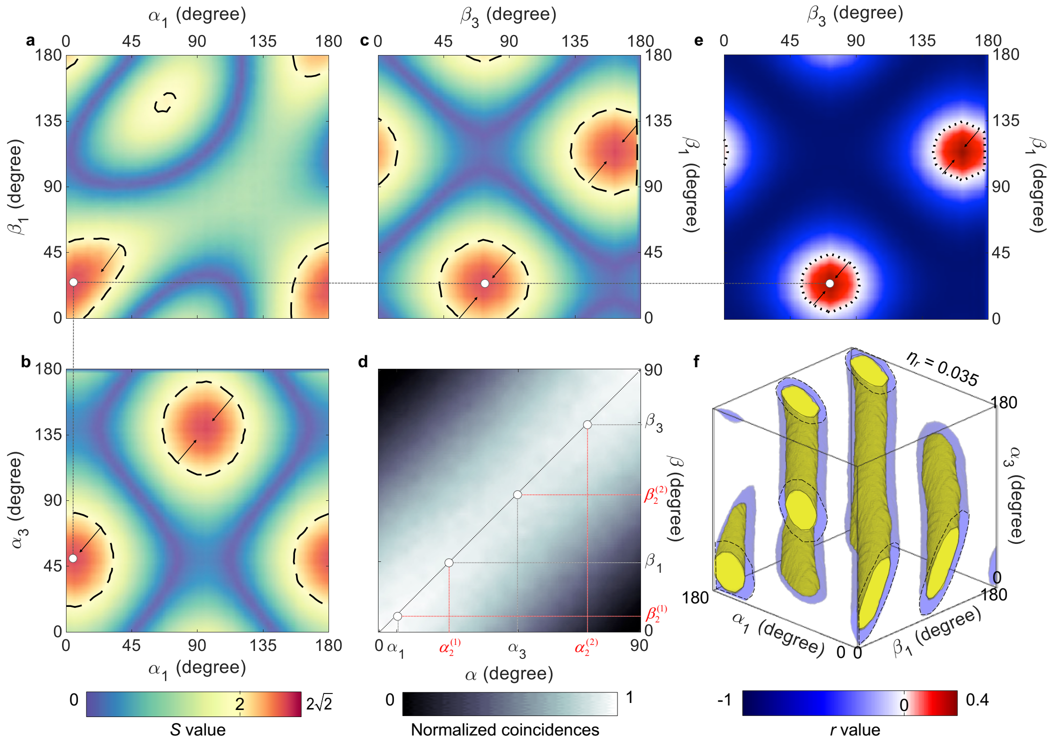

Figure 6.6: **Application of S-maps to calibrate an E91-type QKD protocol.** (a–d) Coincidence map and cross-sections of the CHSH map reveal optimal quadruples $(\alpha_1, \alpha_3, \beta_1, \beta_3)$ that maximize S_{CHSH}. (e) Associated key-rate maps $r(\alpha_1, \alpha_3, \beta_1, \beta_3)$ identify regions with positive asymptotic device-independent key rates under collective attacks.

biphoton events contribute to the reconstructed image. This robustness is particularly valuable for biological microscopy, where samples may need to be imaged under ambient lighting or in scattering environments, and where increasing the probe intensity is undesirable.

- Sub-shot-noise (SSN) performance. By exploiting intensity-difference squeezing or coincident-count statistics, QI schemes can reach or surpass the classical shot-noise limit in estimating transmissivity or phase [185]. For dose-limited imaging—for example in live-cell microscopy—this allows improved CNR at fixed photon exposure, or equivalently, reduced dose at matched image quality.

- Wavelength flexibility and undetected-photon imaging. SPDC automatically generates wavelength-correlated pairs. In degenerate operation, detecting at 2λ can emulate imaging at λ in the sense of spatial-frequency support; in nondegenerate operation, undetected-photon imaging can probe a sample at a wavelength that is difficult to detect (e.g., mid-IR) while detecting at a convenient visible or near-IR wavelength [188], [191]. This opens possibilities for combining biologically friendly illumination bands with low-noise, low-cost detectors.

- Remote sensing and polarization control. Because entanglement correlations are independent of separation (up to losses and decoherence), QI also suggests new modalities for remote sensing [188], [193]. This could be useful in scenarios where direct access to the returning signal beam is limited or where in-situ polarization control is difficult.

Despite its advantages, QI currently faces several practical limitations. High-quality sources of entangled or squeezed light require precise alignment, phase stability, and often bulky or cryogenic components (e.g., superconducting single-photon photodiode arrays or SNSPDs). SPDC efficiencies are low ($\sim 10^{-6}$ per pump photon), limiting photon flux and increasing acquisition time for large fields of view [188]. Scaling QI to volumetric imaging or very large samples demands massively parallel sources and detectors, along with tailored reconstruction algorithms.

Nonetheless, rapid progress is being made on brighter entangled sources, integrated photonics, and single-photon cameras [205]. As these technologies mature, QI techniques such as ICE, QMC, ghost imaging, and quantum holography are poised to transition from table-top demonstrations to practical tools in biomedicine, materials science, and remote sensing.

6.4 Dissertation outline (Chapters VII and VIII)

Chapter VII focuses on scanning-based quantum imaging using spatial and polarization entanglement. The chapter discusses system architecture, coincidence-based acquisition, and birefringence quantification, and reports experiments that achieve high signal-to-noise ratios, light suppression, and imaging of biological specimens with entangled-photon illumination.

Chapter VIII describes the implementation of widefield quantum microscopy based on coincidence detection. It introduces the concept of resolution enhancement at the Heisenberg limit, discusses the role of balanced optical paths in enabling effective wavelength reduction, and reports super-resolved imaging of cellular structures using entangled photon pairs.

Chapter 7

SCANNING-BASED QUANTUM IMAGING OF BIOLOGICAL ORGANISMS THROUGH SPATIAL AND POLARIZATION ENTANGLEMENT

[1] Y. Zhang†, Z. He†, X. **Tong**†, D. C. Garrett, R. Cao, and L. V. Wang, "Quantum imaging of biological organisms through spatial and polarization entanglement," *Science Advances*, 2024. DOI: `10.1126/sciadv.adk1495`,

7.1 Introduction

Optical imaging has been widely used to noninvasively investigate the structures and dynamics of various physical and biological systems [206], [207]. The key advantage of optical imaging is that the interaction of non-ionizing light with molecules provides rich molecular information about biological samples. Aided by the convenience and compactness of optical systems, optical imaging has served as the workhorse for biological researchers and medical practitioners behind a wide variety of discoverie [208].

In the past two decades, advanced optical imaging techniques have been developed to allow super-resolution [206], [207] and high-speed bioimaging [209]–[211]. However, to achieve high resolution and high imaging speed, most optical imaging techniques require intense illumination that can disrupt or damage the biological processes under investigation [207]. Low-intensity illumination, on the other hand, leads to low SNR due to shot noise and stray light.

Recently, to overcome the limitations of optical imaging techniques that rely on classical light sources, quantum imaging approaches that use correlated, entangled, or squeezed photons have been developed [207], [212]–[215]. Compared with classical optical imaging, quantum imaging offers several advantages [216]. First, the classical shot-noise limit can be broken, allowing for SSN imaging under low-intensity illumination [215], [217]–[221]. Second, stray light can be suppressed [214], [222], [223]. Third, super-resolution imaging beyond the diffraction limit can be enabled [207], [224]–[229]. Empowered by these advantages, quantum imaging has been employed to investigate biological specimens [207], [215], which have complex structures and may be susceptible to photobleaching and thermal damage.

Despite these advantages, quantum images of biological specimens reported to date still suffer from low SNR because (1) the conditions required to achieve SSN are stringent [217], [219]–[221], [230] and (2) the SNRs in most quantum imaging approaches are low [214], [216], [223]. Moreover, existing quantum imaging approaches usually have low resolvable pixel counts (that is, the ratio of the FOV to the spatial resolution) [207], [212]–[215] and thus are not suited for practical biological studies, which often demand systematic investigation of multiple parts of a biological system with a wide FOV across a whole organism.

Finally, quantum imaging techniques so far have mainly measured transmittance (absorption) or phase contrast, whereas classical techniques support additional contrasts such as birefringence [206], [207], [231]. Existing quantum imaging approaches have not demonstrated quantitative measurement of both the phase retardation and the principal refractive index axis angle of a biological specimen.

Here, we present ICE, a higher-SNR, greater-resolvable-pixel-count, and birefringence-sensitive quantum imaging technique that generates high-quality images of biological specimens. Under low-intensity illumination, ICE employs a new SSN algorithm that utilizes the covariance of the raw images to achieve a higher SNR than the classical counterpart. Concurrently, ICE substantially increases the SNR over existing quantum imaging techniques by accommodating multiple spatial modes of the entangled photon pairs in each pixel, where a single spatial mode is constrained by the diffraction limit of the system [232], [233]. Table 7.1 summarizes the key advantages of ICE over other QI modalities.

Table 7.1: Advantages of ICE over other QI configurations.

Technique	**Sample**	**Resolvable pixel count**	**Acquisition time per resolvable pixel (SNR = 10)**
Ref. [212]	Wasp wing	2401	1.9 s
Ref. [207]	NIH 3T3 cells	121	1.1 s
Ref. [228]	Quartz crystal	828	50 s
Ref. [213]	Mouse heart	784	0.2 s
Ref. [215]	Yeast cell	2500	0.8 s
Ref. [193]	Bird feather	968	37.3 s
ICE (our work) [194]	Zebrafish / mouse brain	~258,432	0.06 s

The spatial resolution of ICE is determined by both the signal and idler photons through a quantum effect that we term the entanglement pinhole. In the entanglement pinhole effect, when an entangled photon pair is captured concurrently by two

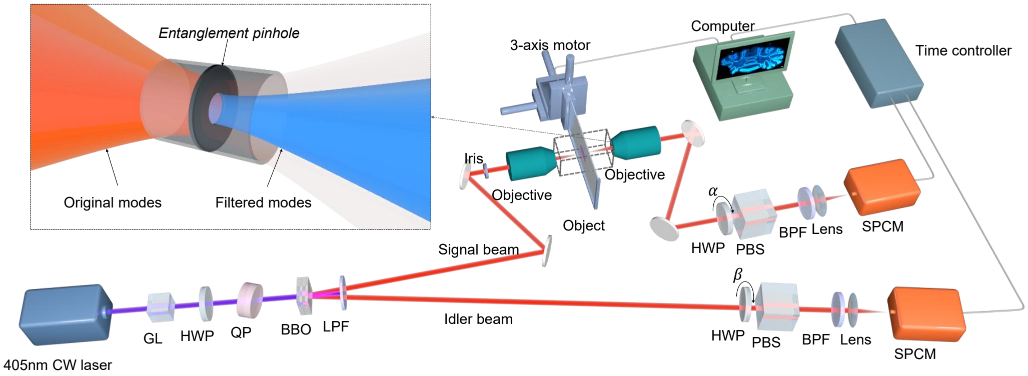

Figure 7.1: **Experimental setup schematics**. CW, continuous wave; GL, Glan–Laser polarizer; HWP, half-wave plate; QP, quartz plate; BBO, β-barium borate crystals; LPF, long-pass filter; PBS, polarizing beam splitter; BPF, band-pass filter; SPCM, single-photon counting module. Inset, illustration of the entanglement pinhole.

detectors, one detector functions non-classically as a pinhole on the object being imaged by the other detector. Further, ICE increases the resolvable pixel counts indefinitely through raster scanning and is 25 times more resilient to stray light than classical imaging. Consequently, ICE enables quantum imaging of whole-organ (mouse brain) slices and organisms (zebrafish) with a FOV of up to 7 mm × 4 mm, and can be operated in the presence of ambient lighting, thus suitable for practical biological studies.

Finally, ICE exploits the polarization entanglement of the photon pairs for ghost birefringence imaging, where the birefringence properties of an object can be remotely and instantly measured without changing the polarization states of the photons incident on the object. The quantum advantages of ICE therefore enable the observation of biological specimens under conditions that cannot be satisfied with classical imaging, as well as the remote sensing of birefringence.

7.2 Sub-shot-noise quantum imaging using multi-mode entangled photons

In ICE (Fig. 7.1), we use two BBO nonlinear crystals with perpendicularly aligned optical axes to produce hyperentangled photon pairs, which are simultaneously entangled in spatial mode, polarization, and energy [189], [234] through the type-I SPDC process. A continuous-wave pump laser illuminates the BBO crystals to generate signal and idler photons. The pump beam is blocked after the crystals so that only the SPDC photons are used for imaging.

The signal photons are routed through the object arm, where they probe the sample placed on a microscope slide. The slide is mounted on a three-axis motorized translation stage for raster scanning. The transmitted signal photons are collected by an objective lens and directed to a single-photon detector. The idler photons are routed through a reference arm and detected by another single-photon detector without passing through the object. Both detectors are temporally synchronized so that coincidence detection can be performed.

In each acquisition, ICE records three images: the signal image $N_s(\mathbf{r})$, the idler image $N_i(\mathbf{r})$, and the coincidence image $N_c(\mathbf{r})$. Here, N_s and N_i contain contributions from both SPDC photon pairs and stray light, while N_c is dominated by true coincidences arising from entangled photon pairs. Classical imaging can be realized from either the signal or idler singles counts. ICE images are formed from coincidence counts between the two arms.

To enhance the SNR of the transmittance measurement, we introduce a covariance-over-variance (CoV) SSN retrieval algorithm that exploits the correlations between the signal and idler beams (Fig.7.2). Specifically, the single-photon images contain contributions from both entangled SPDC photon pairs (with mean μ_{SPDC}) and stray light (with mean μ_{stray}). We assume identical detector efficiencies and backgrounds for the signal and idler channels, denoted η.

The imaging task is to recover the object transmittance $T(\mathbf{r})$. Classically, it is estimated by

$$T_0(\mathbf{r}) = \frac{N_s(\mathbf{r})}{N_{s,0}(\mathbf{r})}, \tag{7.1}$$

where $N_{s,0}$ denotes the signal image without the object. In practice, ICE approximates $N_{s,0}$ using the spatial average of a background region $N_{s,b}(\mathbf{r})$.

Two families of SSN algorithms have traditionally been employed. The first uses a ratio between the signal and idler channels:

$$T_1(\mathbf{r}) = \frac{N_s(\mathbf{r})}{N_i(\mathbf{r})} \cdot \frac{\langle N_i(\mathbf{r})\rangle_{\mathbf{r}}}{\langle N_{s,b}(\mathbf{r})\rangle_{\mathbf{r}}}, \tag{7.2}$$

which leverages pair correlations to suppress uncorrelated noise.

The second strategy is optimized subtraction:

$$N_s^{\text{SSN}}(\mathbf{r}) = N_s(\mathbf{r}) - k(\mathbf{r})\, \Delta N_i(\mathbf{r}), \tag{7.3}$$

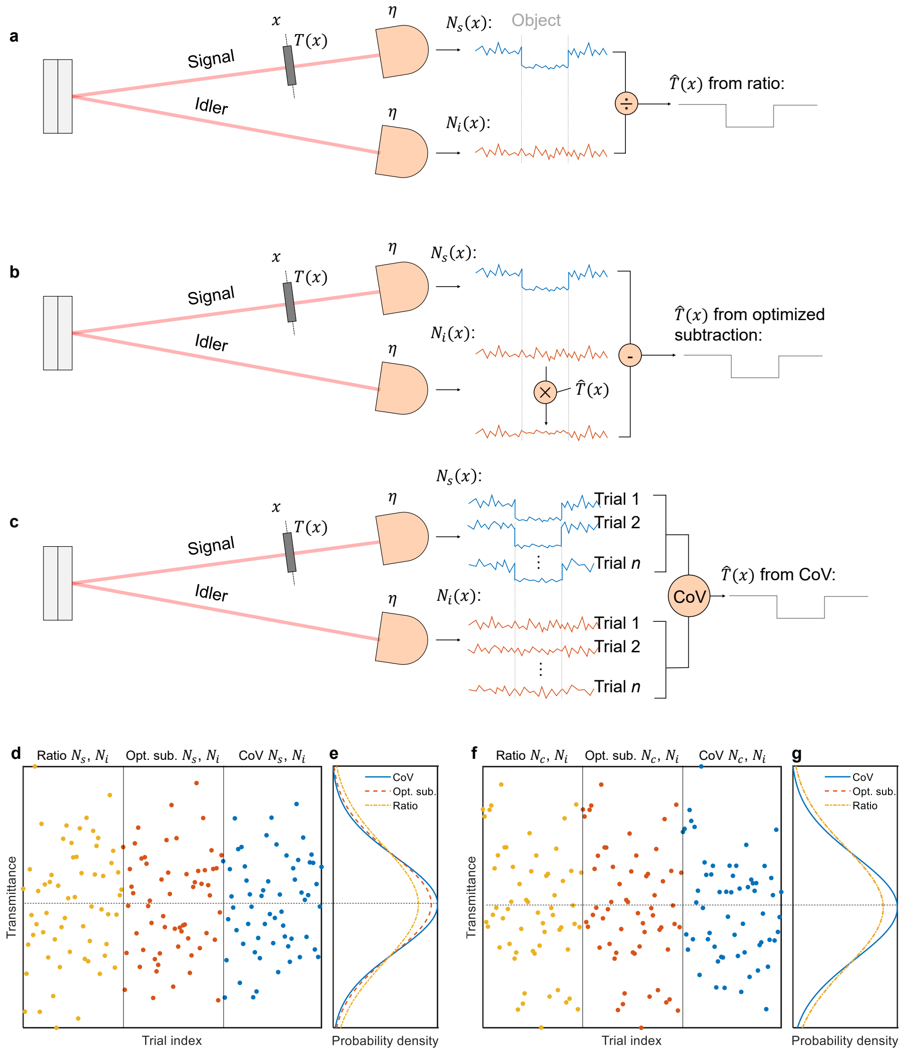

Figure 7.2: **SSN algorithms and performances**. (a) Workflow of the ratio algorithm. (b) Workflow of the optimized subtraction algorithm. (c) Workflow of the CoV algorithm. (d) transmittance of the object experimentally measured using the ratio, optimized subtraction, and CoV algorithms with N_s and N_i. (e) histograms of the transmittance measured in (d). (f) transmittance of the object experimentally measured using the ratio, optimized subtraction, and CoV algorithms with N_c and N_i. (g) histograms of the transmittance measured in (f).

where $\Delta N_i(\mathbf{r}) = N_i(\mathbf{r}) - \langle N_i \rangle_{\mathbf{r}}$ and $k(\mathbf{r})$ is a spatially varying factor ideally proportional to the (unknown) transmittance $T(\mathbf{r})$. Using an estimated $\hat{T}(\mathbf{r})$, one obtains

$$T_2(\mathbf{r}) = \frac{N_s(\mathbf{r})}{\langle N_{s,b} \rangle_{\mathbf{r}}} - \hat{T}(\mathbf{r})\,\eta \left(\frac{\mu_{\text{SPDC}}}{\mu_{\text{stray}} + \mu_{\text{SPDC}}} \right)^2 \frac{\Delta N_i(\mathbf{r})}{\langle N_{s,b} \rangle_{\mathbf{r}}}. \tag{7.4}$$

Although both methods outperform classical estimation, they require prior knowledge of $T(\mathbf{r})$ or assumptions about photon statistics and stray-light suppression.

Using time-lapsed stacks $N_s(\mathbf{r}, t)$ and $N_i(\mathbf{r}, t)$, the CoV algorithm adopts the structure of optimized subtraction but computes $k(\mathbf{r})$ by minimizing the temporal variance of Eq. (7.3). The minimizer is

$$k^*(\mathbf{r}) = \frac{\mathrm{Cov}_t[N_s(\mathbf{r}, t), N_i(\mathbf{r}, t)]}{\mathrm{Var}_t[N_i(\mathbf{r}, t)]}, \tag{7.5}$$

yielding the CoV transmittance estimate:

$$T_3(\mathbf{r}) = \frac{N_s(\mathbf{r})}{\langle N_{s,b} \rangle_{\mathbf{r}}} - \frac{\mathrm{Cov}_t[N_s(\mathbf{r}, t), N_i(\mathbf{r}, t)]}{\mathrm{Var}_t[N_i(\mathbf{r}, t)]} \frac{\Delta N_i(\mathbf{r})}{\langle N_{s,b} \rangle_{\mathbf{r}}}. \tag{7.6}$$

The minimized output variance becomes

$$\mathrm{Var}_t[N_s^{\mathrm{SSN}}(\mathbf{r}, t)] = \mathrm{Var}_t[N_s(\mathbf{r}, t)] \left(1 - \rho^2_{N_s,N_i}\right), \tag{7.7}$$

where ρ_{N_s,N_i} is the temporal Pearson correlation coefficient. Because $\rho^2 \geq 0$, the CoV method guarantees SNR improvement over classical estimation.

When only a single acquisition is available, ICE uses spatial redundancy rather than temporal variations. Pixel values are binned into L subsets, and for each subset (N_s^ℓ, N_i^ℓ), an analog of Eq. (7.5) is computed:

$$k_\ell^* = \frac{\mathrm{Cov}_{\mathbf{r}}[N_s^\ell(\mathbf{r}), N_i^\ell(\mathbf{r})]}{\mathrm{Var}_{\mathbf{r}}[N_i^\ell(\mathbf{r})]}. \tag{7.8}$$

Summing over the binary masks $M_\ell(\mathbf{r})$ reconstructs a spatially varying $k^*(\mathbf{r})$, enabling the single-frame estimator:

$$T_4(\mathbf{r}) = \frac{N_s(\mathbf{r})}{\langle N_{s,b} \rangle_{\mathbf{r}}} - \left[\sum_{\ell=1}^{L} k_\ell^* M_\ell(\mathbf{r})\right] \frac{\Delta N_i(\mathbf{r})}{\langle N_{s,b} \rangle_{\mathbf{r}}}. \tag{7.9}$$

Compared with state-of-the-art SSN methods such as the ratio and optimized subtraction algorithm [219], [221], [230], our CoV algorithm achieves higher SNRs for both classical and quantum imaging, as demonstrated in simulations and experiments. The CoV algorithm can be applied to the singles images (N_s and N_i) or the coincidence image N_c to obtain sub-shot-noise transmittance maps.

7.3 Entanglement-pinhole-enabled high-resolution and large-depth-of-field imaging

Despite the higher coincidence rate and SNR, acquiring images by raster scanning a multi-mode beam is generally undesired in classical imaging, because the multi-mode beam leads to a broad PSF and consequently a poor spatial resolution. In

ICE, however, the spatially entangled photon pairs enable the entanglement pinhole effect: when a signal–idler pair is detected in coincidence, the spatial correlation between the two photons ensures that the detection of the idler photon effectively acts as a non-classical pinhole on the object plane in the signal arm.

Relying on true coincidences from spatially entangled photons, the entanglement pinhole filters out a portion of the spatial modes in the SPDC beam and improves both spatial resolution and depth of field (DOF) over classical imaging. The CoV algorithm, combined with coincidence detection, thus yields sub-shot-noise images with enhanced resolution and robustness to stray light.

To experimentally investigate the spatial resolution and DOF of ICE, we imaged a USAF resolution target with both classical imaging and ICE. In the classical case, only one arm of the SPDC setup and the singles counts were used. In ICE, we used coincidence counts between the signal and idler arms.

As shown in Fig. 7.3a, the classical image of the USAF target can only resolve groups 4 and 5, whereas ICE can clearly resolve groups 6 and 7. This indicates that ICE achieves finer spatial resolution than classical imaging under similar conditions. Furthermore, ICE maintains higher resolution over a long axial distance. By translating the sample along the z-axis, we recorded images at different defocus positions to quantify the DOF.

To quantify resolution and DOF, we acquired edge-spread functions (ESFs) at different z positions by taking intensity profiles across sharp edges in the images. We then computed the corresponding line-spread functions (LSFs) by differentiating the ESFs and measured their full width at half maximum (FWHM) to estimate the spatial resolution. The measured resolutions as functions of z are summarized in Fig. 7.3c, where the means and standard errors are shown. ICE consistently exhibits finer resolution than classical imaging across the examined axial range.

To further characterize the DOF, we repeated the resolution analysis with a finer axial step size (10 μm) over approximately 700 μm along the z-axis (Fig. 7.3d). After aligning the foci by shifting the ICE curve by 43 μm along z, we fitted the experimental data and determined the focal resolutions of classical imaging and ICE to be 14.4 ± 0.6 μm and 10.4 ± 0.4 μm, respectively, demonstrating that ICE improves the resolution by 38% over classical imaging. The DOFs are determined to be 92 ± 2 μm and 95 ± 2 μm for classical imaging and ICE, respectively. ICE thus achieves improved resolution while preserving a comparable DOF.

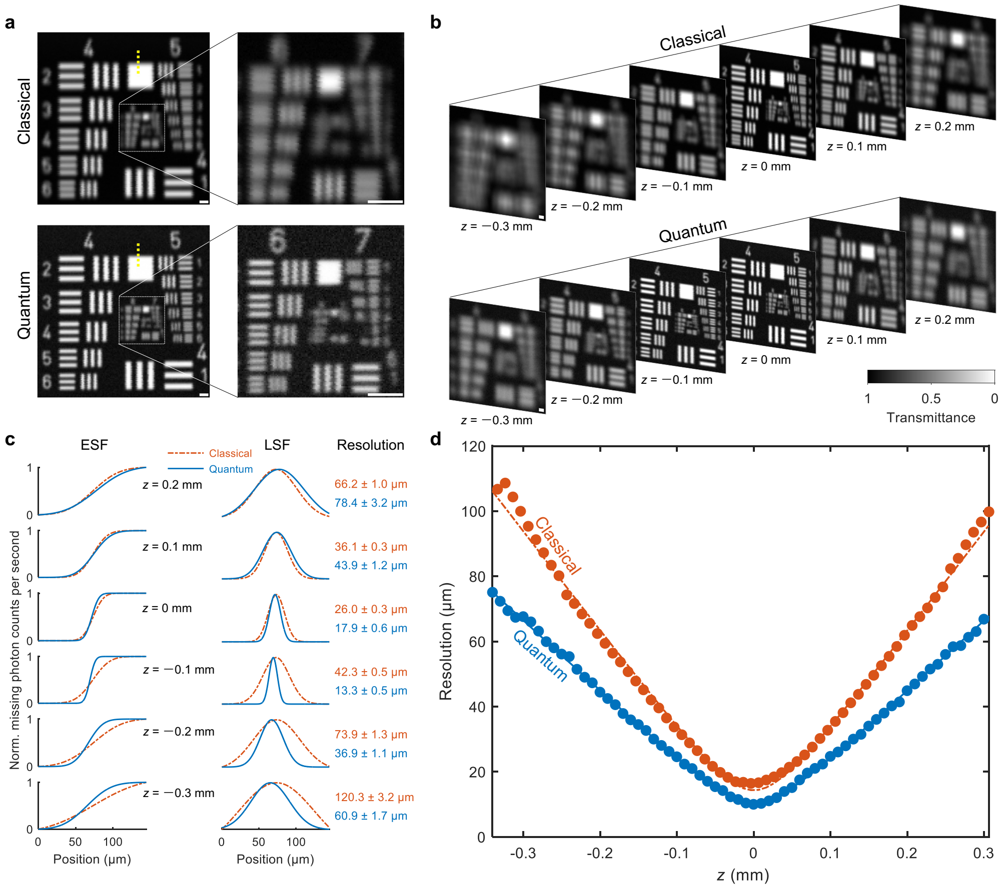

Figure 7.3: **Effect of the entanglement pinhole on ICE.** (a,b) Classical imaging and ICE of a USAF resolution target at focus (a) and at different z positions (b), where $z = 0$ mm denotes the focus of classical imaging. (c) Edge-spread functions (ESFs), line-spread functions (LSFs), and spatial resolutions measured at different z positions. The ESFs were fitted from the profiles of the yellow dotted lines in (a). The means and standard errors of the resolution are shown on the right. (d) Resolution versus z for classical imaging and ICE. Dots represent experimental measurements. Solid and dash-dotted lines denote fits. Norm., normalized. Scale bars, 50 μm.

Compared with existing quantum imaging techniques that have typically been demonstrated with thin biological samples (e.g., thickness < 10 μm) [207], [212]–[215], ICE provides a larger DOF, enabling volumetric imaging and the interrogation of thicker specimens. The entanglement pinhole thus allows ICE to combine high resolution with a large DOF in a way that is difficult to achieve with classical wide-field or confocal imaging under similar photon budgets.

7.4 Quantum imaging of biological organisms in the presence of stray light

By raster scanning the object, ICE provides a FOV that can be extended indefinitely. We imaged a slice of a whole organ (the cerebellum of a mouse brain) with a 7 mm×4 mm FOV. The ICE image outperforms the classical counterpart with higher resolution, as evidenced by line profiles taken across regions of interest. Narrower trenches and sharper peaks in the ICE profiles confirm improved resolution across the large FOV.

In addition to the large FOV, ICE demonstrates robust resistance to stray light. To illustrate this, we imaged a whole zebrafish under ambient-light-like conditions using both classical imaging and ICE (Fig. 7.4a). The sample was illuminated by the entangled SPDC photons, while a light-emitting diode (LED) was used as a controllable stray light source. The zebrafish images reveal that ICE maintains high contrast and structural visibility even when the classical image becomes severely degraded by stray light.

To quantify robustness to stray light, we imaged carbon fibers under varying LED optical powers using both classical imaging and ICE (Fig. 7.4b). For each LED power, we computed the structural similarity index measure (SSIM) between the image acquired with stray light and the corresponding reference image acquired without stray light. The SSIM values as functions of LED power are plotted in Fig. 7.4c. The top panel shows the individual SSIM curves for classical imaging and ICE, with a dashed horizontal line indicating a threshold (SSIM = 0.1) used to define significant degradation. From these curves, we identify the LED powers at which the SSIM drops below the threshold, obtaining 0.18 mW and 4.41 mW for classical imaging and ICE, respectively. ICE therefore suppresses stray light approximately 25 times more effectively than classical imaging.

The bottom panel of Fig. 7.4c shows the difference between the two SSIM curves, ΔSSIM, further highlighting ICE's advantage. This robustness is attributed to coincidence detection: while stray light can strongly degrade singles images, it acts as an uncorrelated source producing negligible coincidence counts, and thus has minimal impact on ICE images.

Because ICE can be operated in the presence of ambient lighting, it is well suited for practical biological imaging scenarios where strict light shielding is difficult, such as in open microscopes, *in vivo* preparations, or field-deployable instruments.

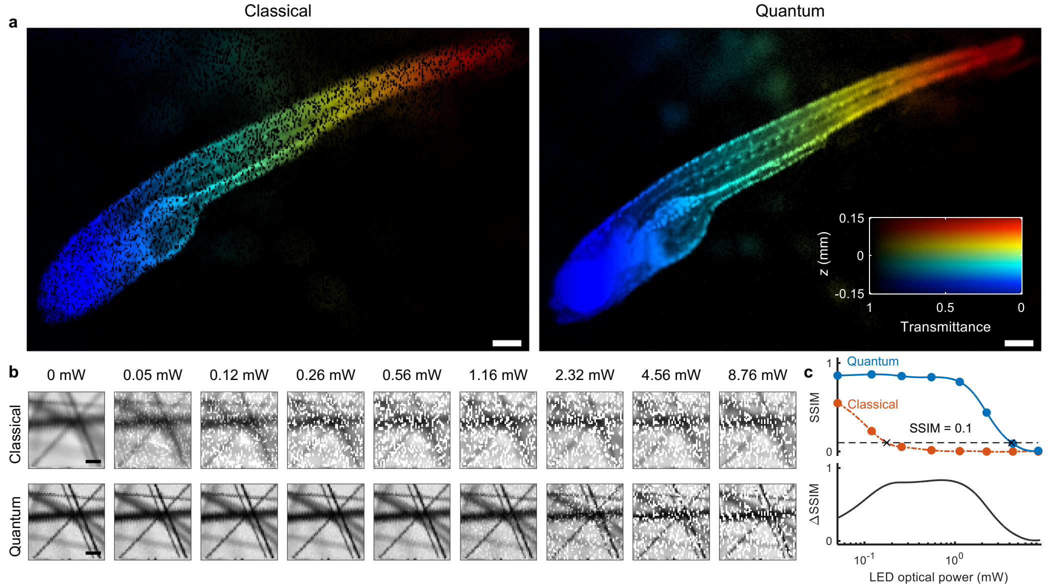

Figure 7.4: **ICE in the presence of stray light.** (a) Classical and ICE images of a whole zebrafish in the presence of stray light. Pseudo-colors encode the z positions of the sample. Scale bars, 200 μm. (b) Classical and ICE images of carbon fibers acquired at different stray-light optical powers. Scale bars, 100 μm. (c) Top: structural similarity index measure (SSIM) calculated between the images in (b) and reference images acquired without stray light. The black dashed line indicates a threshold (SSIM = 0.1) used to quantify the robustness of ICE and classical imaging. Bottom: difference between the two SSIM curves, ΔSSIM.

7.5 Ghost birefringence imaging of a whole zebrafish

In addition to intensity- and transmittance-based contrast, many biological structures exhibit birefringence, which encodes information about molecular organization and anisotropy [206], [207], [231], [235], [236]. Conventional birefringence imaging typically relies on sequential polarization-state manipulation and precise control of the polarization of the light incident on the sample. ICE, using polarization-entangled photon pairs, enables *ghost* birefringence imaging: the birefringent properties of the object are inferred from measurements in the idler arm, while the polarization states of the photons probing the object are not changed.

To demonstrate ghost birefringence imaging, we used ICE to image a whole zebrafish. In this experiment, polarization analysis of the signal and idler beams was performed with polarizers placed in the respective arms. The polarizer in the signal arm was fixed at a constant angle θ_s, while the polarizer in the idler arm was rotated to different angles θ_i, yielding a set of ICE images acquired under different polarization-analysis conditions (Fig. 7.5a).

From these ICE images, we extracted the transmittance T, the principal refractive index axis angle, and the phase retardation between the principal axes at each spatial location as follows. In the experiment, the signal-arm polarization is fixed at $\alpha = 0°$, while the idler-arm polarizer is rotated through $\beta = 0°, 45°, 90°, 135°$. Despite constant illumination polarization on the sample, varying β modulates the coincidence counts according to the object's birefringence characteristics.

Let the object be a general linear birefringent element characterized by a Mueller matrix

$$X_{\Delta,\theta} = \begin{bmatrix} 1 & 0 & 0 & 0 \\ 0 & \cos^2 2\theta + \sin^2 2\theta \cos\Delta & \cos 2\theta \sin 2\theta (1-\cos\Delta) & -\sin 2\theta \sin\Delta \\ 0 & \cos 2\theta \sin 2\theta (1-\cos\Delta) & \sin^2 2\theta + \cos^2 2\theta \cos\Delta & \cos 2\theta \sin\Delta \\ 0 & \sin 2\theta \sin\Delta & -\cos 2\theta \sin\Delta & \cos\Delta \end{bmatrix}, \tag{7.10}$$

where θ is the orientation of the principal refractive index axis and Δ is the phase retardation. Under coincidence detection, ICE measures Stokes vectors that correspond to the Mueller-transformed illumination states.

For each idler polarization β, the measured Stokes vector is

$$\mathbf{S}_{\beta=0^\circ} = X_{\Delta,\theta} \begin{bmatrix} 1 & 1 & 0 & 0 \end{bmatrix}^T T, \tag{7.11}$$

$$\mathbf{S}_{\beta=45^\circ} = X_{\Delta,\theta} \begin{bmatrix} 1 & 0 & 1 & 0 \end{bmatrix}^T T, \tag{7.12}$$

$$\mathbf{S}_{\beta=90^\circ} = X_{\Delta,\theta} \begin{bmatrix} 1 & -1 & 0 & 0 \end{bmatrix}^T T, \tag{7.13}$$

$$\mathbf{S}_{\beta=135^\circ} = X_{\Delta,\theta} \begin{bmatrix} 1 & 0 & -1 & 0 \end{bmatrix}^T T, \tag{7.14}$$

where T represents the overall transmission of the object.

Evaluating the transformed Stokes vectors yields four coincidence intensities,

$$N_{0^\circ} = \frac{T}{2}\left(1 + \cos^2 2\theta + \sin^2 2\theta \cos\Delta\right), \tag{7.15}$$

$$N_{45^\circ} = \frac{T}{2}\left(1 + \cos 2\theta \sin 2\theta (1-\cos\Delta)\right), \tag{7.16}$$

$$N_{90^\circ} = \frac{T}{2}\left(1 - \cos^2 2\theta - \sin^2 2\theta \cos\Delta\right), \tag{7.17}$$

$$N_{135^\circ} = \frac{T}{2}\left(1 - \cos 2\theta \sin 2\theta (1-\cos\Delta)\right). \tag{7.18}$$

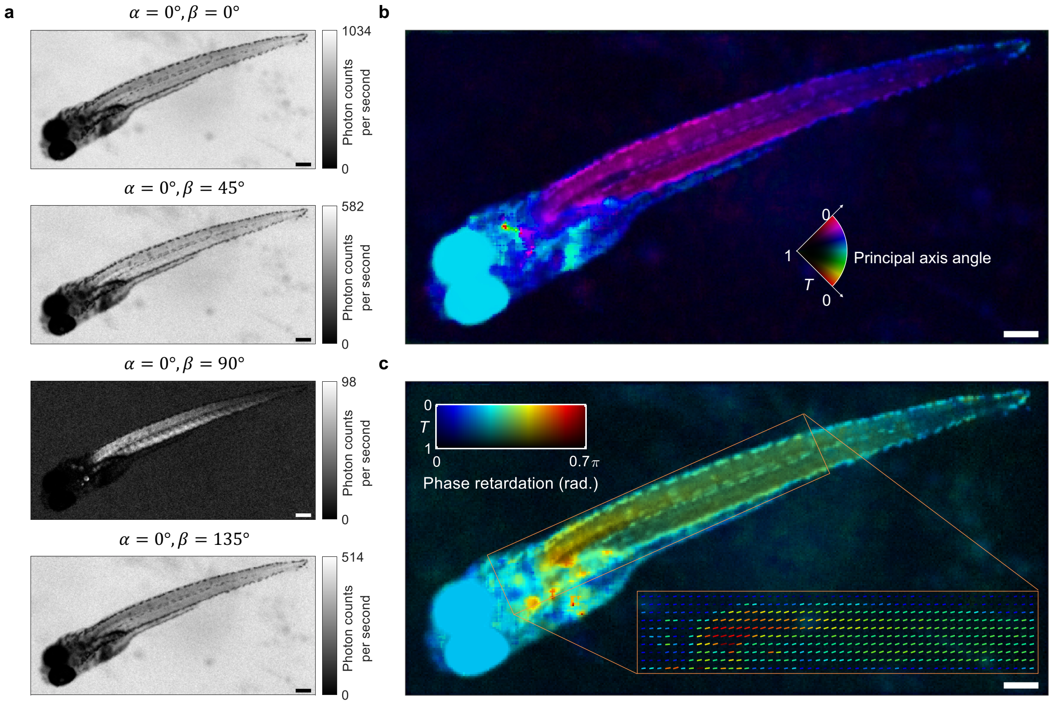

Figure 7.5: **Ghost birefringence imaging of a whole zebrafish with ICE.** (a) ICE images acquired with a signal-arm polarizer at a constant angle θ_s and an idler-arm polarizer at a variable angle θ_i. (b) Transmittance (T) and principal refractive index axis angle (pseudo-colors) calculated using the ICE images in (a). (c) Transmittance (T) and phase retardation between the two refractive index axes (lines and pseudo-colors) calculated using the ICE images in (a). Scale bars, 200 μm.

From these measurements, the object's birefringence properties follow directly:

$$T = \tfrac{1}{2}\left(N_{0^\circ} + N_{45^\circ} + N_{90^\circ} + N_{135^\circ}\right), \tag{7.19}$$

$$\theta = \tfrac{1}{2}\tan^{-1}\left(\frac{2N_{90^\circ}}{N_{45^\circ} - N_{135^\circ}}\right), \tag{7.20}$$

$$\Delta = \cos^{-1}\left(1 - \frac{N_{45^\circ} - N_{135^\circ}}{2 + \dfrac{4N_{90^\circ}^2}{N_{90^\circ}\left(N_{0^\circ} + N_{45^\circ} + N_{90^\circ} + N_{135^\circ}\right)}}\right). \tag{7.21}$$

The principal axis orientation map and the transmittance map are shown in Fig. 7.5(b). The phase retardation map, together with the transmittance, is shown in Fig. 7.5c. These maps reveal spatially varying birefringence features across the zebrafish, including structures that are not apparent in pure intensity images.

Because polarization entanglement correlates the polarization states of the signal and idler photons, measuring the idler photon's polarization state remotely deter-

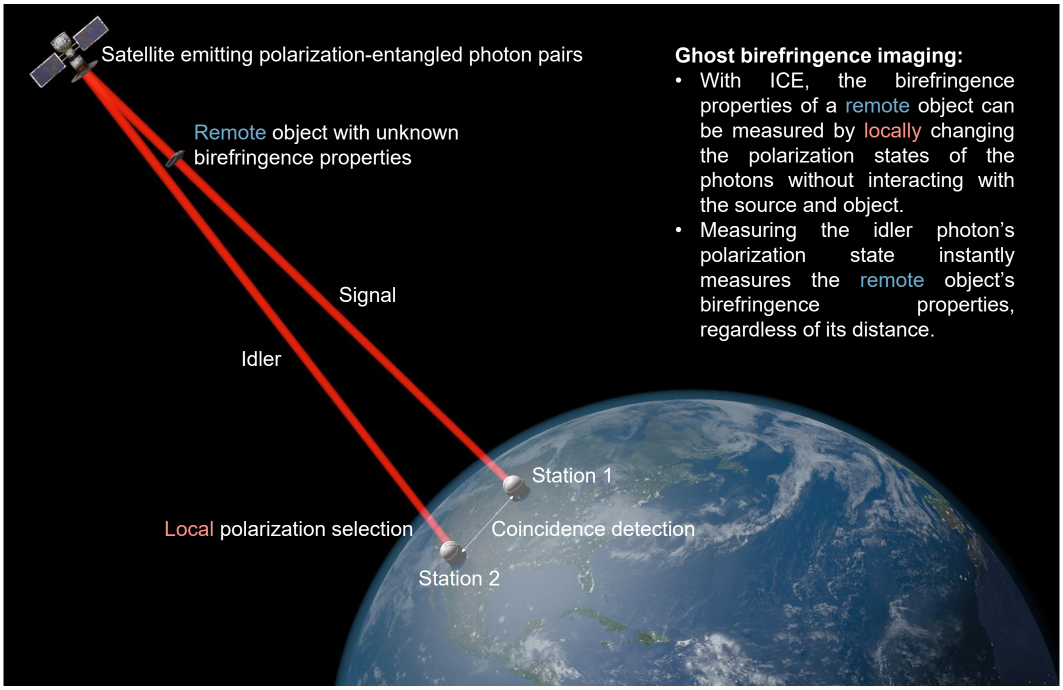

Figure 7.6: **Potential application of quantitative quantum birefringence imaging in remote sensing.** With a satellite emitting polarization-entangled photon pairs, ICE can quantify the birefringence properties of a remote object by changing the polarization states of the photons without interacting with the source and the object. Through polarization entanglement, measuring the idler photon's polarization state instantly determines the incident signal photon's and, consequently, the remote object's full birefringence properties, regardless of its distance.

mines the effective polarization state of the signal photon incident on the object. Consequently, the birefringence properties of the object can be inferred without physically changing the polarization of the light that illuminates the sample. This feature enables remote and instantaneous measurement of birefringence, which can be advantageous in situations where the source cannot be controlled in real time or is inaccessible (for example, in remote sensing scenarios).

7.6 Discussion

Although imaging by coincidence can, in principle, be achieved with classical light sources [237], the SNR of the resulting image is generally limited. In particular, classical thermal or pseudo-thermal sources do not provide the strong non-classical correlations required for the entanglement pinhole effect and the SSN performance demonstrated by ICE. The advantages of ICE arise from the use of hyperentangled photon pairs and the combination of spatial and polarization entanglement.

First, by accommodating multiple spatial modes of entangled photon pairs in each pixel, ICE increases the total photon flux and improves SNR without sacrificing resolution. In contrast, existing quantum imaging approaches often work with a small number of spatial modes and low resolvable pixel counts [207], [212]–[215]. Second, the entanglement pinhole effect leverages spatial correlations to narrow the effective PSF and increase DOF, a feature that is absent in classical multi-mode imaging. Third, because coincidence detection is insensitive to uncorrelated stray light, ICE suppresses stray light far more effectively than classical imaging under similar conditions, as demonstrated by the 25-fold improvement in robustness.

ICE therefore complements classical imaging techniques rather than replacing them. In regimes where high photon flux and strong illumination are acceptable, classical techniques may still be preferable, especially when speed is the dominant constraint. However, in regimes where low illumination, high SNR, large FOV, and polarization/birefringence information are simultaneously required, ICE provides a unique combination of capabilities that cannot be achieved with classical imaging alone.

Finally, as envisioned in Fig. 7.6, because entangled photon sources and single-photon detectors continue to improve, we anticipate that ICE can be extended to faster imaging, higher-dimensional measurements (for example, including spectral information), and long-distance imaging, including satellite-based or remote-sensing applications [238], [239]. ICE thus represents a step toward practical quantum imaging of complex biological systems and other samples that are challenging for classical optical methods.

Chapter 8

WIDEFIELD QUANTUM SUPER-RESOLUTION MICROSCOPY OF CELLS

[1] Z. He†, Y. Zhang†, X. **Tong**†, L. Li, and L. V. Wang, "Quantum microscopy of cells at the heisenberg limit," *Nature Communications*, 2023. DOI: `10.1038/s41467-023-38191-4`,

8.1 Introduction

Since the first realizations of entangled photon sources, biphoton states have become central resources in several areas of quantum science and technology, including photonic quantum computing [240], precision metrology [241], [242], and quantum communication and information processing [243], [244]. The strong correlations shared by the photons in a pair naturally suggest strategies for surpassing bounds imposed on classical optical fields, such as the diffraction limit and constraints derived from the uncertainty principle [245], [246]. Experiments on biphoton diffraction have shown that the resulting pattern can be narrowed by about a factor of two relative to classical illumination [247]–[249], indicating that entangled-photon imaging can, in principle, realize super-resolution beyond linear classical optics [250].

Many platforms for biphoton-based imaging have been explored. On the source side, SPDC in nonlinear crystals such as BBO [251] and periodically poled potassium titanyl phosphate (PPKTP) [191] is widely used to generate entangled photon pairs [252]–[254]. On the detection side, several types of single-photon devices have been adopted. Single-pixel single-photon avalanche diodes (SPADs) offer excellent timing resolution and permit direct coincidence detection, but they lack spatial resolution. SPAD arrays extend this concept to multiple pixels, providing spatial information, but current implementations are restricted to relatively modest pixel counts [255]–[257].

Electron-multiplying charge-coupled devices (EMCCDs) complement these detectors by offering a large number of spatially resolved pixels, but their frame rates are not high enough for direct time-resolved coincidence counting [258], [259]. To overcome this, several post-processing techniques have been developed to extract biphoton coincidences from sequences of EMCCD frames [193], [258]. These approaches, however, typically require on the order of 2×10^6 frames to form a single coincidence image. With typical exposure times, such data sets correspond to acquisition times that can exceed 17 h for one image [260].

The long acquisition time is therefore a major bottleneck for wide-field quantum imaging. This is particularly unfortunate because quantum imaging offers several important advantages over its classical counterpart: resilience to stray light [244], [260], enhanced sensitivity in two-photon processes [261], [262], and the possibility of resolution enhancement through quantum correlations [263]–[265]. Nonetheless, until recently there had been no demonstration of EMCCD-based wide-field quantum imaging achieving $\sim$1.4 μm resolution, largely because low-intensity quantum sources and slow coincidence extraction limit the achievable CNR and speed.

Quantum estimation theory predicts that an N-photon entangled state can, in principle, enhance resolution by a factor of N with respect to classical light, corresponding to the Heisenberg limit [241], [264]. In particular, biphoton NOON states have been used to demonstrate a twofold improvement in spatial resolution in quantum lithography [247], and SPDC-generated biphoton states can also reach the Heisenberg limit in certain imaging configurations [264], [265]. In both of these settings, the two photons propagate along the same physical path, effectively acting as a single excitation with half the wavelength [264], [265]. More recently, it has been shown that Heisenberg-limited resolution can be attained even when only one photon in each pair interacts with the sample, provided that the detection scheme appropriately exploits the biphoton correlations [258], [263].

Building on the wide-field approach of Refs. [193], [258], we implement QMC using an EMCCD camera in a configuration where the two arms have balanced optical pathlengths. Earlier realizations of similar concepts were not yet suitable for microscopic imaging. In particular, they typically used low numerical apertures (NAs) and large fields of view, limiting the achievable resolution, and they relied on post-processing algorithms that required large frame counts, limiting the speed. Here, by introducing high-NA objectives and a more efficient covariance-based coincidence extraction algorithm, we improve both the spatial resolution and the acquisition rate.

The QMC scheme leverages the quantum correlations of biphotons to perform super-resolved microscopy, achieving up to five-fold higher imaging speed, 2.6-fold higher CNR, and approximately ten-fold stronger robustness to stray light relative to previous wide-field quantum imaging techniques [193], [260]. In contrast to quantum imaging protocols that operate at the standard quantum limit [247], [259], [263], the balanced-pathlength configuration realizes a factor-of-two resolution gain, characteristic of the Heisenberg limit [258], [264]. Using this framework, we demonstrate wide-field imaging of cancer cells with a spatial resolution of 1.4 μm over a FOV of 100×50 μm^2. The combination of low-light illumination, super-resolution, enhanced CNR, and strong rejection of uncorrelated background makes QMC a promising tool for biological imaging.

8.2 Experimental setup

A schematic of the QMC optical system is shown in Fig. 8.1. A right-angle prism first separates the signal and idler photons into two nominally symmetric arms. The optical pathlengths in these arms are carefully adjusted to be equal (see Section 8.6 for further discussion). The arm that contains the sample functions as a conventional wide-field imaging path; the image obtained from this arm alone, without coincidence processing, is used as the classical reference.

Although QMC builds on the same general physical principles as earlier wide-field biphoton imaging schemes [193], [258], [260], the implementation here is significantly different. In previous work, the two arms typically shared a common imaging system with small NA and a large FOV, which limited the spatial resolution to macroscopic scales. In the present configuration, the biphoton field is split at the source Fourier plane using a prism, and the signal and idler paths are then relayed independently. This architecture allows high-NA microscope objectives to be inserted in both arms, enabling microscopic spatial resolution.

The signal and idler arms are constructed as near mirror images of one another, ensuring that the optical pathlengths, magnification, and aberrations are well matched. SPDC photon pairs are generated in a type-I BBO crystal pumped by a continuous-wave laser, spectrally filtered, and relayed by a series of $4f$ systems to the object and reference planes. The fields from both arms are finally imaged onto an EMCCD camera, which records the spatially resolved single-photon intensities.

8.3 Estimation of coincidence intensity and covariance algorithm

To efficiently recover coincidence information from EMCCD data, we employ a covariance-based algorithm that estimates the coincidence intensity between the signal and idler regions of the camera. As illustrated schematically in Fig. 8.2, the

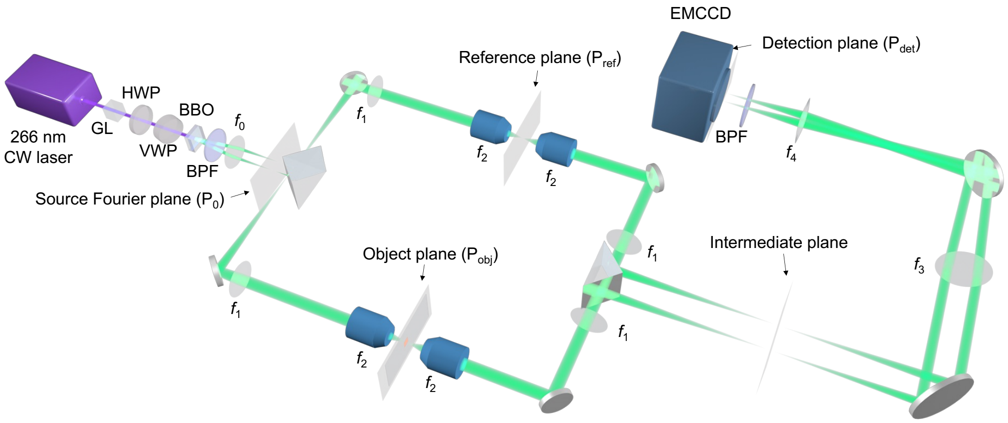

Figure 8.1: **Experimental setup schematic of QMC.** A continuous-wave 266 nm laser pumps a type-I BBO crystal to generate entangled photon pairs via SPDC. A Glan–Laser polarizer (GL), half-wave plate (HWP), and variable wave plate (VWP) adjust the pump polarization. A 532 nm bandpass filter (BPF) removes the pump. The signal and idler photons are separated by a right-angle prism and relayed through symmetric $4f$ systems (lenses with focal lengths f_0–f_4) to the object plane (P_{obj}), reference plane (P_{ref}), and detection plane (P_{det}) on an EMCCD camera. The source Fourier plane P_0 corresponds to the Fourier plane of the BBO crystal.

EMCCD sensor is partitioned into a left (L) region that collects signal photons and a right (R) region that records idler photons.

Let I_L and I_R denote the total intensities recorded in the left and right regions, respectively, in a single frame. Each can be decomposed into a contribution from true biphoton coincidences and a contribution from noise,

$$I_L = I_{\text{coin}} + I_{L,\text{noise}}, \tag{8.1}$$

$$I_R = I_{\text{coin}} + I_{R,\text{noise}}, \tag{8.2}$$

where I_{coin} represents the coincidence intensity from entangled pairs, and $I_{L,\text{noise}}$ and $I_{R,\text{noise}}$ account for detector noise, dark counts, and other uncorrelated background. These noise terms are assumed to be statistically independent between the two regions.

Over N frames, the covariance between I_L and I_R is defined as

$$\operatorname{cov}(I_L, I_R) = \frac{1}{N}\sum_{i=1}^{N}\big(I_L^{(i)} - \langle I_L\rangle\big)\big(I_R^{(i)} - \langle I_R\rangle\big), \tag{8.3}$$

where $I_L^{(i)}$ and $I_R^{(i)}$ are the intensities in frame i, and $\langle\cdot\rangle$ denotes an average over frames. Substituting Eqs. (8.1) and (8.2) into Eq. (8.3), one obtains

$$\mathrm{cov}(I_L, I_R) = \langle I_{\mathrm{coin}}^2\rangle - \langle I_{\mathrm{coin}}\rangle^2 + \langle I_{L,\mathrm{noise}} I_{R,\mathrm{noise}}\rangle - \langle I_{L,\mathrm{noise}}\rangle\langle I_{R,\mathrm{noise}}\rangle. \tag{8.4}$$

Because the noise in the two regions arises from independent processes, the cross term involving $I_{L,\mathrm{noise}}$ and $I_{R,\mathrm{noise}}$ is negligible in practice, i.e.,

$$\langle I_{L,\mathrm{noise}} I_{R,\mathrm{noise}}\rangle - \langle I_{L,\mathrm{noise}}\rangle\langle I_{R,\mathrm{noise}}\rangle \ll \langle I_{\mathrm{coin}}^2\rangle - \langle I_{\mathrm{coin}}\rangle^2.$$

The coincidence signal I_{coin} follows Poissonian statistics [252], [266], such that its variance equals its mean. Under this condition,

$$\mathrm{cov}(I_L, I_R) \approx \langle I_{\mathrm{coin}}^2\rangle - \langle I_{\mathrm{coin}}\rangle^2 = \langle I_{\mathrm{coin}}\rangle. \tag{8.5}$$

Thus, for sufficiently large N, the covariance between the left and right regions directly estimates the average coincidence intensity. This is a key difference from earlier EMCCD-based methods [193], [258], [260], which do not yield the expected coincidence intensity as directly.

Figure 8.2b illustrates how the CNR evolves with the number of frames for QMC in comparison with two representative wide-field quantum imaging methods [193], [260]. To reach a CNR of 3, the covariance-based algorithm requires approximately 10^5 frames (with 10 ms exposure per frame), corresponding to about 40% and 20% of the frame counts needed in Refs. [193] and [260], respectively. At a fixed large frame number (2×10^6), QMC achieves ~1.5-fold and ~2.6-fold higher CNR than these two methods.

One of the key benefits of quantum imaging is its robustness to stray light. Equation (8.5) highlights that the covariance isolates the correlated biphoton component and naturally suppresses uncorrelated contributions, including stray-light background. When more than 2×10^6 frames are available, the algorithms in Refs. [193], [260] can also tolerate significant stray-light levels, but their performance deteriorates for smaller data sets. Figure 8.2c shows the dependence of CNR on stray-light intensity when only 10^5 frames are used. Once the stray light is roughly 12 times stronger than the classical signal, the classical CNR falls below unity, and the earlier quantum algorithms likewise fail to maintain adequate contrast. In contrast, QMC maintains a CNR above one even when the stray-light intensity is ~120 times the classical signal for the same number of frames.

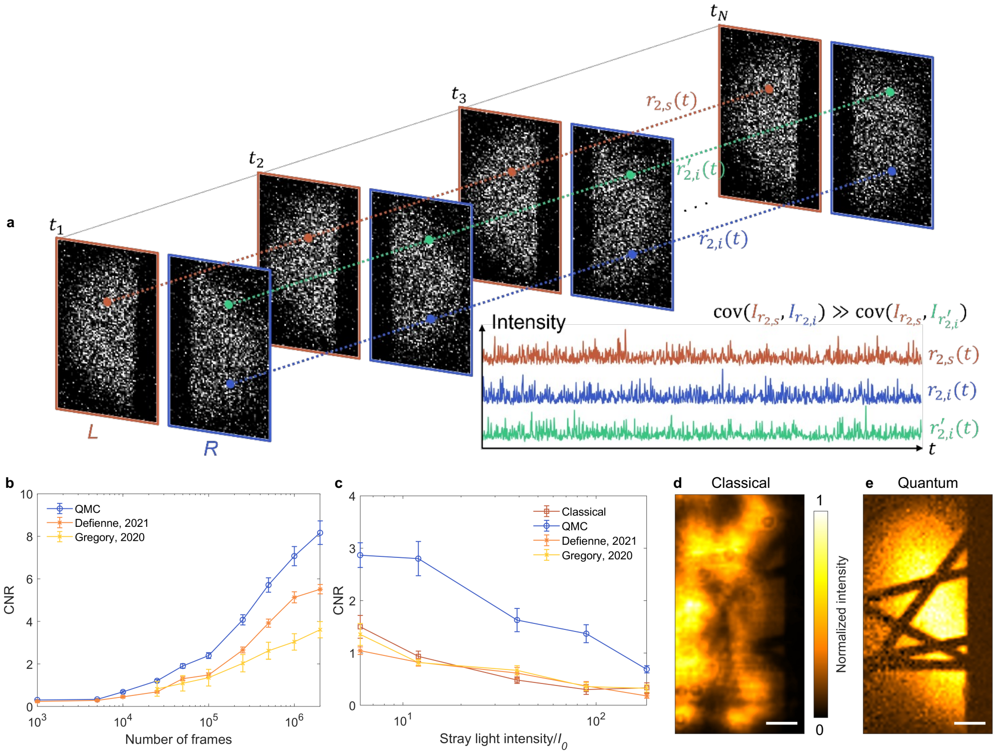

Figure 8.2: **Covariance-based coincidence measurement in QMC.** (a) Conceptual picture of the covariance method: symmetric pixel pairs in the left (L) and right (R) regions of the EMCCD are monitored over many frames. The covariance of their intensities is dominated by entangled biphoton events, whereas contributions from accidental or uncorrelated photons average out. (b) Comparison of CNR versus number of frames for QMC and existing wide-field quantum imaging algorithms [193], [260]. (c) CNR as a function of stray-light intensity using 10^5 frames, comparing classical imaging, QMC, and previous quantum algorithms. (d) Classical and (e) QMC images of carbon fibers in the presence of stray light with intensity $8I_0$, where I_0 is the classical signal intensity.

The qualitative difference is evident in Figs. 8.2d and e, which compare classical and QMC images of carbon fibers under stray light at $8I_0$. The classical image is heavily contaminated by stray light, whereas the QMC image effectively recovers the underlying structure by isolating the coincidence signal. When the full 2×10^6 frames are used, QMC continues to operate successfully even if the stray light reaches ~155 times the classical signal. The breakdown occurs only when accidental coincidences from the background approach the rate of true biphoton coincidences. Overall, the covariance method provides a powerful and efficient way to retrieve entangled-photon coincidences while strongly rejecting uncorrelated noise, thereby maximizing CNR at a given background level.

8.4 Quantification of spatial resolution

To quantify the spatial resolution enhancement provided by QMC, we first examine a simplified diagram of the imaging geometry, shown in Fig. 8.3a. Classical and quantum images of group 7 of a USAF 1951 resolution target, whose stripe widths range from 2.76 to 3.91 μm, are displayed in Figs. 8.3b and c, respectively. These features lie near the resolution limit of the classical imaging system used here.

The resolution is quantified via the full width at half maximum (FWHM) of the line-spread function (LSF) in the vicinity of focus. Figure 8.3d summarizes the measured spatial resolutions of classical imaging and QMC as functions of the axial position z relative to the classical focal plane. At the optimal focus, the classical system achieves a resolution of 2.9 μm, whereas QMC yields a resolution of 1.4 μm, demonstrating approximately a factor-of-two improvement. Normalized lateral LSFs at selected z positions are plotted in Fig. 8.3e, highlighting the narrower QMC response.

The factor-of-two resolution gain can be interpreted in terms of an effective wavelength that is halved for the biphoton relative to the single-photon case. To formalize this, consider the coordinates $r_{0,s}$, $r_{1,s}$, and $r_{2,s}$ in the source Fourier plane, object plane, and detection plane for the signal arm, and $r_{0,i}$, $r_{1,i}$, and $r_{2,i}$ for the idler arm, as indicated in Fig. 8.3a. The biphoton state at the source Fourier plane can be written as

$$|\xi\rangle = \sum_{k_{0,s}} A(k_{0,s}) e^{ik_{0,s}\cdot r_{0,s}} e^{ik_{0,i}\cdot r_{0,i}} |1_{k_{0,s}}, 1_{k_{0,i}}\rangle, \tag{8.6}$$

where $k_{0,s}$ and $k_{0,i}$ are the transverse wavevectors for the signal and idler photons, and $A(k_{0,s})$ is the probability amplitude of each jointly occupied mode. Denoting the pump position and wavevector by r_p and k_p, the SPDC phase-matching condition enforces spatial entanglement such that $(r_{0,s}+r_{0,i})/2 = r_p$ and $k_{0,s}+k_{0,i} = k_p$ [252].

For a given pair of symmetric pixels in the detection plane, the intensity correlation is described by the second-order correlation function

$$G^{(2)}_{\mathrm{QMC}} = \left|\langle 0|\hat{E}_s^{(+)}\hat{E}_i^{(+)}|\xi\rangle\right|^2, \tag{8.7}$$

where $\hat{E}_s^{(+)}$ and $\hat{E}_i^{(+)}$ are the positive-frequency field operators in the signal and idler arms. After propagation through the symmetric $4f$ relays and interaction with the object, the QMC image can be expressed as

$$G^{(2)}_{\mathrm{QMC}}(\boldsymbol{\rho}) = \left|t(\boldsymbol{\rho})\right|^2 \Gamma_{\mathrm{QMC}}\left(\frac{\lambda}{2};\boldsymbol{\rho}\right) \left|h\left(\frac{\lambda}{2};\boldsymbol{\rho}, M\boldsymbol{\rho}\right)\right|^2, \tag{8.8}$$

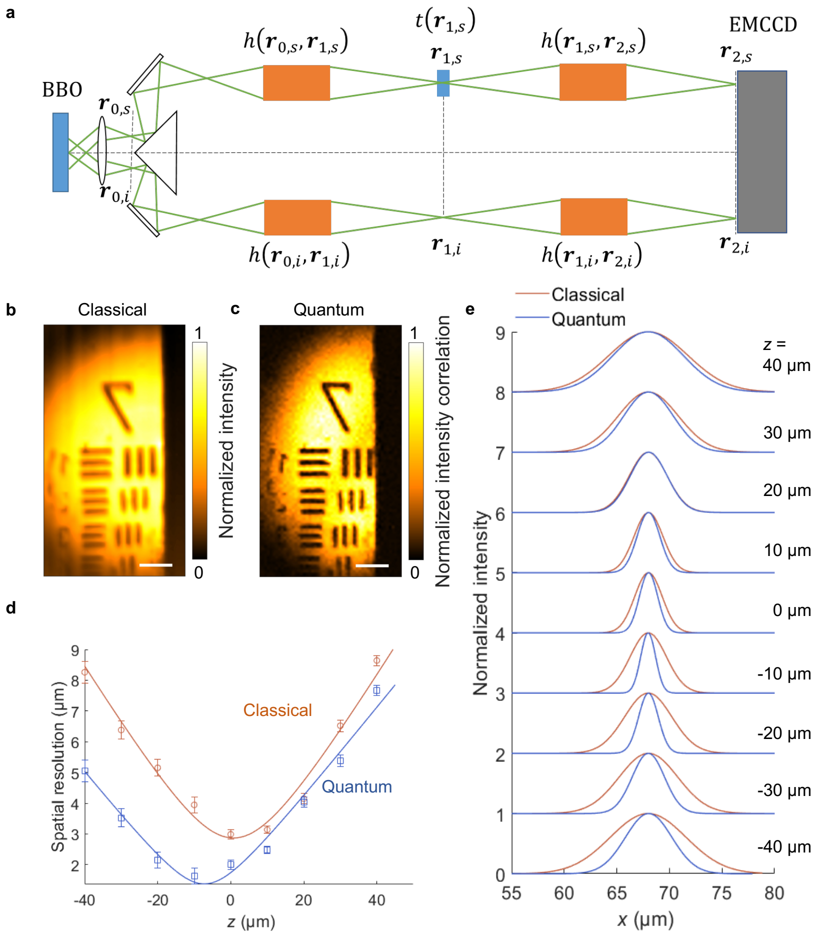

Figure 8.3: **Super-resolution performance of QMC.** (a) Simplified diagram of the QMC imaging geometry. The vectors r_0, r_1, and r_2 denote coordinates in the source Fourier plane, object plane, and detection plane, respectively, with subscripts s and i distinguishing the signal and idler arms. The functions $h(r_{0,s}, r_{1,s})$ and $h(r_{1,s}, r_{2,s})$ are the PSFs from $r_{0,s}$ to $r_{1,s}$ and from $r_{1,s}$ to $r_{2,s}$ in the signal arm; $h(r_{0,i}, r_{1,i})$ and $h(r_{1,i}, r_{2,i})$ are the corresponding PSFs in the idler arm. The object transmission is denoted by $t(r_{1,s})$. (b–c) Classical (b) and QMC (c) images of group 7 (2.76–3.91 μm) of a USAF 1951 resolution target. Scale bars: 20 μm. (d) Measured spatial resolution for classical imaging and QMC as a function of axial position z relative to the classical focal plane. Data points indicate means ± standard errors ($n = 14$). (e) Normalized lateral LSFs of classical imaging and QMC at different z positions.

where $\boldsymbol{\rho}$ denotes coordinates in the object plane, $t(\boldsymbol{\rho})$ is the object's amplitude transmission, $\Gamma_{\mathrm{QMC}}(\lambda/2;\boldsymbol{\rho})$ is the squared intensity distribution on the object plane corresponding to an effective wavelength $\lambda/2$, and $h(\lambda/2;\boldsymbol{\rho}, M\boldsymbol{\rho})$ is the PSF from the object plane to the detection plane at this effective wavelength and magnification M.

For comparison, the classical wide-field image formed with illumination at wavelength λ is characterized by the first-order correlation function

$$G_{\mathrm{CI}}^{(1)}(\boldsymbol{\rho}) = \left|t(\boldsymbol{\rho})\right|^2 \gamma_{\mathrm{CI}}(\lambda; \boldsymbol{\rho}) \left|h(\lambda; \boldsymbol{\rho}, M\boldsymbol{\rho})\right|^2 , \tag{8.9}$$

where $\gamma_{\mathrm{CI}}(\lambda; \boldsymbol{\rho})$ is the wide-field illumination intensity at the object plane and $h(\lambda; \boldsymbol{\rho}, M\boldsymbol{\rho})$ is the classical PSF at wavelength λ.

The difference between Eqs. (8.8) and (8.9) highlights that QMC effectively probes the object with an illumination at half the wavelength, even though each photon individually has wavelength λ. Importantly, in the present implementation, only the signal photon passes through the sample, while the idler photon does not interact with the object [247], [264]. The resulting “two-photon PSF” arises from coherent interference between the signal and idler fields in the coincidence channel, not simply from multiplying classical intensity PSFs. A simplified description of this phenomenon has been proposed for twin-photon imaging [267], but the full treatment must account for the specific geometry and illumination conditions of the QMC system.

In the experiments, the classical resolution is ultimately limited by the effective NA of the microscope objectives. The actual NA can be smaller than the nominal value (0.4 in this case) if the beam does not fully fill the entrance pupil, which further increases the relative advantage of the QMC resolution.

8.5 Imaging cells by QMC

To illustrate the capabilities of QMC for biological imaging, we apply the method to fixed cancer cells. Figures 8.4a and b present classical and QMC images, respectively, of two HeLa cells. Line profiles taken along the arrows in these images are plotted in Fig. 8.4c. The QMC profiles reveal subcellular structures and boundaries that appear blurred or unresolved in the classical image, consistent with the measured factor-of-two improvement in spatial resolution.

Some irregularities in the brightness distribution are visible in both the classical and QMC images. These variations are attributed to the sample preparation (for example, non-uniform staining or thickness) rather than to fundamental limitations of the imaging system. The images in Fig. 8.4 were computed from 2×10^6 frames with a 10 ms exposure time per frame to obtain high CNR. Additional cell images reconstructed from 10^5 frames show qualitatively similar morphological details at lower acquisition times.

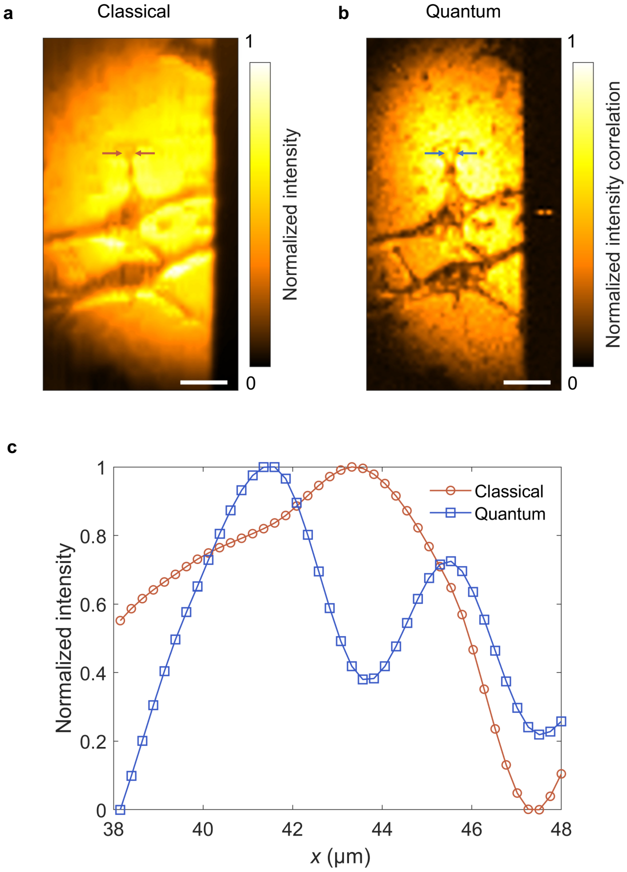

Figure 8.4: **QMC imaging of cancer cells.** (a–b) Classical (a) and QMC (b) images of two HeLa cells. Scale bars: 20 μm. (c) Normalized intensity profiles extracted along the arrows in (a) and (b), comparing the classical and QMC signals. The QMC traces show enhanced contrast and sharper transitions at cellular boundaries.

8.6 Discussion

The balanced-pathlength design is central to achieving Heisenberg-limited resolution in QMC. By making the optical paths from the source Fourier plane to the detection plane symmetric in the signal and idler arms, the photon pairs retain strong correlations in both position and momentum, which allows their phases to interfere constructively in the coincidence channel. For classical, unentangled light, such simultaneous correlations in position and momentum cannot be realized for independent photons, consistent with the uncertainty principle [268].

As a consequence of this symmetry, entangled photon pairs appear at conjugate positions about a common center in the source Fourier plane, the object plane, and the detection plane. In the experiment, the signal and idler arms are constructed as approximate mirror images of each other to preserve this symmetry. Photon pairs that originate at symmetric points in the source Fourier plane propagate along symmetric trajectories, enforced by the SPDC phase-matching conditions, and are then relayed by matched $4f$ systems to the object and reference planes.

When the signal photon encounters the sample at the object plane, scattering can alter its outgoing direction, leading to different wavevectors for the signal and idler photons thereafter. Nevertheless, within the paraxial approximation, rays that originate from the same point in the object plane are re-imaged to the same point in the detection plane, implying equal optical pathlengths according to Fermat's principle. Although scattering might at first seem to spoil the path symmetry, the fact that the object and detection planes are conjugate ensures that paired photons continue to experience balanced optical paths. This balanced-pathlength picture remains a good description of biphoton propagation from the source Fourier plane to the detection plane and underpins the observed Heisenberg-limited resolution.

In this chapter the emphasis is on establishing QMC as a practical tool for quantum bioimaging, rather than on competing directly with the highest-performance classical microscopes in terms of CNR or acquisition time. The primary limitation on CNR at present is the relatively low SPDC conversion efficiency of the BBO crystal. To reach a CNR of 3, QMC requires approximately 10^5 frames and a total acquisition time on the order of 17 min, whereas conventional fluorescence or bright-field microscopy can often produce sufficient CNR in a single sub-second exposure.

These constraints are not fundamental. More efficient quantum light sources, such as those enabled by nanophotonic structures or metalens arrays [269], could substantially increase the detected biphoton flux and dramatically reduce acquisition times. In addition, QMC offers a different mode of background rejection compared with classical nonlinear microscopies such as second-harmonic generation (SHG) imaging [270]. Whereas SHG relies primarily on spectral filtering to distinguish signal from background, QMC uses coincidence detection to reject both temporally and spatially uncorrelated noise, including stray light and detector noise.

In summary, QMC realizes quantum microscopy of cancer cells at the Heisenberg limit, with a demonstrated resolution of 1.4 μm, up to five-fold faster acquisition, 2.6-fold higher CNR, and an order-of-magnitude stronger resistance to stray light than previous wide-field quantum imaging schemes [193], [260]. The low illumination levels and quantum correlations make QMC an attractive candidate for nondestructive imaging of biological samples, revealing features that are not discernible in classical wide-field images. Classical imaging can be further improved by various super-resolution strategies [271], [272], and the QMC architecture presented here can, in principle, be combined with such approaches to effectively reduce the working wavelength by another factor of two, pushing classical super-resolution techniques into a genuinely quantum-enhanced regime.

Chapter 9

CONCLUSIONS AND OUTLOOK

This thesis presents a unified body of work advancing two frontiers of optical imaging: photoacoustic computed tomography and quantum imaging. Although these fields differ in physical mechanisms, technological infrastructures, and clinical maturity, the research described here pursues a shared objective: to push the limits of resolution, contrast, and biological interpretability in biomedical imaging.

In PACT, this thesis discusses two high-speed three-dimensional imaging frameworks that were deployed across multiple anatomical systems—rodent brain, rodent heart, and the human breast—to demonstrate capabilities not previously achieved in conventional PACT. For the breast-imaging studies, systematic pipelines were constructed for data processing, reconstruction, segmentation, and feature extraction. These pipelines allowed quantitative comparisons across patient populations and supported the development of classical and learning-based classifiers for assessing lesion characteristics. Collectively, these contributions demonstrate that PACT can move beyond qualitative visualization toward quantitative biomedical assessment, improving diagnostic performance while preserving the method's noninvasive and radiation-free nature.

In quantum imaging, this thesis introduces and demonstrates widefield and scanning-based quantum microscopy platforms that achieve super-resolution performance enabled by entangled-photon correlations. Novel imaging configurations and covariance-based detection algorithms were designed to surpass the classical shot-noise and diffraction limits. These developments yielded substantial gains in spatial resolution, contrast robustness, and stray-light suppression compared with classical imaging counterparts. The results highlight that entangled-photon-based imaging can access regimes previously regarded as impractical for real-world biological samples, and they establish a technological foundation for quantum-enhanced microscopy with relevance to cell biology, tissue photonics, and precision metrology.

Taken together, the research presented here advances both PACT and quantum imaging along crucial axes: system design and engineering, image reconstruction and processing, feature extraction, and translational deployment. The overall body of work demonstrates how physical insight, optical engineering, and data-driven analysis can be jointly leveraged to expand the boundaries of noninvasive biomedical imaging.

The results in this thesis open several pathways for future investigation, both in PACT and in quantum imaging. The next phase of PACT development will focus on deriving richer diagnostic information from increasingly complex datasets. One promising direction is the incorporation of hypoxia-based biomarkers, which have shown preliminary value in highlighting metabolic and vascular abnormalities in breast tissue. By quantifying spectral and temporal signatures related to tumor oxygenation and perfusion dynamics, PACT may offer new functional contrasts that complement morphology-based assessments. Another major opportunity lies in multimodal integration. Breast imaging inherently benefits from the complementary information provided by mammography, ultrasound, and MRI. By aligning PACT data with these modalities—and by leveraging large vision or language models to interpret heterogeneous datasets—PACT can be embedded into a broader clinical context. Such integration may enable improved diagnostic decision-making, enhanced lesion characterization, and patient-specific longitudinal tracking. Ultimately, the goal is to position PACT as a clinically mature modality whose value arises both from its intrinsic imaging capabilities and from its synergy with the broader ecosystem of breast diagnostics.

The central challenge for real-world quantum imaging is acquisition speed. While coincidence-based methods have demonstrated exceptional resolution and robustness, their frame rates remain fundamentally limited by detection efficiency, photon flux, and system noise. Overcoming this bottleneck will require advances in high-efficiency, low-noise detection hardware; optimized optical architectures for photon-pair generation and collection; and improved algorithms for coincidence extraction and quantum-state reconstruction. Ongoing research will investigate advanced detector arrays, such as superconducting-nanowire single-photon detector arrays, to achieve real-time coincidence imaging. If combined with high-brightness entangled sources and improved optical throughput, these advances could elevate the frame rate of quantum microscopy to levels enabling applications in living systems.

PACT and quantum imaging—though grounded in distinct physical principles—are converging toward a shared vision: achieving high-resolution, high-contrast, and functionally informative imaging in regimes where conventional optical imaging falls short. Continued progress in detection technologies, photonic engineering, and data-driven analysis is expected to further accelerate both fields. These advancements hint at a future in which noninvasive, high-performance imaging becomes a ubiquitous tool in biology and medicine, enabling unprecedented insights into complex living systems.

BIBLIOGRAPHY

[1] L. V. Wang and S. Hu, “Photoacoustic tomography: In vivo imaging from organelles to organs,” *Science*, vol. 335, pp. 1458–1462, 2012. DOI: `10.1126/science.1216210`.

[2] L. V. Wang and J. Yao, “A practical guide to photoacoustic tomography in the life sciences,” *Nature Methods*, vol. 13, pp. 627–638, 2016. DOI: `10.1038/nmeth.3925`.

[3] L. Lin and L. V. Wang, “The emerging role of photoacoustic imaging in clinical oncology,” *Nature Reviews Clinical Oncology*, vol. 19, pp. 365–383, 2022. DOI: `10.1038/s41571-022-00615-3`.

[4] J. Park, S. Choi, F. Knieling, B. Clingman, S. Bohndiek, L. V. Wang, and C. Kim, “Clinical translation of photoacoustic imaging,” *Nature Reviews Bioengineering*, vol. 3, pp. 193–212, 2025. DOI: `10.1038/s44222-024-00240-y`.

[5] E. I. Neuschler, R. Butler, C. A. Young, *et al.*, “A pivotal study of optoacoustic imaging to diagnose benign and malignant breast masses: A new evaluation tool for radiologists,” *Radiology*, vol. 287, pp. 398–412, 2017. DOI: `10.1148/radiol.2017161513`.

[6] H.-P. Brecht *et al.*, “Whole-body three-dimensional optoacoustic tomography system for small animals,” *Journal of Biomedical Optics*, vol. 14, no. 6, p. 064 007, 2009.

[7] J. Xia, W. Chen, K. Maslov, M. A. Anastasio, and L. V. Wang, “Whole-body ring-shaped confocal photoacoustic computed tomography of small animals in vivo,” *Journal of Biomedical Optics*, vol. 17, p. 050 506, 2012. DOI: `10.1117/1.JBO.17.5.050506`.

[8] L. Li, L. Zhu, C. Ma, L. Wang, J. Yao, and L. V. Wang, “Single-impulse panoramic photoacoustic computed tomography of small-animal whole-body dynamics at high spatiotemporal resolution,” *Nature Biomedical Engineering*, vol. 1, p. 0071, 2017. DOI: `10.1038/s41551-017-0071`.

[9] L. Lin, P. Hu, J. Shi, C. M. Appleton, K. Maslov, L. Li, R. Zhang, and L. V. Wang, “Single-breath-hold photoacoustic computed tomography of the breast,” *Nature Communications*, vol. 9, p. 2352, 2018. DOI: `10.1038/s41467-018-04734-5`.

[10] L. Lin, P. Hu, X. Tong, S. Na, R. Cao, X. Yuan, D. C. Garrett, J. Shi, K. Maslov, and L. V. Wang, “High-speed three-dimensional photoacoustic computed tomography for preclinical research and clinical translation,” *Nature Communications*, vol. 12, p. 882, 2021. DOI: `10.1038/s41467-021-21232-1`.

[11] B. E. Treeby and B. T. Cox, "K-Wave: MATLAB toolbox for the simulation and reconstruction of photoacoustic wave fields," *Journal of Biomedical Optics*, vol. 15, p. 021 314, 2010. DOI: `10.1117/1.3360308`.

[12] N. Davoudi, X. L. Deán-Ben, and D. Razansky, "Deep learning optoacoustic tomography with sparse data," *Nature Machine Intelligence*, vol. 1, pp. 453–460, 2019. DOI: `10.1038/s42256-019-0107-0`.

[13] J. Yang, S. Choi, and C. Kim, "Recent advances in deep-learning-enhanced photoacoustic imaging," *Advanced Photonics Nexus*, vol. 2, p. 054 001, 2023. DOI: `10.1117/1.APN.2.5.054001`.

[14] J. Yao, J. Xia, and L. V. Wang, "Multiscale functional and molecular photoacoustic tomography," *Ultrasonic Imaging*, vol. 38, pp. 44–62, 2016. DOI: `10.1177/0161734615599760`.

[15] G. Diot, S. Metz, A. Noske, *et al.*, "Multispectral optoacoustic tomography (MSOT) of human breast cancer," *Clinical Cancer Research*, vol. 23, pp. 6912–6922, 2017. DOI: `10.1158/1078-0432.CCR-17-0896`.

[16] S. Manohar and M. Dantuma, "Current and future trends in photoacoustic breast imaging," *Photoacoustics*, vol. 16, p. 100 134, 2019. DOI: `10.1016/j.pacs.2019.100134`.

[17] L. Lin *et al.*, "Photoacoustic computed tomography of breast cancer in response to neoadjuvant chemotherapy," *Advanced Science*, vol. 8, p. 2 003 396, 2021. DOI: `10.1002/advs.202003396`.

[18] K. Nagae *et al.*, "Real-time 3d photoacoustic visualization system with a wide field of view for imaging human limbs," *F1000Research*, vol. 7, p. 1813, 2018. DOI: `10.12688/f1000research.16565.1`.

[19] J. Ahn, J. Y. Kim, W. Choi, and C. Kim, "High-resolution functional photoacoustic monitoring of vascular dynamics in human fingers," *Photoacoustics*, vol. 23, p. 100 282, 2021. DOI: `10.1016/j.pacs.2021.100282`.

[20] Y. Suzuki *et al.*, "Subcutaneous lymphatic vessels in the lower extremities: Comparison between photoacoustic lymphangiography and near-infrared fluorescence lymphangiography," *Radiology*, vol. 295, pp. 469–474, 2020. DOI: `10.1148/radiol.2020191499`.

[21] F. Knieling *et al.*, "Multispectral optoacoustic tomography in ulcerative colitis — a first-in-human diagnostic clinical trial," *Journal of Nuclear Medicine*, vol. 58, p. 1196, 2017. DOI: `10.2967/jnumed.117.192211`.

[22] A. P. Regensburger *et al.*, "Multispectral optoacoustic tomography enables assessment of disease activity in paediatric inflammatory bowel disease," *Photoacoustics*, vol. 35, p. 100 578, 2024. DOI: `10.1016/j.pacs.2023.100578`.

[23] B. Park, C. Kim, and J. Kim, “Recent advances in ultrasound and photoacoustic analysis for thyroid cancer diagnosis,” *Advanced Physics Research*, vol. 2, p. 2 200 070, 2023. DOI: `10.1002/apxr.202200070`.

[24] M. V. Marshall *et al.*, “Near-infrared fluorescence imaging in humans with indocyanine green: A review and update,” *The Open Surgical Oncology Journal*, vol. 2, pp. 12–25, 2010.

[25] H. Rahbar, S. C. Partridge, W. B. DeMartini, B. Thursten, and C. D. Lehman, “Clinical and technical considerations for high quality breast mri at 3 tesla,” *Journal of Magnetic Resonance Imaging*, vol. 37, no. 4, pp. 778–790, 2013.

[26] D. A. Feinberg and E. Yacoub, “The rapid development of high speed, resolution and precision in fmri,” *NeuroImage*, vol. 62, no. 2, pp. 720–725, 2012.

[27] S. Gottschalk *et al.*, “Rapid volumetric optoacoustic imaging of neural dynamics across the mouse brain,” *Nature Biomedical Engineering*, vol. 3, pp. 392–401, 2019.

[28] X. L. Deán-Ben, T. F. Fehm, S. J. Ford, S. Gottschalk, and D. Razansky, “Spiral volumetric optoacoustic tomography visualizes multi-scale dynamics in mice,” *Light: Science & Applications*, vol. 6, e16247, 2017.

[29] Y. Matsumoto *et al.*, “Visualising peripheral arterioles and venules through high-resolution and large-area photoacoustic imaging,” *Scientific Reports*, vol. 8, p. 14 930, 2018.

[30] A. Oraevsky *et al.*, “Full-view 3d imaging system for functional and anatomical screening of the breast,” in *Proc. SPIE 10494, Photons Plus Ultrasound: Imaging and Sensing*, 2018.

[31] S. M. Schoustra *et al.*, “Twente photoacoustic mammoscope 2: System overview and three-dimensional vascular network images in healthy breasts,” *Journal of Biomedical Optics*, vol. 24, no. 12, p. 121 909, 2019.

[32] R. A. Kruger *et al.*, “Dedicated 3d photoacoustic breast imaging,” *Medical Physics*, vol. 40, no. 11, p. 113 301, 2013.

[33] X. L. Deán-Ben and D. Razansky, “Functional optoacoustic human angiography with handheld video rate three dimensional scanner,” *Photoacoustics*, vol. 1, no. 3–4, pp. 68–73, 2013.

[34] M. Heijblom, W. Steenbergen, and S. Manohar, “Clinical photoacoustic breast imaging: The twente experience,” *IEEE Pulse*, vol. 6, no. 3, pp. 42–46, 2015.

[35] Y. Tan, K. Xia, Q. Ren, and C. Li, “Three-dimensional photoacoustic imaging via scanning a one dimensional linear unfocused ultrasound array,” *Optics Express*, vol. 25, no. 7, pp. 8022–8028, 2017.

[36] M. Xu and L. V. Wang, “Universal back-projection algorithm for photoacoustic computed tomography,” *Physical Review E*, vol. 71, no. 1, p. 016 706, 2005.

[37] X. Pan, Y. Zou, and M. A. Anastasio, “Data redundancy and reduced-scan reconstruction in reflectivity tomography,” *IEEE Transactions on Image Processing*, vol. 12, no. 7, pp. 784–795, 2003.

[38] P. Hu, L. Li, L. Lin, and L. V. Wang, “Spatiotemporal antialiasing in photoacoustic computed tomography,” *IEEE Transactions on Medical Imaging*, vol. 39, no. 11, pp. 3535–3547, 2020.

[39] S. L. Jacques, *Generic tissue optical properties*, `https://omlc.org/news/feb15/generic_optics/index.html`, 2015.

[40] American National Standards Institute, *American national standard for the safe use of lasers, ansi z136.1-2007*, 2007.

[41] L. Lei *et al.*, “Label-free photoacoustic computed tomography of whole mouse brain structures ex vivo,” *Neurophotonics*, vol. 3, no. 3, p. 035 001, 2016.

[42] A. Greenough and A. D. Miller, *Manual of Neonatal Respiratory Care*, 2nd ed. Taylor & Francis, 2006.

[43] D. A. Schwinn, R. W. McIntyre, and J. G. Reves, “Isoflurane-induced vasodilation: Role of the alpha-adrenergic nervous system,” *Anesthesia & Analgesia*, vol. 71, no. 4, pp. 451–459, 1990.

[44] R. Cao *et al.*, “Functional and oxygen-metabolic photoacoustic microscopy of the awake mouse brain,” *NeuroImage*, vol. 150, pp. 77–87, 2017.

[45] D. G. Lyons, A. Parpaleix, M. Roche, and S. Charpak, “Mapping oxygen concentration in the awake mouse brain,” *eLife*, vol. 5, e12024, 2016.

[46] E. Jonckers, J. V. Audekerke, G. D. Visscher, A. V. der Linden, and M. Verhoye, “Functional connectivity fmri of the rodent brain: Comparison of functional connectivity networks in rat and mouse,” *PLoS ONE*, vol. 6, no. 4, e18876, 2011.

[47] C. P. Hunter, “Epidemiology, stage at diagnosis, and tumor biology of breast carcinoma in multiracial and multiethnic populations,” *Cancer*, vol. 88, no. 5, pp. 1193–1202, 2000.

[48] N. Klauber-DeMore, “Tumor biology of breast cancer in young women,” *Breast Disease*, vol. 23, pp. 9–15, 2006.

[49] M. Herranz and A. Ruibal, “Optical imaging in breast cancer diagnosis: The next evolution,” *Journal of Oncology*, vol. 2012, p. 863 747, 2012.

[50] S. Rankin, “Recent advances in imaging breast cancer,” *Cancer Imaging*, vol. 2, no. 1, pp. 28–32, 2001.

[51] T. Durduran, R. Choe, J. Culver, L. Zubkov, M. Holboke, J. Giammarco, B. Chance, and A. Yodh, "Bulk optical properties of healthy female breast tissue," *Physics in Medicine and Biology*, vol. 47, pp. 2847–2861, 2002.

[52] D. Grosenick, H. Rinneberg, R. Cubeddu, and P. Taroni, "Review of optical breast imaging and spectroscopy," *Journal of Biomedical Optics*, vol. 21, no. 9, p. 091 311, 2016.

[53] M. A. Senchukova, N. V. Nikitenko, O. N. Tomchuk, N. V. Zaitsev, and A. A. Stadnikov, "Different types of tumor vessels in breast cancer: Morphology and clinical value," *SpringerPlus*, vol. 4, p. 512, 2015.

[54] S. Ueda *et al.*, "Baseline tumor oxygen saturation correlates with a pathologic complete response in breast cancer patients undergoing neoadjuvant chemotherapy," *Cancer Research*, vol. 72, no. 18, pp. 4318–4328, 2012.

[55] N. Weidner, J. P. Semple, W. R. Welch, and J. Folkman, "Tumor angiogenesis and metastasis—correlation in invasive breast carcinoma," *New England Journal of Medicine*, vol. 324, no. 1, pp. 1–8, 1991.

[56] 3D4Medical, *Complete anatomy 2020*, `https://3d4medical.com/`, 2020.

[57] R. A. Jesinger, G. E. L. Jr, E. A. Ballard, S. M. Zelasko, and L. M. Glassman, "Vascular abnormalities of the breast: Arterial and venous disorders, vascular masses, and mimic lesions with radiologic-pathologic correlation," *RadioGraphics*, vol. 31, no. 7, E117–E136, 2011.

[58] L. Lei, "Multi-contrast photoacoustic computed tomography," Ph.D. dissertation, California Institute of Technology, 2019.

[59] World Health Organization, *The top 10 causes of death*, `https://www.who.int/news-room/fact-sheets/detail/the-top-10-causes-of-death`, Accessed 2024-06-01, 2020.

[60] I. J. Neeland *et al.*, "Effects of liraglutide on visceral and ectopic fat in adults with overweight and obesity at high cardiovascular risk: A randomised, double-blind, placebo-controlled, clinical trial," *The Lancet Diabetes & Endocrinology*, vol. 9, pp. 595–605, 2021.

[61] F. Lobelo *et al.*, "Routine assessment and promotion of physical activity in healthcare settings: A scientific statement from the American Heart Association," *Circulation*, vol. 137, e495–e522, 2018.

[62] P. Fei *et al.*, "Cardiac light-sheet fluorescent microscopy for multi-scale and rapid imaging of architecture and function," *Scientific Reports*, vol. 6, p. 22 489, 2016.

[63] V. Chetboul, "Advanced techniques in echocardiography in small animals," *Veterinary Clinics of North America: Small Animal Practice*, vol. 40, pp. 529–543, 2010.

[64] M. Nahrendorf *et al.*, “Cardiac magnetic resonance imaging in small animal models of human heart failure,” *Medical Image Analysis*, vol. 7, pp. 369–375, 2003.

[65] G. Bertolini and L. Angeloni, “Vascular and cardiac CT in small animals,” in *Computed Tomography: Advanced Applications*, A. M. Halefoğlu, Ed., IntechOpen, 2017.

[66] Q. Wang *et al.*, “Application of animal and human PET in cardiac research,” *American Journal of Cardiovascular Disease*, vol. 8, pp. 24–30, 2018.

[67] R. Golestani *et al.*, “Small-animal SPECT and SPECT/CT: Application in cardiovascular research,” *European Journal of Nuclear Medicine and Molecular Imaging*, vol. 37, pp. 1766–1777, 2010.

[68] W. Koba, L. A. Jelicks, and E. J. Fine, “MicroPET/SPECT/CT imaging of small animal models of disease,” *American Journal of Pathology*, vol. 182, pp. 319–324, 2013.

[69] C. Nanni and D. A. Torigian, “Applications of small animal imaging with PET, PET/CT, and PET/MR imaging,” *PET Clinics*, vol. 3, pp. 243–250, 2008.

[70] E. W. Izaguirre *et al.*, “Dual modality micro-SPECT and micro-CT for small animal imaging: Technical advances and challenges,” in *Proceedings of SPIE 5923, Penetrating Radiation Systems and Applications VII*, 2005.

[71] R. M. Botnar and M. R. Makowski, “Cardiovascular magnetic resonance imaging in small animals,” *Progress in Molecular Biology and Translational Science*, vol. 105, pp. 227–261, 2012.

[72] C. Errico, J. Pierre, S. Pezet, Y. Desailly, Z. Lenkei, O. Couture, and M. Tanter, “Ultrafast ultrasound localization microscopy for deep super-resolution vascular imaging,” *Nature*, vol. 527, no. 7579, pp. 499–502, 2015.

[73] X. L. Deán-Ben *et al.*, “Spiral volumetric optoacoustic tomography visualizes multi-scale dynamics in mice,” *Light: Science & Applications*, vol. 6, e16247, 2017.

[74] I. Ivankovic *et al.*, “Volumetric optoacoustic tomography enables non-invasive *in vivo* characterization of impaired heart function in hypoxic conditions,” *Scientific Reports*, vol. 9, p. 8369, 2019.

[75] B. Desjardins and E. A. Kazerooni, “Ecg-gated cardiac ct,” *American Journal of Roentgenology*, vol. 182, pp. 993–1010, 2004.

[76] M. S. Nacif *et al.*, “Cardiac magnetic resonance imaging and its electrocardiographs (ecg): Tips and tricks,” *International Journal of Cardiovascular Imaging*, vol. 28, pp. 1465–1475, 2012.

[77] M. L. Lassen, J. Kwiecinski, and P. J. Slomka, “Gating approaches in cardiac PET imaging,” *PET Clinics*, vol. 14, pp. 271–279, 2019.

[78] H. C. A. Lin *et al.*, “Ultrafast volumetric optoacoustic imaging of whole isolated beating mouse heart,” *Scientific Reports*, vol. 8, p. 14 132, 2018.

[79] Ç. Özsoy *et al.*, “Ultrafast four-dimensional imaging of cardiac mechanical wave propagation with sparse optoacoustic sensing,” *Proceedings of the National Academy of Sciences of the United States of America*, vol. 118, e2103979118, 2021.

[80] S. L. Jacques, “Optical properties of biological tissues: A review,” *Physics in Medicine and Biology*, vol. 58, R37–R61, 2013.

[81] L. Lin *et al.*, “*In vivo* photoacoustic tomography of myoglobin oxygen saturation,” *Journal of Biomedical Optics*, vol. 21, p. 061 002, 2015.

[82] U. B. Hendgen-Cotta, M. Kelm, and T. Rassaf, “Myoglobin functions in the heart,” *Free Radical Biology and Medicine*, vol. 73, pp. 252–259, 2014.

[83] T. Azar, J. Sharp, and D. Lawson, “Heart rates of male and female Sprague-Dawley and spontaneously hypertensive rats housed singly or in groups,” *Journal of the American Association for Laboratory Animal Science*, vol. 50, pp. 175–184, 2011.

[84] M. A. Alpert and M. W. Hashimi, “Obesity and the heart,” *The American Journal of the Medical Sciences*, vol. 306, pp. 117–123, 1993.

[85] G. P. Aurigemma, G. De Simone, and T. P. Fitzgibbons, “Cardiac remodeling in obesity,” *Circulation: Cardiovascular Imaging*, vol. 6, pp. 142–152, 2013.

[86] M. Xu and L. V. Wang, “Universal back-projection algorithm for photoacoustic computed tomography,” *Physical Review E*, vol. 71, p. 016 706, 2005.

[87] C. Pantaleone, “Optical absorption of hemoglobin in tissue,” in *Cancer Immunotherapy and Biological Cancer Treatments*, H. Arnouk, Ed., IntechOpen, 2019.

[88] J. Mayet and A. Hughes, “Cardiac and vascular pathophysiology in hypertension,” *Heart*, vol. 89, pp. 1104–1109, 2003.

[89] S. M. Artham *et al.*, “Obesity and hypertension, heart failure, and coronary heart disease–risk factor, paradox, and recommendations for weight loss,” *The Ochsner Journal*, vol. 9, pp. 124–132, 2009.

[90] S. K. Pal, M. J. Miller, N. Agarwal, S. M. Chang, M. C. Mac Gregor, E. Cohen, S. Cole, W. Dale, C. S. M. Diefenbach, and M. L. Disis, “Adapting clinical trial design for older cancer patients,” *Journal of Clinical Oncology*, vol. 37, pp. 834–842, 2019.

[91] F. Andre, N. Ismaila, N. L. Henry, M. R. Somerfield, R. C. Bast, W. Barlow, D. E. Collyar, M. E. Hammond, N. M. Kuderer, and M. C. Liu, “Use of biomarkers to guide decisions on adjuvant systemic therapy for women with early-stage invasive breast cancer,” *Journal of Clinical Oncology*, vol. 37, pp. 1956–1964, 2019.

[92] F. Cardoso, L. J. van’t Veer, J. Bogaerts, L. Slaets, G. Viale, S. Delaloge, J.-Y. Pierga, E. Brain, S. Causeret, and M. DeLorenzi, “70-gene signature as an aid to treatment decisions in early-stage breast cancer,” *New England Journal of Medicine*, vol. 375, pp. 717–729, 2016.

[93] S. Glück, F. De Snoo, J. Peeters, L. Stork-Sloots, and G. Somlo, “Molecular subtyping of early-stage breast cancer identifies a group of patients who do not benefit from adjuvant chemotherapy,” *Breast Cancer Research and Treatment*, vol. 139, pp. 759–767, 2013.

[94] M. Golshan, C. T. Cirrincione, W. M. Sikov, D. A. Berry, S. Jasinski, T. F. Weisberg, G. Somlo, C. Hudis, E. Winer, and D. W. Ollila, “Breast-conserving surgery after neoadjuvant chemotherapy for triple-negative breast cancer: Surgical results from CALGB 40603 (alliance),” *Annals of Surgery*, vol. 262, pp. 434–439, 2015.

[95] A. M. Chen, F. Meric-Bernstam, K. K. Hunt, H. D. Thames, M. J. Oswald, E. D. Outlaw, E. A. Strom, M. D. McNeese, H. M. Kuerer, and M. I. Ross, “Breast conservation after neoadjuvant chemotherapy: The M. D. anderson cancer center experience,” *Journal of Clinical Oncology*, vol. 22, pp. 2303–2312, 2004.

[96] C. Liedtke, C. Mazouni, K. R. Hess, F. André, A. Tordai, J. A. Mejia, W. F. Symmans, A. M. Gonzalez-Angulo, B. Hennessy, and M. Green, “Response to neoadjuvant therapy and long-term survival in patients with triple-negative breast cancer,” *Journal of Clinical Oncology*, vol. 26, pp. 1275–1281, 2008.

[97] N. E. Davidson and M. Morrow, “Neoadjuvant therapy for breast cancer,” *Journal of the National Cancer Institute*, vol. 97, pp. 159–161, 2005.

[98] P. Cortazar and P. G. Kluetz, “Pathological complete response in neoadjuvant treatment of breast cancer,” *Clinical Advances in Hematology & Oncology*, vol. 13, pp. 755–758, 2015.

[99] P. Cortazar, L. Zhang, M. Untch, K. Mehta, J. P. Costantino, N. Wolmark, H. Bonnefoi, D. Cameron, L. Gianni, and P. Valagussa, “Pathological complete response and long-term clinical benefit in breast cancer: The CTNeoBC pooled analysis,” *Lancet*, vol. 384, pp. 164–172, 2014.

[100] W. F. Symmans, C. Wei, R. Gould, X. Yu, Y. Zhang, M. Liu, A. Walls, A. Bousamra, M. Ramineni, and B. Sinn, “Long-term prognostic risk after neoadjuvant chemotherapy associated with residual cancer burden and breast

cancer subtype," *Journal of Clinical Oncology*, vol. 35, pp. 1049–1060, 2017.

[101] S. M. Wong, J. De Los Santos, and M. Basik, "Locoregional management of the axilla after neoadjuvant chemotherapy," *Current Breast Cancer Reports*, vol. 9, pp. 148–156, 2017.

[102] G. Cocconi, B. Di Blasio, G. Alberti, G. Bisagni, E. Botti, and G. Peracchia, "Problems in evaluating response of primary breast cancer to systemic therapy," *Breast Cancer Research and Treatment*, vol. 4, pp. 309–313, 1984.

[103] L. Kostakoglu, F. Duan, M. O. Idowu, P. R. Jolles, H. D. Bear, M. Muzi, J. Cormack, J. P. Muzi, D. A. Pryma, and J. M. Specht, "FLt-PET for breast cancer response assessment after neoadjuvant chemotherapy: Results from ACRIN 6688," *Journal of Nuclear Medicine*, vol. 56, pp. 1681–1689, 2015.

[104] H.-J. Eom, J. H. Cha, W. J. Choi, E. Y. Chae, H. J. Shin, and H. H. Kim, "Dynamic contrast-enhanced MRI and pathological complete response in breast cancer patients treated with neoadjuvant chemotherapy," *American Journal of Roentgenology*, vol. 208, W225–W232, 2017.

[105] B. J. Tromberg, Z. Zhang, A. Leproux, T. D. O'Sullivan, A. E. Cerussi, P. M. Carpenter, R. S. Mehta, D. Roblyer, W. Yang, and K. D. Paulsen, "Predicting responses to neoadjuvant chemotherapy in breast cancer: A diffuse optical spectroscopic imaging study," *Cancer Research*, vol. 76, pp. 5933–5944, 2016.

[106] J. Culver, R. Choe, M. Holboke, L. Zubkov, T. Durduran, A. Slemp, V. Ntziachristos, B. Chance, and A. Yodh, "Three-dimensional diffuse optical tomography in the parallel plane transmission geometry: Evaluation of a hybrid frequency time-domain instrument and image reconstruction algorithm," *Medical Physics*, vol. 30, pp. 235–247, 2003.

[107] J. Xia, J. Yao, and L. V. Wang, "Photoacoustic tomography: Principles and advances," *Progress in Electromagnetic Research*, vol. 147, pp. 1–22, 2014.

[108] E. Hysi, L. A. Wirtzfeld, J. P. May, E. Undzys, S.-D. Li, and M. C. Kolios, "Photoacoustic imaging for monitoring the response of breast cancer to neoadjuvant chemotherapy," *Photoacoustics*, vol. 5, pp. 25–36, 2017.

[109] J. P. May, E. Hysi, L. A. Wirtzfeld, E. Undzys, S.-D. Li, and M. C. Kolios, "Photoacoustic monitoring of breast cancer response to chemotherapy in a preclinical model," *PLOS ONE*, vol. 11, e0157413, 2016.

[110] X. Li, C. Heldermon, and H. Jiang, "Photoacoustic tomography of breast cancer: Monitoring neoadjuvant chemotherapy," in *Biomedical Optics*, vol. BS3A, 2014, p. 66.

[111] A. R. Reynolds, I. R. Hart, A. R. Watson, J. C. Welti, R. G. Silva, S. D. Robinson, G. Da Violante, M. Gourlaouen, M. Salih, and M. C. Jones, "Stochastic *VEGF* signalling inhibitors as anti-cancer therapies," *Nature Medicine*, vol. 15, pp. 392–400, 2009.

[112] B. P. Schneider and K. D. Miller, "Angiogenesis of breast cancer," *Journal of Clinical Oncology*, vol. 23, pp. 1782–1790, 2005.

[113] H. J. Burstein, Y.-H. Chen, L. M. Parker, J. Savoie, J. Younger, I. Kuter, P. D. Ryan, J. E. Garber, H. Chen, and S. M. Campos, "Vegf as a marker for breast cancer response to chemotherapy and bevacizumab," *Clinical Cancer Research*, vol. 14, pp. 7871–7877, 2008.

[114] I. W. Sudarsa, I. B. T. W. Manuaba, S. Maliawan, and I. W. P. Sutirtayasa, "Expression of *VEGF* and correlation with chemotherapy response in breast cancer," *Bali Medical Journal*, vol. 5, pp. 35–40, 2016.

[115] H. J. Van Staveren, C. J. Moes, J. van Marie, S. A. Prahl, and M. J. van Gemert, "Light scattering in intralipid–10% in the wavelength range of 400–1100 nm," *Applied Optics*, vol. 30, pp. 4507–4514, 1991.

[116] D. Grosenick, H. Rinneberg, R. Cubeddu, and P. Taroni, "Review of optical breast imaging and spectroscopy," *Journal of Biomedical Optics*, vol. 21, p. 091 311, 2016.

[117] S. C. Heffelfinger, M. A. Miller, R. Yassin, and R. Gear, "Angiogenic growth factors in preinvasive breast disease," *Clinical Cancer Research*, vol. 5, pp. 2867–2876, 1999.

[118] T. Fukuda, R. Horii, N. Gomi, Y. Miyagi, S. Takahashi, Y. Ito, F. Akiyama, S. Ohno, and T. Iwase, "Factors affecting the detection of occult breast cancers," *SpringerPlus*, vol. 5, p. 152, 2016.

[119] C. B. J. H. Wilson, A. A. Lammertsma, C. G. McKenzie, K. ikora, and T. Jones, "Measurements of blood volume and flow in breast tumors," *Cancer Research*, vol. 52, pp. 1592–1597, 1992.

[120] E. L. Madsen, M. E. Deaner, and J. Mehi, "Ultrasonic properties of tissue-mimicking materials," *Ultrasound in Medicine and Biology*, vol. 37, pp. 1327–1343, 2011.

[121] A. M. Winkler, K. I. Maslov, and L. V. Wang, "Noise-equivalent sensitivity of photoacoustic nanoparticle contrast agents," *Journal of Biomedical Optics*, vol. 18, p. 097 003, 2013.

[122] H. Zhao, K. Li, N. Chen, K. Zhang, L. Wang, R. Lin, X. Gong, L. Song, Z. Liu, and C. Liu, "Multiscale vessel enhancement in photoacoustic imaging," *IEEE Photonics Journal*, vol. 11, pp. 1–12, 2019.

[123] H. Zhao, Z. Ke, N. Chen, S. Wang, K. Li, L. Wang, X. Gong, W. Zheng, L. Song, Z. Liu, D. Liang, and C. Liu, "Deep learning-based reconstruction and enhancement of photoacoustic images," *Journal of Biophotonics*, vol. 13, e201960147, 2019.

[124] N. Weidner, J. Folkman, F. Pozza, P. Bevilacqua, E. N. Allred, D. H. Moore, S. Meli, and G. Gasparini, "Tumor angiogenesis: A new significant and independent prognostic indicator in early-stage breast carcinoma," *Journal of the National Cancer Institute*, vol. 84, pp. 1875–1887, 1992.

[125] A. L. Harris, H. Zhang, A. Moghaddam, S. Fox, P. Scott, A. Pattison, K. Gatter, I. Stratford, and R. Bicknell, "Breast cancer angiogenesis as a target for therapy," *Breast Cancer Research and Treatment*, vol. 38, pp. 97–103, 1996.

[126] E. J. Feuer *et al.*, "The lifetime risk of developing breast cancer," *Journal of the National Cancer Institute*, vol. 85, pp. 892–897, 1993.

[127] S. J. Hockenberger, "Fibrocystic breast disease: Every woman is at risk," *Plastic and Aesthetic Nursing*, vol. 13, pp. 37–40, 1993.

[128] R. L. Siegel, K. D. Miller, H. E. Fuchs, and A. Jemal, "Cancer statistics, 2021," *CA: A Cancer Journal for Clinicians*, vol. 71, pp. 7–33, 2021.

[129] D. A. Spak, J. S. Plaxco, L. Santiago, M. J. Dryden, and B. E. Dogan, "Bi-rads fifth edition: A summary of changes," *Diagnostic and Interventional Imaging*, vol. 98, pp. 179–190, 2017.

[130] F. Pesapane *et al.*, "Will traditional biopsy be substituted by radiomics and liquid biopsy for breast cancer diagnosis and characterisation?" *Medical Oncology*, vol. 37, p. 29, 2020.

[131] M. B. Popli, R. Teotia, M. Narang, and H. Krishna, "Breast positioning during mammography: Mistakes to be avoided," *Breast Cancer*, vol. 8, pp. 119–124, 2014.

[132] T. M. Kolb, J. Lichy, and J. H. Newhouse, "Comparison of the performance of screening mammography, physical examination, and breast us and evaluation of factors that influence them," *Radiology*, vol. 225, pp. 165–175, 2002.

[133] W. A. Berg *et al.*, "Diagnostic accuracy of mammography, clinical examination, us, and mr imaging in preoperative assessment of breast cancer," *Radiology*, vol. 233, pp. 830–849, 2004.

[134] M. von Euler-Chelpin, M. Lillholm, I. Vejborg, M. Nielsen, and E. Lynge, "Sensitivity of screening mammography by density and texture: A cohort study from a population-based screening program in denmark," *Breast Cancer Research*, vol. 21, p. 111, 2019.

[135] R. F. Brem, M. J. Lenihan, J. Lieberman, and J. Torrente, “Screening breast ultrasound: Past, present, and future,” *American Journal of Roentgenology*, vol. 204, pp. 234–240, 2015.

[136] C. D. Lehman *et al.*, “Cancer yield of mammography, mr, and us in high-risk women: Prospective multi-institution breast cancer screening study,” *Radiology*, vol. 244, pp. 381–388, 2007.

[137] V. Corsetti *et al.*, “Breast screening with ultrasound in women with mammography-negative dense breasts: Evidence on incremental cancer detection and false positives, and associated cost,” *European Journal of Cancer*, vol. 44, pp. 539–544, 2008.

[138] S. Raza, S. A. Chikarmane, S. S. Neilsen, L. M. Zorn, and R. L. Birdwell, “Bi-rads 3, 4, and 5 lesions: Value of us in management—follow-up and outcome,” *Radiology*, vol. 248, pp. 773–781, 2008.

[139] R. M. S. Sigrist, J. Liau, A. E. Kaffas, M. C. Chammas, and J. K. Willmann, “Ultrasound elastography: Review of techniques and clinical applications,” *Theranostics*, vol. 7, pp. 1303–1329, 2017.

[140] M. A. Perazella, “Gadolinium-contrast toxicity in patients with kidney disease: Nephrotoxicity and nephrogenic systemic fibrosis,” *Current Drug Safety*, vol. 3, pp. 67–75, 2008.

[141] I. Eshed, C. E. Althoff, B. Hamm, and K.-G. A. Hermann, “Claustrophobia and premature termination of magnetic resonance imaging examinations,” *Journal of Magnetic Resonance Imaging*, vol. 26, pp. 401–404, 2007.

[142] O. P. Faris and M. J. Shein, “Government viewpoint: Us food & drug administration: Pacemakers, icds and mri,” *Pacing and Clinical Electrophysiology*, vol. 28, pp. 268–269, 2005.

[143] D. R. Leff *et al.*, “Diffuse optical imaging of the healthy and diseased breast: A systematic review,” *Breast Cancer Research and Treatment*, vol. 108, pp. 9–22, 2008.

[144] L. Lin *et al.*, “Single-breath-hold photoacoustic computed tomography of the breast,” *Nature Communications*, vol. 9, p. 2352, 2018.

[145] S. Han, H. Lee, C. Kim, and J. Kim, “Review on multispectral photoacoustic analysis of cancer: Thyroid and breast,” *Metabolites*, vol. 12, p. 382, 2022.

[146] M. Dantuma *et al.*, “Fully three-dimensional sound speed-corrected multi-wavelength photoacoustic breast tomography,” *arXiv preprint*, 2023. eprint: `2308.06754`.

[147] B. P. Schneider and K. D. Miller, “Angiogenesis of breast cancer,” *Journal of Clinical Oncology*, vol. 23, pp. 1782–1790, 2005.

[148] A. R. Reynolds *et al.*, "Stimulation of tumor growth and angiogenesis by low concentrations of rgd-mimetic integrin inhibitors," *Nature Medicine*, vol. 15, pp. 392–400, 2009.

[149] P. Vaupel, A. Mayer, S. Briest, and M. Höckel, "Oxygenation status of malignant tumors: Pathogenesis of hypoxia and significance for tumor therapy," in *Oxygen Transport to Tissue XXVI*, P. Okunieff *et al.*, Eds., Springer, 2005, pp. 333–342.

[150] D. M. Gilkes and G. L. Semenza, "Role of hypoxia-inducible factors in breast cancer metastasis," *Future Oncology*, vol. 9, pp. 1623–1636, 2013.

[151] J. Folkman, "Role of angiogenesis in tumor growth and metastasis," *Seminars in Oncology*, vol. 29, pp. 15–18, 2002.

[152] L. V. Wang and S. Hu, "Photoacoustic tomography: In vivo imaging from organelles to organs," *Science*, vol. 335, pp. 1458–1462, 2012.

[153] S. A. Ermilov *et al.*, "Laser optoacoustic imaging system for detection of breast cancer," *Journal of Biomedical Optics*, vol. 14, p. 024 007, 2009.

[154] X. Li, C. D. Heldermon, L. Yao, L. Xi, and H. Jiang, "High resolution functional photoacoustic tomography of breast cancer," *Medical Physics*, vol. 42, pp. 5321–5328, 2015.

[155] M. Heijblom *et al.*, "Photoacoustic image patterns of breast carcinoma and comparisons with magnetic resonance imaging and vascular stained histopathology," *Scientific Reports*, vol. 5, p. 11 778, 2015.

[156] S. M. Schoustra *et al.*, "Imaging breast malignancies with the twente photoacoustic mammoscope 2," *PLOS ONE*, vol. 18, e0281434, 2023.

[157] G. L. G. Menezes *et al.*, "Downgrading of breast masses suspicious for cancer by using optoacoustic breast imaging," *Radiology*, vol. 288, pp. 355–365, 2018.

[158] E. I. Neuschler *et al.*, "A pivotal study of optoacoustic imaging to diagnose benign and malignant breast masses: A new evaluation tool for radiologists," *Radiology*, vol. 287, pp. 398–412, 2018.

[159] B. E. Dogan *et al.*, "Optoacoustic imaging and gray-scale us features of breast cancers: Correlation with molecular subtypes," *Radiology*, vol. 292, pp. 564–572, 2019.

[160] N. Nyayapathi *et al.*, "Photoacoustic dual-scan mammoscope: Results from 38 patients," *Biomedical Optics Express*, vol. 12, pp. 2054–2063, 2021.

[161] O. Abeyakoon *et al.*, "An optoacoustic imaging feature set to characterise blood vessels surrounding benign and malignant breast lesions," *Photoacoustics*, 2022. DOI: `10.1016/j.pacs.2022.100383`.

[162] W. Zheng *et al.*, "Deep learning enhanced volumetric photoacoustic imaging of vasculature in human," *Advanced Science*, vol. 10, p. 2 301 277, 2023.

[163] J. Rodrigues *et al.*, “Machine learning enabled photoacoustic spectroscopy for noninvasive assessment of breast tumor progression in vivo: A preclinical study,” *ACS Sensors*, vol. 9, pp. 589–601, 2024.

[164] G. Li *et al.*, “Deep learning combined with attention mechanisms to assist radiologists in enhancing breast cancer diagnosis: A study on photoacoustic imaging,” *Biomedical Optics Express*, vol. 15, pp. 4689–4704, 2024.

[165] Center for Devices and Radiological Health, “Imagio breast imaging system—p200003,” U.S. Food and Drug Administration, Tech. Rep., 2021.

[166] R. Pereira *et al.*, “Evaluation of the accuracy of mammography, ultrasound and magnetic resonance imaging in suspect breast lesions,” *Clinics*, vol. 75, e1805, 2020.

[167] J. Fitzjohn, C. Zhou, and J. G. Chase, “Critical assessment of mammography accuracy,” *IFAC-PapersOnLine*, vol. 56, pp. 5620–5625, 2023.

[168] Y.-C. Chang, Y.-H. Huang, C.-S. Huang, and R.-F. Chang, “Vascular morphology and tortuosity analysis of breast tumor inside and outside contour by 3-d power doppler ultrasound,” *Ultrasound in Medicine and Biology*, vol. 38, pp. 1859–1869, 2012.

[169] Y. Freund and R. E. Schapire, “A decision-theoretic generalization of on-line learning and an application to boosting,” *Journal of Computer and System Sciences*, vol. 55, pp. 119–139, 1997.

[170] T. Chen and C. Guestrin, “Xgboost: A scalable tree boosting system,” in *Proceedings of the 22nd ACM SIGKDD International Conference on Knowledge Discovery and Data Mining*, 2016, pp. 785–794.

[171] L. van der Maaten and G. Hinton, “Visualizing data using t-sne,” *Journal of Machine Learning Research*, vol. 9, pp. 2579–2605, 2008.

[172] J. Ma *et al.*, “Segment anything in medical images,” *Nature Communications*, vol. 15, p. 654, 2024.

[173] N. Weidner, “Intratumor microvessel density as a prognostic factor in cancer,” *American Journal of Pathology*, vol. 147, pp. 9–19, 1995.

[174] W. A. Berg *et al.*, “Combined screening with ultrasound and mammography vs mammography alone in women at elevated risk of breast cancer,” *Journal of the American Medical Association*, vol. 299, pp. 2151–2163, 2008.

[175] F. Sardanelli *et al.*, “Multicenter surveillance of women at high genetic breast cancer risk using mammography, ultrasonography, and contrast-enhanced magnetic resonance imaging (the high breast cancer risk italian 1 study): Final results,” *Investigative Radiology*, vol. 46, pp. 94–105, 2011.

[176] S. Shen *et al.*, “A multi-centre randomised trial comparing ultrasound vs mammography for screening breast cancer in high-risk chinese women,” *British Journal of Cancer*, vol. 112, pp. 998–1004, 2015.

[177] R. Guo, G. Lu, B. Qin, and B. Fei, "Ultrasound imaging technologies for breast cancer detection and management: A review," *Ultrasound in Medicine and Biology*, vol. 44, pp. 37–70, 2018.

[178] E. Devolli-Disha, S. Manxhuka-Kërliu, H. Ymeri, and A. Kutllovci, "Comparative accuracy of mammography and ultrasound in women with breast symptoms according to age and breast density," *Biomedicine*, vol. 9, pp. 131–136, 2009.

[179] A. M. Smith, M. C. Mancini, and S. Nie, "Second window for in vivo imaging," *Nature Nanotechnology*, vol. 4, pp. 710–711, 2009.

[180] J. Fenner *et al.*, "Macroscopic stiffness of breast tumors predicts metastasis," *Scientific Reports*, vol. 4, p. 5512, 2014.

[181] N. G. Ramião *et al.*, "Biomechanical properties of breast tissue, a state-of-the-art review," *Biomechanics and Modeling in Mechanobiology*, vol. 15, pp. 1307–1323, 2016.

[182] X. Qian *et al.*, "Prospective assessment of breast cancer risk from multimodal multiview ultrasound images via clinically applicable deep learning," *Nature Biomedical Engineering*, vol. 5, pp. 522–532, 2021.

[183] J. Witowski *et al.*, "Improving breast cancer diagnostics with deep learning for mri," *Science Translational Medicine*, vol. 14, eabo4802, 2022.

[184] R. Horodecki, P. Horodecki, M. Horodecki, and K. Horodecki, "Quantum entanglement," *Reviews of Modern Physics*, vol. 81, pp. 865–942, 2009.

[185] M. D. Reid, P. D. Drummond, W. P. Bowen, E. G. Cavalcanti, P. K. Lam, H. A. Bachor, U. L. Andersen, and G. Leuchs, "The Einstein–Podolsky–Rosen paradox: From concepts to applications," *Reviews of Modern Physics*, vol. 81, pp. 1727–1751, 2009.

[186] N. Brunner, D. Cavalcanti, S. Pironio, V. Scarani, and S. Wehner, "Bell nonlocality," *Reviews of Modern Physics*, vol. 86, pp. 419–478, 2014.

[187] H. M. Wiseman, S. J. Jones, and A. C. Doherty, "Steering, entanglement, nonlocality, and the Einstein–Podolsky–Rosen paradox," *Physical Review Letters*, vol. 98, p. 140 402, 2007.

[188] X. Tong, Y. Zhang, and L. V. Wang, "Enhancing optical microscopy with quantum entanglement," *Optics & Photonics News*, vol. 35, no. 11, pp. 34–39, 2024.

[189] P. G. Kwiat, K. Mattle, H. Weinfurter, A. Zeilinger, A. V. Sergienko, and Y. Shih, "New high-intensity source of polarization-entangled photon pairs," *Physical Review Letters*, vol. 75, pp. 4337–4341, 1995.

[190] X. Tong, Z. He, Y. Zhang, S. Solomon, L. Lin, Q. Song, and L. V. Wang, "Experimental full-domain mapping of quantum correlation in Clauser-Horne-Shimony-Holt scenarios," *Physical Review Applied*, vol. 19, no. 3, p. 034 049, 2023.

[191] G. B. Lemos, V. Borish, G. D. Cole, S. Ramelow, R. Lapkiewicz, and A. Zeilinger, "Quantum imaging with undetected photons," *Nature*, vol. 512, pp. 409–412, 2014.

[192] M. J. Padgett and R. W. Boyd, "An introduction to ghost imaging: Quantum and classical," *Philosophical Transactions of the Royal Society A*, vol. 375, no. 2099, p. 20 160 233, 2017.

[193] H. Defienne, M. Reichert, I. A. B. Reid, R. W. Boyd, and D. Faccio, "Polarization entanglement–enabled quantum holography," *Nature Physics*, vol. 17, pp. 591–597, 2021.

[194] Y. Zhang†, Z. He†, X. **Tong**†, D. C. Garrett, R. Cao, and L. V. Wang, "Quantum imaging of biological organisms through spatial and polarization entanglement," *Science Advances*, 2024. DOI: `10.1126/sciadv.adk1495`,

[195] Z. He, Y. Zhang, X. Tong, L. Li, and L. V. Wang, "Quantum microscopy of cells at the Heisenberg limit," *Nature Communications*, vol. 14, p. 2441, 2023.

[196] J. S. Bell, "On the Einstein Podolsky Rosen paradox," *Physics*, vol. 1, pp. 195–200, 1964.

[197] R. Uola, A. C. S. Costa, H. C. Nguyen, and O. Gühne, "Quantum steering," *Reviews of Modern Physics*, vol. 92, p. 015 001, 2020.

[198] E. G. Cavalcanti, C. J. Foster, M. Fuwa, and H. M. Wiseman, "Analog of the Clauser–Horne–Shimony–Holt inequality for steering," *Journal of the Optical Society of America B*, vol. 32, no. 4, A74–A81, 2015.

[199] R. F. Werner, "Quantum states with Einstein–Podolsky–Rosen correlations admitting a hidden-variable model," *Physical Review A*, vol. 40, pp. 4277–4281, 1989.

[200] A. K. Ekert, "Quantum cryptography based on Bell's theorem," *Physical Review Letters*, vol. 67, pp. 661–663, 1991.

[201] A. Acín, N. Brunner, N. Gisin, S. Massar, S. Pironio, and V. Scarani, "Device-independent security of quantum cryptography against collective attacks," *Physical Review Letters*, vol. 98, p. 230 501, 2007.

[202] N. Gisin, G. Ribordy, W. Tittel, and H. Zbinden, "Quantum cryptography," *Reviews of Modern Physics*, vol. 74, pp. 145–195, 2002.

[203] S. Pironio, A. Acín, N. Brunner, N. Gisin, S. Massar, and V. Scarani, "Device-independent quantum key distribution secure against collective attacks," *New Journal of Physics*, vol. 11, p. 045 021, 2009.

[204] R. Arnon-Friedman, F. Dupuis, O. Fawzi, R. Renner, and T. Vidick, "Practical device-independent quantum cryptography via entropy accumulation," *Nature Communications*, vol. 9, p. 459, 2018.

[205] P. Cameron *et al.*, "Adaptive optical imaging with entangled photons," *Science*, vol. 383, pp. 1142–1147, 2024.

[206] Y. M. Sigal, R. Zhou, and X. Zhuang, "Visualizing and discovering cellular structures with super-resolution microscopy," *Science*, vol. 361, pp. 880–887, 2018. DOI: `10.1126/science.aau1044`.

[207] R. Tenne *et al.*, "Super-resolution enhancement by quantum image scanning microscopy," *Nature Photonics*, vol. 13, pp. 116–122, 2019. DOI: `10.1038/s41566-018-0333-z`.

[208] N. Thekkek and R. Richards-Kortum, "Optical imaging for cervical cancer detection: Solutions for a continuing global problem," *Nature Reviews Cancer*, vol. 8, pp. 725–731, 2008. DOI: `10.1038/nrc2469`.

[209] T.-L. Liu *et al.*, "Observing the cell in its native state: Imaging subcellular dynamics in multicellular organisms," *Science*, vol. 360, eaaq1392, 2018. DOI: `10.1126/science.aaq1392`.

[210] T. Zhang *et al.*, "Kilohertz two-photon brain imaging in awake mice," *Nature Methods*, vol. 16, pp. 1119–1122, 2019. DOI: `10.1038/s41592-019-0596-9`.

[211] J. Wu *et al.*, "Kilohertz two-photon fluorescence microscopy imaging of neural activity in vivo," *Nature Methods*, vol. 17, pp. 287–290, 2020. DOI: `10.1038/s41592-019-0707-0`.

[212] P. A. Morris, R. S. Aspden, J. E. C. Bell, R. W. Boyd, and M. J. Padgett, "Imaging with a small number of photons," *Nature Communications*, vol. 6, p. 5913, 2015. DOI: `10.1038/ncomms6913`.

[213] I. Kviatkovsky *et al.*, "Microscopy with undetected photons in the mid-infrared," *Science Advances*, vol. 6, eabd0264, 2020. DOI: `10.1126/sciadv.abd0264`.

[214] H. Defienne, B. Ndagano, A. Lyons, and D. Faccio, "Polarization entanglement-enabled quantum holography," *Nature Physics*, vol. 17, pp. 591–597, 2021. DOI: `10.1038/s41567-021-01218-3`.

[215] C. A. Casacio *et al.*, "Quantum-enhanced nonlinear microscopy," *Nature*, vol. 594, pp. 201–206, 2021. DOI: `10.1038/s41586-021-03528-w`.

[216] P.-A. Moreau, E. Toninelli, T. Gregory, and M. J. Padgett, "Imaging with quantum states of light," *Nature Reviews Physics*, vol. 1, pp. 367–380, 2019. DOI: `10.1038/s42254-019-0056-0`.

[217] G. Brida, M. Genovese, and I. Ruo Berchera, "Experimental realization of sub-shot-noise quantum imaging," *Nature Photonics*, vol. 4, pp. 227–230, 2010. DOI: `10.1038/nphoton.2010.29`.

[218] M. A. Taylor *et al.*, "Biological measurement beyond the quantum limit," *Nature Photonics*, vol. 7, pp. 229–233, 2013. DOI: `10.1038/nphoton.2013.34`.

[219] P.-A. Moreau *et al.*, "Demonstrating an absolute quantum advantage in direct absorption measurement," *Science Advances*, vol. 3, e1601782, 2017. DOI: `10.1126/sciadv.1601782`.

[220] I. Ruo Berchera and I. P. Degiovanni, "Quantum imaging with sub-poissonian light: Challenges and perspectives in optical metrology," *Metrologia*, vol. 56, p. 024 001, 2019. DOI: `10.1088/1681-7575/ab06e2`.

[221] N. Samantaray, I. Ruo-Berchera, A. Meda, and M. Genovese, "Realisation of the first sub-shot-noise wide-field imaging system," *Light: Science & Applications*, vol. 6, e17005, 2017. DOI: `10.1038/lsa.2017.5`.

[222] Y. Zhang, O. S. Magaña-Loaiza, T. Zhong, F. N. C. Wong, and J. H. Shapiro, "Simultaneous entanglement swapping of multiple orbital-angular-momentum states of light," *Physical Review Letters*, vol. 115, p. 260 403, 2015. DOI: `10.1103/PhysRevLett.115.260403`.

[223] J. Schneeloch, C. J. Broadbent, S. P. Walborn, E. G. Cavalcanti, and J. C. Howell, "Einstein–podolsky–rosen steering inequalities from entropic uncertainty relations," *Physical Review A*, vol. 87, p. 062 103, 2013. DOI: `10.1103/PhysRevA.87.062103`.

[224] V. Giovannetti, S. Lloyd, and L. Maccone, "Quantum-enhanced measurements: Beating the standard quantum limit," *Science*, vol. 306, pp. 1330–1336, 2004. DOI: `10.1126/science.1104149`.

[225] V. Giovannetti, S. Lloyd, and L. Maccone, "Quantum metrology," *Physical Review Letters*, vol. 96, p. 010 401, 2006. DOI: `10.1103/PhysRevLett.96.010401`.

[226] R. Demkowicz-Dobrzański, M. Jarzyna, and J. Kołodyński, "Quantum limits in optical interferometry," *Progress in Optics*, vol. 60, pp. 345–435, 2015. DOI: `10.1016/bs.po.2015.08.002`.

[227] J. P. Dowling, "Quantum optical metrology—the lowdown on high-n00n states," *Contemporary Physics*, vol. 49, pp. 125–143, 2008. DOI: `10.1080/00107510802091298`.

[228] Y. Israel, S. Rosen, and Y. Silberberg, "Supersensitive polarization microscopy using noon states of light," *Physical Review Letters*, vol. 112, p. 103 604, 2014. DOI: `10.1103/PhysRevLett.112.103604`.

[229] J. Lavoie *et al.*, "Quantum super-resolution in fluorescence microscopy," *Nature Photonics*, vol. 11, pp. 593–597, 2017. DOI: `10.1038/s41566-017-0008-0`.

[230] E. Rebufello *et al.*, "Sub-shot-noise absorption microscopy based on spatial quantum correlations," *Physical Review A*, vol. 104, p. 063 514, 2021. DOI: `10.1103/PhysRevA.104.063514`.

[231] R. Oldenbourg and M. Shribak, *Handbook of Optics*. McGraw-Hill, 2010.

[232] G. Grynberg, A. Aspect, and C. Fabre, *Introduction to Quantum Optics*. Cambridge University Press, 2010.

[233] R. Daendliker, "Concept of modes in optics and photonics," in *Sixth International Conference on Education and Training in Optics and Photonics*, vol. 3831, SPIE, 2000, pp. 193–198. DOI: `10.1117/12.388721`.

[234] J. T. Barreiro, T.-C. Wei, and P. G. Kwiat, "Beating the channel capacity limit for linear photonic superdense coding," *Nature Physics*, vol. 4, pp. 282–286, 2008. DOI: `10.1038/nphys919`.

[235] C. Lane, D. Rode, and T. Rösgen, "Two-dimensional birefringence measurement technique using a polarization camera," *Applied Optics*, vol. 60, pp. 8435–8444, 2021. DOI: `10.1364/AO.434152`.

[236] S. B. Mehta, M. Shribak, and R. Oldenbourg, "Polarized light imaging of birefringence and diattenuation at high resolution and high sensitivity," *Journal of Optics*, vol. 15, p. 094 007, 2013. DOI: `10.1088/2040-8978/15/9/094007`.

[237] J. H. Shapiro and R. W. Boyd, "The physics of ghost imaging," *Quantum Information Processing*, vol. 11, pp. 949–993, 2012. DOI: `10.1007/s11128-011-0336-5`.

[238] S.-K. Liao *et al.*, "Satellite-to-ground quantum key distribution," *Nature*, vol. 549, pp. 43–47, 2017. DOI: `10.1038/nature23655`.

[239] J. Yin *et al.*, "Satellite-based entanglement distribution over 1200 kilometers," *Science*, vol. 356, pp. 1140–1144, 2017. DOI: `10.1126/science.aan3211`.

[240] J. L. O'Brien, "Optical quantum computing," *Science*, vol. 318, pp. 1567–1570, 2007.

[241] V. Giovannetti, S. Lloyd, and L. Maccone, "Advances in quantum metrology," *Nature Photonics*, vol. 5, pp. 222–229, 2011.

[242] M. A. Taylor and W. P. Bowen, "Quantum metrology and its application in biology," *Physics Reports*, vol. 615, pp. 1–59, 2016.

[243] F. Flamini, N. Spagnolo, and F. Sciarrino, "Photonic quantum information processing: A review," *Reports on Progress in Physics*, vol. 82, p. 016 001, 2018.

[244] O. S. Magaña-Loaiza and R. W. Boyd, “Quantum imaging and information,” *Reports on Progress in Physics*, vol. 82, p. 124 401, 2019.

[245] M. I. Kolobov and C. Fabre, “Quantum limits on optical resolution,” *Physical Review Letters*, vol. 85, pp. 3789–3792, 2000.

[246] P. Busch and C. Shilladay, “Complementarity and uncertainty in mach–zehnder interferometry and beyond,” *Physics Reports*, vol. 435, pp. 1–31, 2006.

[247] M. D’Angelo, M. V. Chekhova, and Y. Shih, “Two-photon diffraction and quantum lithography,” *Physical Review Letters*, vol. 87, p. 013 602, 2001.

[248] M. W. Mitchell, J. S. Lundeen, and A. M. Steinberg, “Super-resolving phase measurements with a multiphoton entangled state,” *Nature*, vol. 429, pp. 161–164, 2004.

[249] I. Afek, O. Ambar, and Y. Silberberg, “High-NOON states by mixing quantum and classical light,” *Science*, vol. 328, pp. 879–881, 2010.

[250] R. S. Bennink, S. J. Bentley, R. W. Boyd, and J. C. Howell, “Quantum and classical coincidence imaging,” *Physical Review Letters*, vol. 92, p. 033 601, 2004.

[251] B. Ndagano *et al.*, “Quantum microscopy based on hong–ou–mandel interference,” *Nature Photonics*, vol. 16, pp. 384–389, 2022.

[252] C. Couteau, “Spontaneous parametric down-conversion,” *Contemporary Physics*, vol. 59, pp. 291–304, 2018.

[253] H. Zhang *et al.*, “Preparation and storage of frequency-uncorrelated entangled photons from cavity-enhanced spontaneous parametric downconversion,” *Nature Photonics*, vol. 5, pp. 628–632, 2011.

[254] C. Wagenknecht *et al.*, “Experimental demonstration of a heralded entanglement source,” *Nature Photonics*, vol. 4, pp. 549–552, 2010.

[255] R. Camphausen *et al.*, “A quantum-enhanced wide-field phase imager,” *Science Advances*, vol. 7, eabj2155, 2021.

[256] H. Defienne *et al.*, “Pixel super-resolution with spatially entangled photons,” *Nature Communications*, vol. 13, p. 3566, 2022.

[257] B. Ndagano *et al.*, “Imaging and certifying high-dimensional entanglement with a single-photon avalanche diode camera,” *NPJ Quantum Information*, vol. 6, p. 94, 2020.

[258] H. Defienne, M. Reichert, and J. W. Fleischer, “General model of photon-pair detection with an image sensor,” *Physical Review Letters*, vol. 120, p. 203 604, 2018.

[259] A. Meda *et al.*, “Photon-number correlation for quantum enhanced imaging and sensing,” *Journal of Optics*, vol. 19, p. 094 002, 2017.

[260] T. Gregory, P.-A. Moreau, E. Toninelli, and M. J. Padgett, “Imaging through noise with quantum illumination,” *Science Advances*, vol. 6, eaay2652, 2020.

[261] O. Varnavski and T. Goodson, “Two-photon fluorescence microscopy at extremely low excitation intensity: The power of quantum correlations,” *Journal of the American Chemical Society*, vol. 142, pp. 12 966–12 975, 2020.

[262] F. Schlawin, K. E. Dorfman, and S. Mukamel, “Entangled two-photon absorption spectroscopy,” *Accounts of Chemical Research*, vol. 51, pp. 2207–2214, 2018.

[263] E. Toninelli *et al.*, “Resolution-enhanced quantum imaging by centroid estimation of biphotons,” *Optica*, vol. 6, pp. 347–353, 2019.

[264] M. Unternährer, B. Bessire, L. Gasparini, M. Perenzoni, and A. Stefanov, “Super-resolution quantum imaging at the heisenberg limit,” *Optica*, vol. 5, pp. 1150–1154, 2018.

[265] D.-Q. Xu *et al.*, “Experimental observation of sub-Rayleigh quantum imaging with a two-photon entangled source,” *Applied Physics Letters*, vol. 106, p. 171 104, 2015.

[266] B. C. Sanders, “Review of entangled coherent states,” *Journal of Physics A: Mathematical and Theoretical*, vol. 45, p. 244 002, 2012.

[267] I. F. Santos, M. A. Sagioro, C. H. Monken, and S. Pádua, “Resolution and apodization in images generated by twin photons,” *Physical Review A*, vol. 67, p. 033 812, 2003.

[268] D. Paneru, E. Cohen, R. Fickler, R. W. Boyd, and E. Karimi, “Entanglement: Quantum or classical?” *Reports on Progress in Physics*, vol. 83, p. 064 001, 2020.

[269] L. Li *et al.*, “Metalens-array–based high-dimensional and multiphoton quantum source,” *Science*, vol. 368, pp. 1487–1490, 2020.

[270] P. J. Campagnola and C.-Y. Dong, “Second harmonic generation microscopy: Principles and applications to disease diagnosis,” *Laser & Photonics Reviews*, vol. 5, pp. 13–26, 2011.

[271] M. Saxena, G. Eluru, and S. S. Gorthi, “Structured illumination microscopy,” *Advances in Optics and Photonics*, vol. 7, pp. 241–275, 2015.

[272] L. Schermelleh *et al.*, “Super-resolution microscopy demystified,” *Nature Cell Biology*, vol. 21, pp. 72–84, 2019.